PhD-FSTM-2024-043

The Faculty of Science, Technology and Medicine

DISSERTATION

Defence held on 11/07/2024 in Luxembourg

to obtain the degree of

DOCTEUR DE L'UNIVERSITÉ DU LUXEMBOURG
EN PHYSIQUE

by

Evelyn Pratami SINAGA

born on 1 October 1991 in Surabaya (Indonesia)

MICROMAGNETIC SIMULATIONS OF MAGNETIC SMALL ANGLE NEUTRON SCATTERING OF NANOSPHERES

Dissertation defense committee

Dr. Andreas Michels, Dissertation Supervisor
Professor, University of Luxembourg
Dr. Alex Redinger, Chairman
Professor, University of Luxembourg
Dr. Sebastian Mühlbauer, Vice Chairman
Heinz Maier-Leibnitz Zentrum (MLZ), Garching
Dr. Mael Guennou
Professor, University of Luxembourg
Dr. Hamid Kachkachi
Professor, University of Perpignan, France

ABSTRACT

Magnetic nanoparticles are the subject of an immense interdisciplinary research since they offer versatile applications, e.g., in the areas of materials science, nanotechnology, and biomedicine. To assess their potential for a particular technology, it is crucial to understand their internal spin microstructure, which is often found to be nonuniform. This spin disorder has various origins, such as the presence of microsructural defects (e.g., surface anisotropy, vacancies, and antiphase boundaries), or the size and shape of the particles (and the ensuing dipolar interaction). Currently, from the experimental characterization point of view, it is an immense challenge to resolve and analyze the spin structure of nanoparticles since commonly magnetic nanoparticle assemblies consist of a (size and shape) distribution of randomly-oriented particles.

In this project, we focus on the technique of magnetic small-angle neutron scattering (SANS), which is a powerful method for the investigation of mesoscale spin structures within the volume of magnetic media. With the conventional SANS technique one can study structure on a length scale of about 1–100 nm. The relevant quantity for understanding magnetic SANS is the three-dimensional magnetization vector field $\mathbf{M} = \mathbf{M}(\mathbf{r})$, which can be computed using the continuum theory of micromagnetics. The Fourier transform $\widetilde{\mathbf{M}} = \widetilde{\mathbf{M}}(\mathbf{q})$ of the real-space spin structure then determines the magnetic neutron scattering cross section. Using numerical micromagnetic computations, we study the effect of pore-type defects and the signature of the Dzyaloshinkii-Moriya interaction (DMI) in spherical nanoparticles in the randomly-averaged SANS observables, in particular in the spin-flip SANS cross section, the related chiral function, and the pair distance distribution function.

The micromagnetic simulations on ensembles of randomly-oriented spherical (Fe and FeGe) nanoparticles take into account the Zeeman energy in the external magnetic field, the dipolar (magnetostatic) interaction energy, the energy of the

magnetocrystalline anisotropy, the isotropic and symmetric exchange energy, as well as the antisymmetric Dzyaloshinkii-Moriya interaction (DMI) energy. We use the open-source software package MuMax3, which is a widely-used micromagnetic simulation tool that enables researchers to investigate the static and dynamic nanoscale behavior of magnetic materials.

In a first part, we use the numerical micromagnetic approach to model the impact of micostructural defects on the SANS observables. More specifically, the defects are magnetic holes, i.e., regions within the nanoparticles where the saturation magnetization and the exchange constant differ from those of the host material. By analyzing the magnetic SANS cross section and the pair distance distribution as a function of the concentration of these pore-type defect, the study highlights the properties of these irregularities in the magnetic microstructure. The signature of the defects and the role of the dipolar energy are discussed and the effect of a particle-size distribution is studied. The results serve as a guideline to the experimentalist. Additionally, the research includes a comparison to experimental neutron data on an isotropic Nd-Fe-B permanent magnet, where a dipolar-energy-induced vortex-like flux-closure magnetization pattern is observed, and analyzed via the magnetic correlation function approach.

In a second part, the signature of the DMI in the SANS cross section is investigated. The DMI is a phenomenon that occurs in systems with broken inversion symmetry and strong spin-orbit coupling. When combined with all the other magnetic interactions, the DMI supports and stabilizes the formation of various complex magnetization configurations at the mesoscale level, which include helices, spin spirals, skyrmions, and hopfions. An important question in this context addresses the signature of the DMI in the neutron-scattering observables, particularly in randomly-oriented nanoparticle assemblies. In such systems, the magnetic scattering signal related to the DMI is diffuse in character and differs from the single-crystal diffraction peaks observed e.g. in the B20 compounds. Simulations were carried out for a specific parameter range of par-

ticle size ($60\,\mathrm{nm} \leq D \leq 200\,\mathrm{nm}$) and applied magnetic field ($-1\,\mathrm{T} \leq \mu_0 H_0 \leq 1\,\mathrm{T}$). The findings indicate that the chiral function is only nonzero when the DMI is taken into account in the simulations. The results are discussed in relation to the symmetry properties of the magnetization Fourier components and the energies involved under space inversion.

ACKNOWLEDGEMENTS

I would like to express my deep gratitude to God, Jesus Christ, for granting me the strength and determination to complete this dissertation. His love, grace, and mercy have been a source of comfort and motivation throughout this journey. I would also like to extend my sincere appreciation to my supervisor, Andreas Michels, for providing me with the opportunity to undertake this research and for his guidance, support, and encouragement. His expertise, patience, and willingness to provide constructive feedback have been invaluable. I am thankful to Michael Adams, Mathias Bersweiler, Ivan Titov, Phillip Bender, Štefan Liščák, and Venus Rai for their generous contribution of time and expertise in assisting me with various aspects of this research. Their input has greatly enriched this work and facilitated its completion. I am grateful to Astrid and all the administrative staff for their constant support and assistance. The National Research Fund of Luxembourg (FNR) is acknowledged for providing the financial support to carry out this thesis (PRIDE MASSENA Grant). Furthermore, I would like to express my gratitude to my family, Hesky, Asael, and Benaya, my parents, and my friends, whose unwavering support and encouragement have been a source of strength throughout the challenges and successes of this journey. I am also thankful to the participants who generously dedicated their time and shared their experiences, as their willingness to participate was essential for the completion of this research.

LIST OF PUBLICATIONS

Entries marked with (⋆) are directly related to this doctoral dissertation.

2024

1. (⋆) **Neutron scattering signature of the Dzyaloshinskii-Moriya interaction in nanoparticles**
   E.P. Sinaga, M.P. Adams, E.H. Hasdeo, and A. Michels, under review (2024). doi: arXiv:2402.00558

2. **Framework for polarized magnetic neutron scattering from nanoparticle assemblies with vortex-type spin textures**
   M.P. Adams, **E.P. Sinaga**, Š. Liščák, and A. Michels, under review (2024). doi: arXiv:2404.15826

3. **Signature of surface anisotropy in the spin-flip neutron scattering cross section of spherical nanoparticles: atomistic simulations and analytical theory**
   M.P. Adams, **E.P. Sinaga**, H. Kachkachi, and A. Michels, Phys. Rev. B **109**, 024429 (2024). doi:10.1103/PhysRevB.109.024429

2023

4. (⋆) **Micromagnetic simulation of neutron scattering from spherical nanoparticles: Effect of pore-type defects**
   E.P. Sinaga, M.P. Adams, M. Bersweiler, L.G. Vivas, E.H. Hasdeo, J. Leliaert, P. Bender, D. Honecker, and A. Michels, Phys. Rev. B **107**, 014416 (2023). doi: 10.1103/PhysRevB.107.014416

5. **Fingerprint of vortexlike flux closure in an isotropic Nd-Fe-B bulk magnet**

   M. Bersweiler, Y. Oba, **E.P. Sinaga**, I. Peral, I. Titov, M.P. Adams, V. Rai, K.L. Metlov, and A. Michels, Phys. Rev. B **108**, 094434 (2023). doi: 10.1103/PhysRevB.108.094434

6. **On the angular anisotropy of the randomly averaged magnetic neutron scattering cross section of nanoparticles**

   M.P. Adams, **E.P Sinaga**, and A. Michels, IUCrJ **10**, 261–269 (2023). doi: 10.1107/S205225252300180X

2022

7. **Magnetic nanoprecipitates and interfacial spin disorder in zero-field-annealed $\mathbf{Ni_{50}Mn_{45}In_5}$ Heusler alloys as seen by magnetic small-angle neutron scattering**

   M. Bersweiler, P. Bender, I. Peral, **E.P. Sinaga**, D. Honecker, D. Alba Venero, I. Titov, and A. Michels, J. Appl. Cryst. **55**, 713–721 (2022). doi: 10.1107/S1600576722006355

2021

8. **Revealing defect-induced spin disorder in nanocrystalline Ni**

   M. Bersweiler, **E.P. Sinaga**, I. Peral, N. Adachi, P. Bender, N.-J. Steinke, E.P. Gilbert, Y. Todaka, A. Michels, and Y. Oba, Phys. Rev. Materials **5**, 044409 (2021). doi:10.1103/PhysRevMaterials.5.044409

TABLE OF CONTENTS

LIST OF FIGURES

LIST OF TABLES

Chapter 1

Introduction

Small Angle Neutron Scattering (SANS) is a powerful experimental technique used to investigate the structure and properties of materials on a mesoscopic length scale between about a few and a few hundred of nanometers [4, 7, 15]. This method uses neutrons to probe the sample and, due to the magnetic moment of the neutron, is also sensitive to the magnetic structure of materials. In SANS experiments, neutrons are scattered off the sample at small angles, usually between 0.1 and 10 degrees. By measuring the intensity of the scattered neutrons, we can gain insight into the structure and properties of the material, such as the size and shape of the scattering particles, the spacing between them, and their interactions.

This project focuses on a specific type of SANS known as "diffuse" magnetic SANS. In contrast to magnetic small angle *diffraction* that investigates long - range periodic structures, such as helical spin systems, spin-density waves, flux-line lattices in superconductors, or skyrmion crystals, "diffuse" SANS experiments focus on the scattering of neutrons at small angles near the forward direction, originating from quasi-nonperiodic long-wavelength magnetization fluctuations. The wavelength of the incident neutrons is usually much larger than the so-called Bragg cutoff of the material, so the discrete atomic structure of the sample is generally not relevant for SANS and a continuum description is appropriate. Therefore, the quantity of interest in a magnetic SANS experiment, the elastic magnetic SANS cross section, is primarily determined by the three-dimensional magnetization vector field of the sample. Figure 1.1 highlights the transition from real space to reciprocal space for the cases of a smooth texture and a discrete

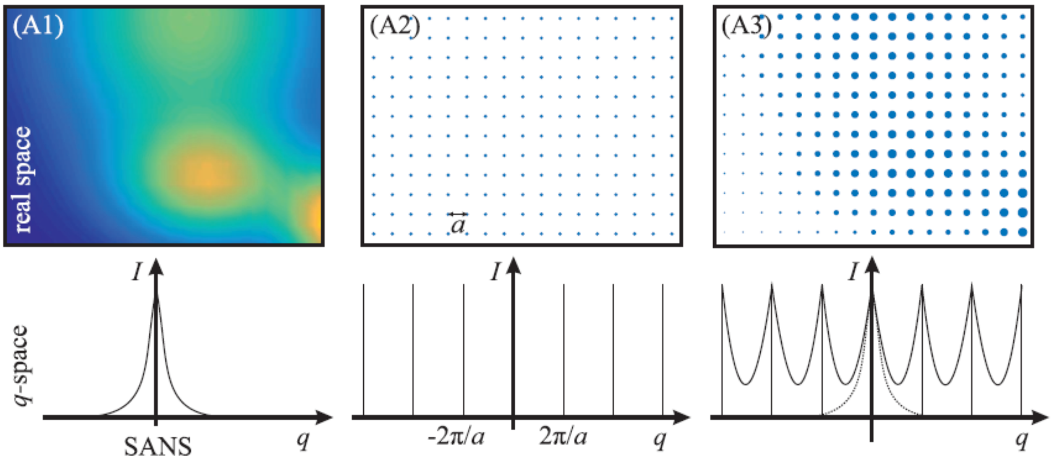

Figure 1.1: Schematic representation of the transition from real space to reciprocal space, shown for a smooth texture (A1), a discrete lattice with a lattice spacing of a (A2), and a smooth incommensurate modulation on top of a discrete lattice (A3). Image taken from [3, 4].

lattice structure.

Magnetic materials are highly valued for their diverse properties in many scientific and technological areas. Magnetic nanoparticles, in particular, possess a remarkable potential in nanotechnology due to their size-dependent magnetic properties that often differ from those of bulk materials. These magnetic nanoparticles have a wide range of applications, ranging from biomedical, environmental, and technological domains. For example, magnetic nanoparticles can be used for targeted drug delivery systems [16, 17], magnetic resonance imaging (MRI) contrast agents [18], environmental remediation [19], magnetic data storage [20], catalysis [21], and energy-related applications [22]. To gain insight into the structural and magnetic configurations of these nanoparticles, SANS is used to characterize their behavior under the application of external magnetic fields. By studying magnetic nanoparticles with the SANS technique, one can uncover their magnetic microstructure, which is essential for creating customized materials for various applications. This knowledge can then be used to improve our understanding of their behavior and promote the development of new materials for practical use.

1.1 Basic Properties of the Neutron

The neutron has a mass of 1.675×10^{-27} kg, a spin angular momentum of $\mathbf{S} = \pm 1/2\hbar$, a magnetic dipole moment of $-1.913\ \mu_{\mathrm{N}}$ (where μ_{N} is the nuclear magneton), and an average lifetime of of approximately 886 seconds [23]. These characteristics render the neutron extremely attractive for research purposes. More specifically:

- The mass of the neutron gives rise to a de Broglie wavelength for research neutrons that aligns with the interatomic distances found in numerous crystalline and liquid materials (Å regime). This characteristic facilitates the study of the structure of matter. Additionally, given that the energy levels of cold and thermal neutrons are commensurate with the elementary excitations within solids (meV regime), it becomes possible to investigate the dynamic properties through the examination of inelastic neutron scattering.

- Due to their zero net electrical charge, neutrons exhibit a very weak interaction with matter, unlike electrons, which are subject to the Coulomb barrier. Consequently, neutrons have the ability to penetrate materials deeply and interact with the atomic nuclei. The theoretical analysis of the neutron-nucleus scattering process can be conducted using first-order perturbation theory, known in the scattering formalism as the Born approximation.

- The magnetic moment of the neutron interacts with the magnetic moment of unpaired electrons in atoms, allowing for an examination of magnetic structure and dynamics through this interaction. It is important to note that magnetic neutron scattering can be as strong as the nuclear scattering.

- The average lifetime of the neutron is ± 15 minutes, i.e., it lives "long enough" so that scattering experiments can be carried out.

One might think that neutrons (being neutral particles) will only interact strongly with the materials' nuclei. However, the spin of neutrons allows the detection of the electron's magnetic moment. The diagram in Fig. 1.2 illustrates how beams of

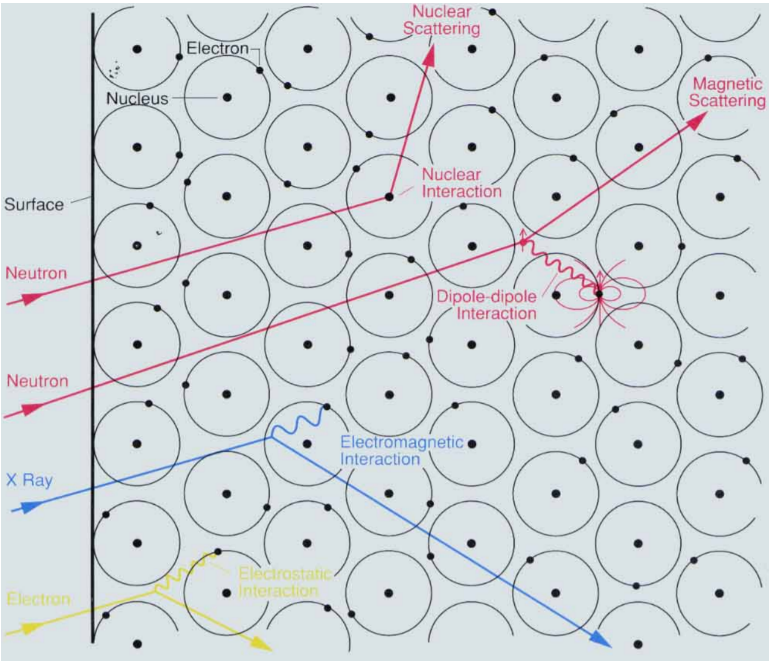

Figure 1.2: Illustration of the primary interaction mechanisms of electrons, X-rays, and neutrons with matter. Image taken from [5].

neutrons (red), X-rays (blue), and electrons (yellow) interact with matter through distinct mechanisms. Both X-rays and electrons engage with the material's electrons; the X-rays through the electromagnetic interaction, and the electrons via electrostatic forces. These interactions are strong, preventing the deep penetration of the beams into the material. Neutrons on the other hand interact with the atomic nuclei through an extremely short-ranged strong nuclear force, allowing them to penetrate materials more deeply than X-rays or electrons. If there are unpaired electrons in the sample, then the incident neutrons are scattered by them through a spin-based dipole-dipole interaction. Table 1.1 lists the basic properties of the electron, proton, and neutron:

Table 1.1: Basic properties of the three principal constituents of atoms.

Particle	Charge ($\times 10^{-19}$C)	Mass ($\times 10^{-27}$ kg)	Spin
Electron	−1.602177	0.000911	1/2
Proton	+1.602177	1.672622	1/2
Neutron	0	1.674927	1/2

1.2 Motivation for the PhD Project

This PhD project investigates the application of micromagnetic simulations to analyze the characteristics of magnetic SANS in the isolated nanosphere system. The outcomes of this research are : (i) the identification of the influence of pore-type defects within the material on the magnetic SANS observables (cross section and correlation function) [1] and (ii) the demonstration of the effect of the Dzyaloshinskii-Moriya interaction (DMI) on the magnetic SANS cross section, particularly on the chiral function, accessible using polarized neutrons [2].

(i) In recent years, magnetic nanoparticles have become increasingly important in a range of scientific and technological fields [24–26]. Magnetic SANS experiments have been used to study the spin textures of nanoparticles [3, 4, 13], with spin-polarized neutrons being a popular choice because of their sensitivity to magnetic properties.

Many of the magnetic materials which are studied by the SANS technique are polycrystalline in nature. This fact implies that the macroscopic properties and the SANS signal from these magnetic materials are largely determined by crystalline lattice imperfections, such as pores, interfaces, dislocations, or vacancies. Recent studies have shown that the spin textures of magnetic nanoparticles can be highly complex with a variety of nonuniform, canted, or core-shell-type configurations. These studies can be found in various references such as Refs. [27–39] and others. Nevertheless, the conventional approaches used to analyze magnetic SANS data make use of structural form factor models derived from nuclear SANS. Unfortunately, these models fail to accurately consider the spin inhomogeneity that is present within magnetic nanoparticles. The recent advancements in the theory of magnetic SANS demonstrate that in order to accurately analyze experimental magnetic SANS data, it is necessary to consider the spatial variation at the nanometer scale of both the orientation and magnitude of the magnetization vector field. Consequently, macrospin-based models that assume a uniform magnetization are insufficient for this task [40–49]. Furthermore, the complexity of the spin textures of magnetic nanoparticles and the limitations of the standard methods for analyzing magnetic SANS data highlight the need for further research in this field. By developing more accurate models for analyzing magnetic SANS data, researchers can gain a better understanding of the behavior of magnetic nanoparticles and their potential applications in various fields.

(ii) The Dzyaloshinkii-Moriya interaction (DMI) is a result of the relativistic spin-orbit coupling and occurs in condensed-matter systems that have a crystal field environment without inversion symmetry [50, 51]. In many studies, the DMI plays a crucial role in stabilizing different types of skyrmion textures. Its origin can be attributed to the crystal structures of the materials being investigated, with a lack of spatial inversion symmetry, or to the breaking of structural inversion symmetry at defect sites, such as interfaces in ultrathin film architectures. The presence of the DMI is responsible for many of the observed topological spin structures [52, 53]. This PhD project used numerical micromagnetic simulations to investigate the effects of the DMI on the randomly-averaged SANS observables of spherical FeGe nanoparticles. Specifically, we focus on the spin-flip SANS cross section and the related chiral function, which can be obtained from polarized SANS measurements using uniaxial polarization analysis [54].

The organization of the thesis is as follows: Section 2 establishes the theoretical foundation of neutron scattering, introducing essential scattering principles and their connection to micromagnetic simulation techniques. Section 3 delves deeper into micromagnetic theory, elucidating the various energy contributions that govern the magnetic microstructure of nanoparticles. Section 4 discusses the impact of microstructural defects on the magnetic SANS cross section and correlation function of nanoparticles, with a focus on how pore-type defects modify the scattering patterns of nanoparticles. Section 5 explores the effects of the Dzyaloshinskii-Moriya interaction (DMI) on the magnetization configurations and the ensuing spin-flip SANS cross section and chiral function of nanoparticles. Section 6 summarizes the main findings of this PhD thesis.

The results of this thesis have been published in Refs. [1, 2, 13].

Chapter 2

Theoretical Scattering Concepts

This chapter provides an overview of the basic scattering principles, the magnetic SANS method, and its relation to the micromagnetic simulation method. Readers who desire a more detailed exposition are recommended to consult recent reviews on magnetic small angle neutron scattering [55, 56] or a recently published book dedicated to the subject [4]. For further information on the general theory of neutron scattering, we refer the reader to the book by Squires [7].

2.1 Scattering Principle

The general geometry of a neutron scattering experiment is depicted in Fig. 2.1. The incoming neutron beam is characterized by the wave vector $\mathbf{k}_0$. On interacting with the sample, the neutron is scattered and acquires a new wave vector denoted by $\mathbf{k}_1$. The difference between these two wave vectors defines the momentum transfer or the scattering vector $\mathbf{q}$, which is expressed as [7]:

$$\mathbf{q} = \mathbf{k}_0 - \mathbf{k}_1. \tag{2.1}$$

The energy of a neutron can change during the scattering event, which is represented by the following expression:

$$\Delta E = E_0 - E_1 = \frac{\hbar^2}{2m_\mathrm{n}}(k_0^2 - k_1^2), \tag{2.2}$$

where E_0 (E_1) is the incident (scattered) neutron energy and m_n is the mass of the neutron. This project will focus on elastic neutron scattering, where the

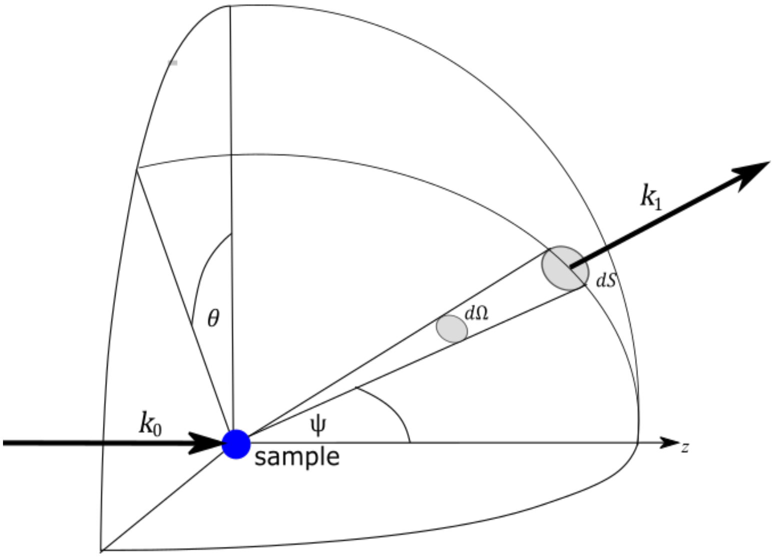

Figure 2.1: Illustration of the general neutron scattering geometry. Figure adapted from [4].

magnitudes of $\mathbf{k}_0$ and $\mathbf{k}_1$ are equal, and the energy before and after the interaction in the sample is the same (i.e., $k_0 = k_1 = 2\pi/\lambda$ and $\Delta E = 0$). Then the scattering vector $\mathbf{q}$ can be written as:

$$q = |\mathbf{q}| = 2k_0 \sin\left(\frac{\psi}{2}\right) = \frac{4\pi}{\lambda}\sin(\psi/2) \cong k_0\psi, \tag{2.3}$$

where ψ is the scattering angle and λ the average neutron wavelengths. The probability of a neutron being scattered in a particular direction $\mathbf{k}_1$ with a final energy E_1 can be expressed by the scattering function, which is the Fourier transform of the scattering potential in space and time. Experiments can be conducted to measure the number of neutrons scattered in a given direction as a function of their energy E_1. The counter (detector) and the target (sample) are assumed to be far apart, so that the (small) solid angle $d\Omega$ that the counter makes with the target is well-defined. To describe the scattering process, polar coordinates are used with the direction of the scattered neutrons being ψ and θ. The partial differential scattering cross section is then expressed as [7]:

$$\frac{d^2\sigma}{d\Omega dE_1} = \frac{n_1}{\Phi d\Omega dE_1}, \tag{2.4}$$

where n_1 is the number of neutrons scattered per second into the solid angle $d\Omega = \sin\psi d\theta d\psi$ with a final energy lying between E_1 and $E_1 + dE$. Φ is the flux of incident neutrons. In SANS experiments one measures an energy-integrated cross section, i.e., $d^2\sigma/d\Omega dE_1$ is summed over all final energies. This quantity is known as the differential scattering cross section:

$$\frac{d\sigma}{d\Omega} = \int_0^\infty \frac{n_1}{d\Omega dE_1} dE_1. \tag{2.5}$$

Then, to get the total scattering cross section σ one needs to integrate $d\sigma/d\Omega$ over all directions (assuming azimuthal symmetry):

$$\sigma = 2\pi \int_0^\pi \frac{d\sigma}{d\Omega} \sin\psi d\psi. \tag{2.6}$$

We would like to emphasize that in the field of small angle scattering, it is common practice to present the macroscopic differential SANS cross section $d\Sigma/d\Omega$ per unit volume (in cm^{-1}):

$$\frac{d\Sigma}{d\Omega} = \frac{N}{V}\frac{d\sigma}{d\Omega}, \tag{2.7}$$

where N is the number of nuclei in the sample and V is the volume of the sample.

The differential scattering cross section can be calculated by summing up all the scattering processes in which the neutron's momentum changes from its initial momentum $\mathbf{k}_0$ to its final momentum $\mathbf{k}_1$ [7]:

$$\frac{d\Sigma}{d\Omega} = \frac{1}{V}\frac{1}{\Phi}\frac{1}{d\Omega} \sum_{\mathbf{k}_1 \text{ in } d\Omega} W_{\mathbf{k}_0 \to \mathbf{k}_1}. \tag{2.8}$$

$W_{\mathbf{k}_0 \to \mathbf{k}_1}$ denotes the number of transitions per second from the state $\mathbf{k}_0$ to the $\mathbf{k}_1$; for elastic scattering only the direction of the neutron's wave vector changes. The transition rate can be determined by Fermi's golden rule [57]:

$$\sum_{\mathbf{k}_1 \text{ in } d\Omega} W_{\mathbf{k}_0 \to \mathbf{k}_1} = \frac{2\pi}{\hbar} \rho_{\mathbf{k}_1} \left|\langle \mathbf{k}_1 | V_{\text{int}} | \mathbf{k}_0 \rangle\right|^2, \tag{2.9}$$

where V_{int} is interaction potential between the neutron and the scatter, and $\rho_{\mathbf{k}_1}$ is density of final momentum states in $d\Omega$.

The calculation of the cross section can become complicated because V_{int} can be influenced by the surrounding environment. We assume that V_{int} does not trap the neutrons in a bound state. The neutrons both in an initial and final state can be thought of as free particles, while the core of the interacting potential does not move. In such cases, the Born approximation is used as a simplification technique. This involves assuming that both the incident and scattered neutrons are in a plane-wave state. The matrix element can then be reduced to a Fourier transform of the interaction potential, where the transition rate is proportional to the squared magnitude of this Fourier transform.

$$\langle \mathbf{k}_1 | V_{\text{int}} | \mathbf{k}_0 \rangle = \int d^3\mathbf{r}\; e^{-i\mathbf{k}_1\cdot\mathbf{r}} V_{\text{int}}(\mathbf{r}) e^{i\mathbf{k}_0\cdot\mathbf{r}} \tag{2.10}$$

$$= \int d^3\mathbf{r}\; e^{-i\mathbf{q}\cdot\mathbf{r}} V_{\text{int}}(\mathbf{r}) = \widetilde{V}_{\text{int}}(\mathbf{q}), \tag{2.11}$$

where $\mathbf{q} = \mathbf{k}_0 - \mathbf{k}_1$ and $\widetilde{V}_{\text{int}}(\mathbf{q})$ is the Fourier transform of $V_{\text{int}}(\mathbf{r})$.

A further discussion of the magnetic interaction potential will be presented later. Details regarding the nuclear interaction potential can be found elsewhere, such as in Refs. [7, 58].

2.2 SANS Scattering Geometry

In Fig. 2.2 a standard SANS setup is sketched. The incident neutron beam with wave vector $\mathbf{k}_0$ is directed along $\mathbf{e}_x$. The external magnetic field $\mathbf{H}_0$ is applied along $\mathbf{e}_z$ and perpendicular to $\mathbf{k}_0$. The scattering angle is denoted by ψ and $\mathbf{k}_1$ is the wave vector of the scattered neutrons. This geometry is denoted as the perpendicular scattering geometry, and used in the micromagnetic simulations. Note that the field $\mathbf{H}_0$ can also be applied parallel to $\mathbf{k}_0$ [4, 7, 59].

The scattering angle in a SANS experiment lies typically within $\psi \lesssim 0.1 - 10°$.

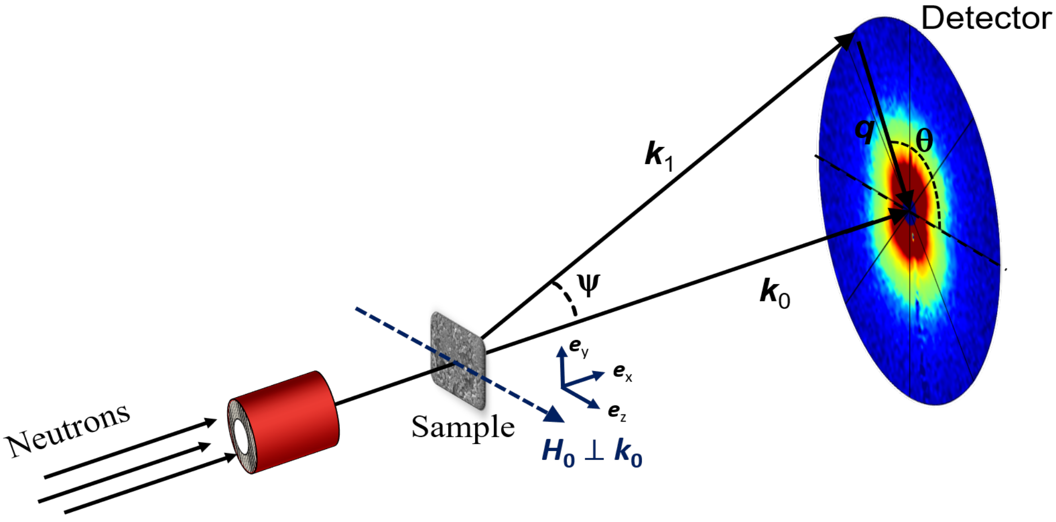

Figure 2.2: Sketch of the scattering geometry assumed in the micromagnetic SANS simulations. The applied magnetic field $\mathbf{H}_0 \parallel \mathbf{e}_z$ is perpendicular to the wave vector $\mathbf{k}_0 \parallel \mathbf{e}_x$ of the incident neutron beam ($\mathbf{k}_0 \perp \mathbf{H}_0$). Figure adapted from [4].

In this case, the components of the momentum transfer vector $\mathbf{q}$ are given by:

$$\mathbf{q} = \begin{pmatrix} q_x \\ q_y \\ q_z \end{pmatrix} = q \begin{pmatrix} -\sin\left(\frac{\psi}{2}\right) \\ \cos\left(\frac{\psi}{2}\right)\sin(\theta) \\ \cos\left(\frac{\psi}{2}\right)\cos(\theta) \end{pmatrix} = k_0 \begin{pmatrix} \cos(\psi) - 1 \\ \sin(\psi)\sin(\theta) \\ \sin(\psi)\cos(\theta) \end{pmatrix}. \tag{2.12}$$

The magnitude q of $\mathbf{q}$ is given by $2k_0 \sin(\psi/2)$. Moreover, one sees that q_x is of second order in the small angle ψ and therefore much smaller than q_y and q_z. Consequently, the three-dimensional scattering vector can be approximated by a two-dimensional one, i.e., $\mathbf{q} \cong \{0, q_y, q_z\} = q\{0, \sin\theta, \cos\theta\}$. This demonstrates that SANS predominantly probes correlations in the plane perpendicular to the incident beam. The angle $\theta = \angle(\mathbf{q}, \mathbf{H}_0)$ is used to describe the angular anisotropy of the recorded scattering pattern on the two-dimensional position sensitive detector.

2.3 Origin of Magnetic SANS

Neutrons can interact with matter in two ways: via the short-ranged nuclear interaction and via the anisotropic dipole-dipole interaction of the neutron spin with the spin of an unpaired electron. Both of these interactions, nuclear and magnetic scattering, are always present and must be taken into account when analyzing the data of an experiment. However, the micromagnetic simulations in this project focus exclusively on the magnetic scattering cross section.

The origin of magnetic SANS is due to nanometer-scale variations in both the orientation and magnitude of the magnetization vector $\mathbf{M(r)}$. A derivation of the magnetic SANS cross section will be given in Section 2.4, where we show that the magnetic interaction potential $\widetilde{V}_{\mathrm{int}}(\mathbf{q})$ [Eq. (2.11)] is proportional to $\widetilde{\mathbf{M}}(\mathbf{q})$. In Fig. 2.3 we illustrate the magnetization distribution for several cases. The simplest case is a homogeneous and uniformly magnetized ferromagnet [Fig. 2.3(a)]. Here, the magnitude $M_{\mathrm{s}} = |\mathbf{M}|$ and the direction of $\mathbf{M} \parallel \mathbf{H}_0 \parallel \mathbf{e}_z$ are the same at each point $\mathbf{r}$ within the material. The magnetization distribution is given by $\mathbf{M} = \{0,0,M_{\mathrm{s}}\}$. Consequently, there is no magnetic SANS signal for this case, and the magnetic SANS cross section reduces to a delta function at the origin of the reciprocal space,

$$\frac{d\Sigma_{\mathrm{M}}}{d\Omega} \propto |\delta(\mathbf{q})^2|. \tag{2.13}$$

In the case of a fully saturated but inhomogenous magnetic microstructure, e.g., a two-phase particle matrix system [Fig. 2.3(b)], the SANS signal has its origin in the spatial variation of the saturation magnetization. The magnetization distribution can be expressed as $\mathbf{M} = \{0, 0, M_z = M_{\mathrm{s}}(\mathbf{r})\}$ and the magnetic SANS cross section is described by the Fourier transform of the saturation magnetization profile,

$$\frac{d\Sigma_{\mathrm{M}}}{d\Omega} \propto |\widetilde{M}_{\mathrm{s}}(\mathbf{q})^2|. \tag{2.14}$$

Figure 2.3(c) depicts the most general case of an inhomogenous and nonuniformly magnetized magnetic material. In this case, the magnetization varies in

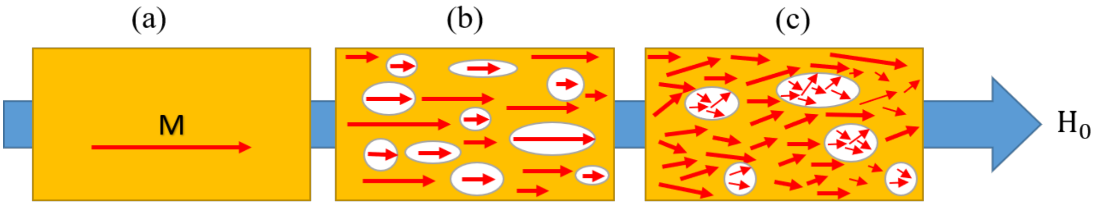

Figure 2.3: Simplified sketches of the magnetization distribution in the presence of an external magnetic field $\mathbf{H}_0$ applied in the $\mathbf{e}_z$ direction of a Cartesian coordinate system. The effects of the sample surface are not taken into account. (a) A homogeneous and saturated ferromagnet; (b) an inhomogeneous and saturated ferromagnet; (c) an inhomogeneous ferromagnet with a nonuniform magnetization distribution. Image adapted from [4].

magnitude and direction. The magnetic SANS cross section is determined by all components of the magnetization $\mathbf{M} = \{M_x(\mathbf{r}), M_y(\mathbf{r}), M_z(\mathbf{r})\}$ and will be described in more detail in the next section.

To further illustrate the most relevant case (c), we show in Fig. 2.4 the spatial distribution of the magnetization vector field $\mathbf{M}(\mathbf{r})$ around a nonmagnetic defect (magnetic hole) in a ferromagnetic Nickel (Ni) phase. The applied magnetic field $\mathbf{H}_0$ is parallel to the z direction. In Fig. 2.4(a), the applied magnetic field is close to the remanent state, with a magnitude of 0.05 T. In contrast, Fig. 2.4(b) corresponds to the saturated state, with an applied magnetic field of 2 T. The top panel represents the projection of the three-dimensional $\mathbf{M}(\mathbf{r})$ into the y-z plane, while the bottom panel represents the perpendicular magnetization component M_y (in arbitrary units). The material parameters used can be found in [60]. The presence of localized perturbations caused by defects is visible at a field of 0.05 T. The purpose of Fig. 2.4 is to illustrate how the nanoscale magnetization inhomogeneity associated with specific defects relates to a contrast for magnetic SANS, as will be further discussed in Chapter 4.

2.4 Magnetic SANS Cross Section

The central focus of the micromagnetic SANS simulations is to model the interaction potential V_{int} and perform the Fourier transformation according to Eq. (2.11). The magnetic interaction potential $V_{\text{int}}(\mathbf{r})$ is the interaction potential of the neu-

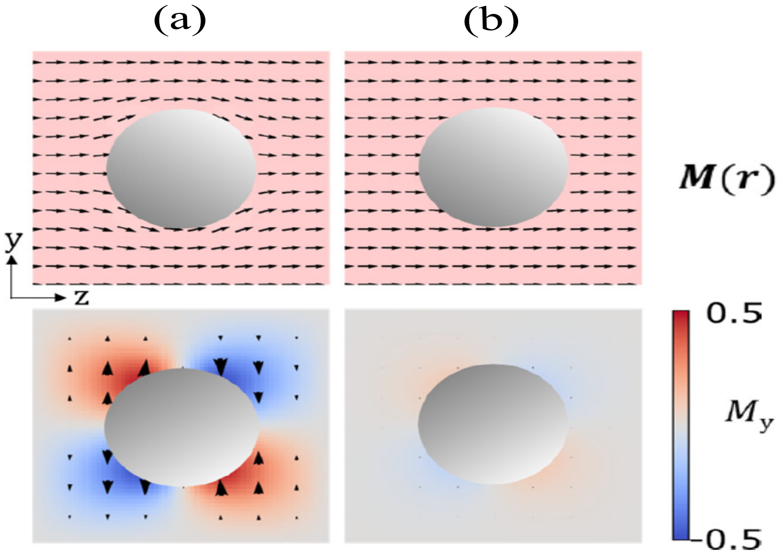

Figure 2.4: Result of a micromagnetic simulation illustrating the spin misalignment correlations around a spherical defect (nonmagnetic hole) in a uniform Ni matrix for two different applied field strengths. Panel (a) corresponds to an applied field of 0.05 T, while panel (b) corresponds to an applied field of 2 T. The top panel in each figure represents the magnetization vector in the y-z plane, while the bottom panel represents the perpendicular magnetization component M_y. Image adapted from [6].

tron's magnetic dipole moment $\boldsymbol{\mu}_\mathrm{n}$ with the magnetic induction field $\mathbf{B}(\mathbf{r})$. The expression for $V_\mathrm{int}(\mathbf{r})$ is given by [7]:

$$V_\mathrm{int}(\mathbf{r}) = -\boldsymbol{\mu}_\mathrm{n} \cdot \mathbf{B}(\mathbf{r}), \tag{2.15}$$

where $\boldsymbol{\mu}_\mathrm{n} = -\gamma_\mathrm{n}\mu_\mathrm{N}\boldsymbol{\sigma}_P$, with $\gamma_\mathrm{n} = 1.913$, μ_N is the nuclear magneton, and $\boldsymbol{\sigma}_P$ represents the Pauli spin operator for the neutron [61]. Therefore, V_int is not just a scalar quantity but rather a 2×2 matrix whose components are determined by the spin of the neutron.

Magnetic neutron scattering results from the interaction between the magnetic moment of the neutron and the magnetic field that is generated by the electron's spin ($\mathbf{B}_\mathrm{S}$) and orbital ($\mathbf{B}_\mathrm{L}$) motion. The total magnetic field $\mathbf{B}(\mathbf{r})$ at the position $\mathbf{r}$ due to the spin and the orbital motion of the electron with a magnetic moment of $\mu_\mathrm{e} = -2\mu_\mathrm{B}\mathbf{S}$ and the linear momentum $\mathbf{p}$ is given by [7]:

$$\mathbf{B}(\mathbf{r}) = \mathbf{B}_\mathrm{S} + \mathbf{B}_\mathrm{L} = \frac{\mu_0}{4\pi}\left(\nabla \times \frac{\boldsymbol{\mu}_\mathrm{e} \times \mathbf{r}}{r^3} - \frac{2\mu_\mathrm{B}}{\hbar}\frac{\mathbf{p} \times \mathbf{r}}{r^3}\right), \tag{2.16}$$

where μ_B denotes the Bohr magneton. The Fourier transform of the magnetic induction is obtained as follows [7]:

$$\widetilde{\mathbf{B}}(\mathbf{q}) = \mu_0\widetilde{\mathbf{Q}}(\mathbf{q}) = \mu_0\frac{\hat{\mathbf{q}} \times \hat{\mathbf{q}} \times \widetilde{\mathbf{M}}(\mathbf{q})}{q^2}, \tag{2.17}$$

where $\hat{\mathbf{q}}$ is the unit scattering vector and the interaction Hamiltonian reads:

$$\widetilde{V}_\mathrm{int}(\mathbf{q}) = -\mu_\mathrm{n}\mu_0\boldsymbol{\sigma} \cdot \widetilde{\mathbf{Q}}(\mathbf{q}). \tag{2.18}$$

For given initial and final spin states of the neutron, whether it is $|\uparrow\rangle = |+\rangle$ or $|\downarrow\rangle = |-\rangle$, one can compute the matrix elements as follows:

$$\begin{aligned} |\langle \pm|\widetilde{V}_\mathrm{int}(\mathbf{q})|\pm\rangle|^2 &\propto \widetilde{Q}_z^*\widetilde{Q}_z \\ |\langle \pm|\widetilde{V}_\mathrm{int}(\mathbf{q})|\mp\rangle|^2 &\propto \left(\widetilde{Q}_x^*\widetilde{Q}_x + \widetilde{Q}_y^*\widetilde{Q}_y\right) \pm i\left(\widetilde{Q}_x^*\widetilde{Q}_y - \widetilde{Q}_y^*\widetilde{Q}_x\right), \end{aligned} \tag{2.19}$$

where we have used the relations:

$$\begin{aligned} \sigma_z|\pm\rangle &= \pm|\pm\rangle, \\ \sigma_\pm|\mp\rangle &= |\pm\rangle, \\ \sigma_\pm &= \frac{1}{2}\left(\sigma_x \pm i\sigma_y\right). \end{aligned} \tag{2.20}$$

σ_z is the eigenstate of $|\pm\rangle$ and $\sigma_\pm$ is the raising or lowering operator. The matrix elements Eq. (2.19) are essential to distinguish the unpolarized SANS from the polarized SANS cross section, as discussed below.

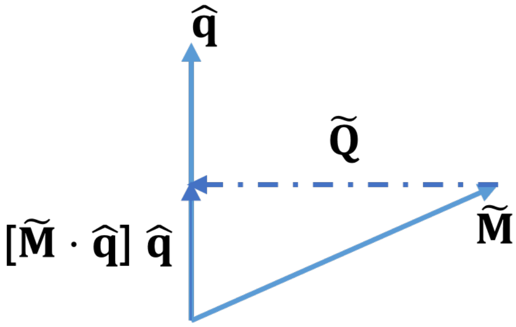

Figure 2.5: Illustration of the geometrical relationship embodied in the Halpern-Johnson vector $\widetilde{\mathbf{Q}}(\mathbf{q})$ [Eq. (2.24)]. Image adapted from [4].

2.4.1 Unpolarized SANS Cross Section

For the unpolarized SANS cross section, one can sum up all the matrix elements in Eq. (2.19) and obtain:

$$\begin{aligned}\frac{d\Sigma_{\mathrm{M}}}{d\Omega}(\mathbf{q}) &= \frac{1}{V}b_{\mathrm{H}}^2\left|\int_V \mathbf{Q}(\mathbf{r})\exp(-i\mathbf{q}\cdot\mathbf{r})d^3r\right|^2 \\ &= \frac{8\pi^3}{V}b_{\mathrm{H}}^2\left|\widetilde{\mathbf{Q}}(\mathbf{q})\right|^2 \qquad (2.21)\\ &= \frac{8\pi^3}{V}b_{\mathrm{H}}^2\left|\hat{\mathbf{q}}\times(\hat{\mathbf{q}}\times\widetilde{\mathbf{M}}(\mathbf{q}))\right|^2, \qquad (2.22)\end{aligned}$$

where V is the scattering volume, $b_{\mathrm{H}} = 2.91\times10^8\,\mathrm{A}^{-1}\mathrm{m}^{-1}$ is the magnetic scattering length in the small angle regime, and $\widetilde{\mathbf{M}}(\mathbf{q})$ is the Fourier transformation of $\mathbf{M}(\mathbf{r})$. The Fourier transform of the magnetization vector field $\mathbf{M}(\mathbf{r}) = \{M_x(\mathbf{r}), M_y(\mathbf{r}), M_z(\mathbf{r})\}$ is represented by

$$\begin{aligned}\widetilde{\mathbf{M}}(\mathbf{q}) &= \left\{\widetilde{M}_x(\mathbf{q}), \widetilde{M}_y(\mathbf{q}), \widetilde{M}_z(\mathbf{q})\right\} \\ &= \frac{1}{(2\pi)^{3/2}}\int d^3\mathbf{r}\;\mathbf{M}(\mathbf{r})\exp(-i\mathbf{q}\cdot\mathbf{r}). \qquad (2.23)\end{aligned}$$

The Halpern-Johnson vector

$$\widetilde{\mathbf{Q}} = \hat{\mathbf{q}}\times\left(\hat{\mathbf{q}}\times\widetilde{\mathbf{M}}(\mathbf{q})\right) = \hat{\mathbf{q}}\left(\hat{\mathbf{q}}\cdot\widetilde{\mathbf{M}}(\mathbf{q})\right) - \widetilde{\mathbf{M}}(\mathbf{q}) \qquad (2.24)$$

is also known as the magnetic scattering vector and plays a crucial role in understanding magnetic neutron scattering. It embodies the dipolar nature of the magnetic scattering and highlights that only the magnetization vector components that are perpendicular to $\mathbf{q}$ are significant in the scattering process, as illustrated in Fig. 2.5.

In the perpendicular scattering geometry ($\mathbf{k}_0 \perp \mathbf{H}_0$), we have $\mathbf{q} = q(0, \sin\theta, \cos\theta)$, and the Halpern-Johnson vector can be written as:

$$\widetilde{\mathbf{Q}}_\perp = \left\{ \begin{array}{c} -\widetilde{M}_x \\ -\widetilde{M}_y \cos^2\theta + \widetilde{M}_z \sin\theta\cos\theta \\ \widetilde{M}_y \sin\theta\cos\theta - \widetilde{M}_z \sin^2\theta \end{array} \right\}. \tag{2.25}$$

Readers who are interested in the case of $\mathbf{k}_0 \parallel \mathbf{H}_0$ are referred to [4].

Using the $\widetilde{\mathbf{Q}}_\perp$ defined by Eq. (2.25), the unpolarized magnetic SANS cross section (in the perpendicular scattering geometry) is given by:

$$\begin{aligned} \frac{d\Sigma_\mathrm{M}}{d\Omega} = \frac{8\pi^3}{V} b_\mathrm{H}^2 \Big(& |\widetilde{M}_x|^2 + |\widetilde{M}_y|^2 \cos^2\theta + |\widetilde{M}_z|^2 \sin^2\theta \\ & -(\widetilde{M}_y \widetilde{M}_z^* + \widetilde{M}_y^* \widetilde{M}_z) \sin\theta\cos\theta \Big), \end{aligned} \tag{2.26}$$

where the asterisk "$*$" marks the complex-conjugated quantity. For the case of a completely saturated microstructure $\mathbf{M}(\mathbf{r}) = \{0, 0, M_z(\mathbf{r})\}$, the SANS cross section reduces to:

$$\frac{d\Sigma_\mathrm{M}^\mathrm{sat}}{d\Omega} = \frac{8\pi^3}{V} b_\mathrm{H}^2 \left|\widetilde{M}_z(\mathbf{q})\right|^2 \sin^2\theta. \tag{2.27}$$

For a uniformly magnetized spherical particle (with a volume of $V_\mathrm{p} = \frac{4\pi}{3} R^3$), the only task is to find the Fourier transform $\widetilde{M}_z(\mathbf{q})$ of the z component of the magnetization. Using Eq. (2.23), we can compute this Fourier transform analytically as follows:

$$
\begin{aligned}
\widetilde{M}_z(\mathbf{q}) &= M_\mathrm{s}\int_0^{2\pi}d\phi\int_0^{\pi}d\theta\sin\theta\int_0^{\infty}r^2dr\Theta(R-r)\exp(iqr\cos\theta) \\
&= 2\pi M_\mathrm{s}\int_0^{R}r^2dr\int_{-1}^{1}d\cos\theta\exp(iqr\cos\theta) \\
&= 2\pi M_\mathrm{s}\int_0^{R}r^2dr\left[\frac{e^{iqr}-e^{-iqr}}{iqr}\right] \\
&= 4\pi M_\mathrm{s}\int_0^{R}r^2dr\frac{\sin(qr)}{qr} \\
&= 4\pi R^3M_\mathrm{s}\frac{\sin(qR)-qR\cos(qR)}{(qR)^3} = 3M_\mathrm{s}V_\mathrm{p}\frac{j_1(qR)}{qR}, \qquad (2.28)
\end{aligned}
$$

where $\Theta(x)$ is the Heaviside step function whose value is unity for $x > 0$ and zero for $x < 0$, and j_1 is the spherical Bessel function of the first kind. Using Eq. (2.28), the SANS cross section for a saturated sphere gives:

$$
\frac{d\Sigma_\mathrm{M}^\mathrm{sat}}{d\Omega} = \frac{8\pi^3}{V}b_\mathrm{H}^2M_\mathrm{s}^2 9V_\mathrm{p}^2\left(\frac{j_1(qR)}{qR}\right)^2\sin^2\theta. \qquad (2.29)
$$

Generally, one needs to carry out micromagnetic simulations to obtain $\mathbf{M}(\mathbf{r})$ and then perform the numerical Fourier transformation to get the magnetic SANS cross section [62]. The details of the micromagnetic simulations will be explained in Section 2.7 and in the Appendix C.

2.4.2 Polarized SANS Cross Section

In the case of polarized neutrons, the spin-flip SANS cross section can be determined using the matrix elements described in Eq. (2.19) as [4]:

$$
\begin{aligned}
\frac{d\Sigma_\mathrm{sf}^{+-}}{d\Omega} &= \frac{8\pi^3}{V}b_\mathrm{H}^2\Big(|\widetilde{M}_x|^2 + |\widetilde{M}_y|^2\cos^4\theta + |\widetilde{M}_z|^2\sin^2\theta\cos^2\theta \qquad (2.30) \\
&\quad -(\widetilde{M}_y\widetilde{M}_z^* + \widetilde{M}_y^*\widetilde{M}_z)\sin\theta\cos^3\theta - i\chi\Big), \\
\frac{d\Sigma_\mathrm{sf}^{-+}}{d\Omega} &= \frac{8\pi^3}{V}b_\mathrm{H}^2\Big(|\widetilde{M}_x|^2 + |\widetilde{M}_y|^2\cos^4\theta + |\widetilde{M}_z|^2\sin^2\theta\cos^2\theta \qquad (2.31) \\
&\quad -(\widetilde{M}_y\widetilde{M}_z^* + \widetilde{M}_y^*\widetilde{M}_z)\sin\theta\cos^3\theta + i\chi\Big).
\end{aligned}
$$

The superscripts “+” and “−” refer to the orientation of the neutron spin (parallel or antiparallel) in relation to the direction of the guide field $\mathbf{H}_0$. The function $\chi = \chi(\mathbf{q})$ is the so-called chiral function, which is obtained from (one-half times) the difference between the two spin-flip SANS cross sections.

$$\begin{aligned} iK\chi(\mathbf{q}) &= \frac{1}{2}\left(\frac{d\Sigma_{\mathrm{sf}}^{+-}}{d\Omega} - \frac{d\Sigma_{\mathrm{sf}}^{-+}}{d\Omega}\right) \\ &= iK\left[(\widetilde{M}_x\widetilde{M}_y^* - \widetilde{M}_x^*\widetilde{M}_y)\cos^2\theta - (\widetilde{M}_x\widetilde{M}_z^* - \widetilde{M}_x^*\widetilde{M}_z)\sin\theta\cos\theta\right], \end{aligned} \tag{2.32}$$

where $K = \frac{8\pi^3}{V} b_{\mathrm{H}}^2$. Note that the chiral function vanishes at complete magnetic saturation ($M_x^{H_0\to\infty} = M_y^{H_0\to\infty} = 0$) and for purely real-valued or purely imaginary magnetization Fourier components [2].

2.5 Pair Distance Distribution and Correlation Function

To further analyze the SANS signal, both theoretically and experimentally, one can extract the so-called pair distance distribution function $p(r)$ and the correlation function $c(r)$. These quantities are used to determine the characteristic domain sizes and provide further useful information on the spin structure that give rise to the magnetic SANS intensity.

For a single uniformly magnetized spherical particle with its saturation direction parallel to $\mathbf{e}_z$, i.e., $M_x = M_y = 0$, Eq. (2.29) can be written as:

$$\frac{d\Sigma_{\mathrm{M}}}{d\Omega} = V_{\mathrm{p}}(\Delta\rho)_{\mathrm{mag}}^2\, 9\left(\frac{j_1(qR)}{qR}\right)^2 \sin^2\theta. \tag{2.33}$$

The volume of the sphere is given by $V_{\mathrm{p}} = \frac{4\pi}{3}R^3$, where R is the radius. The term $(\Delta\rho)_{\mathrm{mag}}^2 = b_{\mathrm{H}}^2\,(\Delta M)^2$ represents the square of the difference in the saturation magnetizations between the particle and vacuum, also known as the magnetic scattering length density contrast. The well-known analytical result for the homogeneous sphere case, Eq. (2.33), follows the Guinier law $I_{\mathrm{G}} \propto \exp[-\frac{1}{5}(qR)^2]$ at small q [63] and the Porod law $I_{\mathrm{P}} \propto q^{-4}$ at large q [64] [see Fig. 2.6].

The pair distance distribution function $p(r)$ can be computed from the azimuthally-

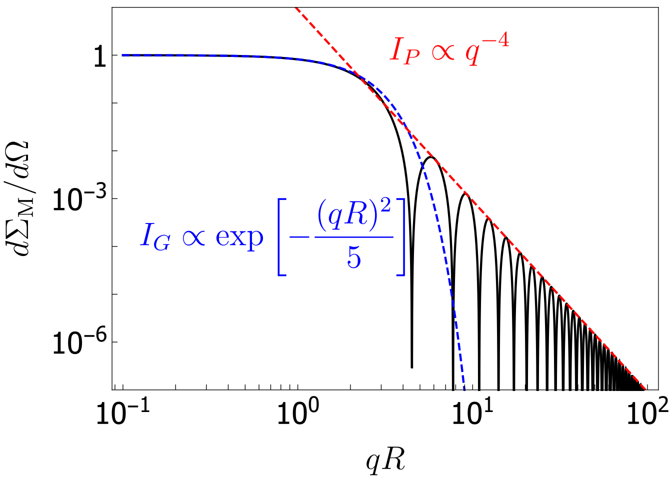

Figure 2.6: Unpolarized magnetic SANS cross section $d\Sigma_{\mathrm{M}}/d\Omega$ at saturation [Eq. (2.33)] compared with the Guinier law $I_{\mathrm{G}} \propto \exp[-\frac{1}{5}(qR)^2]$ and the Porod law $I_{\mathrm{P}} \propto q^{-4}$ at, respectively, small and large q (log-log scale).

averaged magnetic SANS cross section according to:

$$p(r) = r^2 \int_0^\infty \frac{d\Sigma_{\mathrm{M}}}{d\Omega}(q) j_0(qr) q^2 dq, \tag{2.34}$$

$$\text{where} \quad \frac{d\Sigma_{\mathrm{M}}}{d\Omega}(q) = \frac{1}{2\pi} \int_0^{2\pi} \frac{d\Sigma_{\mathrm{M}}}{d\Omega}(q,\theta) d\theta \tag{2.35}$$

and $j_0(qr) = \sin(qr)/(qr)$. The pair distance distribution function $p(r)$ corresponds to the distribution of real-space distances between volume elements inside the particle weighted by the excess scattering-length density distribution; see the reviews by Glatter [65] and by Svergun and Koch [66] for detailed discussions of the properties of $p(r)$. Apart from constant prefactors, the $p(r)$ of the azimuthally-averaged single-particle cross section [Eq. (2.33)], corresponding to a uniform sphere magnetization, equals (for $r \leq 2R$):

$$p(r) = r^2 \left(1 - \frac{3r}{4R} + \frac{r^3}{16R^3}\right), \tag{2.36}$$

while $p(r) = 0$ for $r > 2R$. We also display the correlation function $c(r)$, which is related to $p(r)$ via

$$c(r) = p(r)/r^2. \tag{2.37}$$

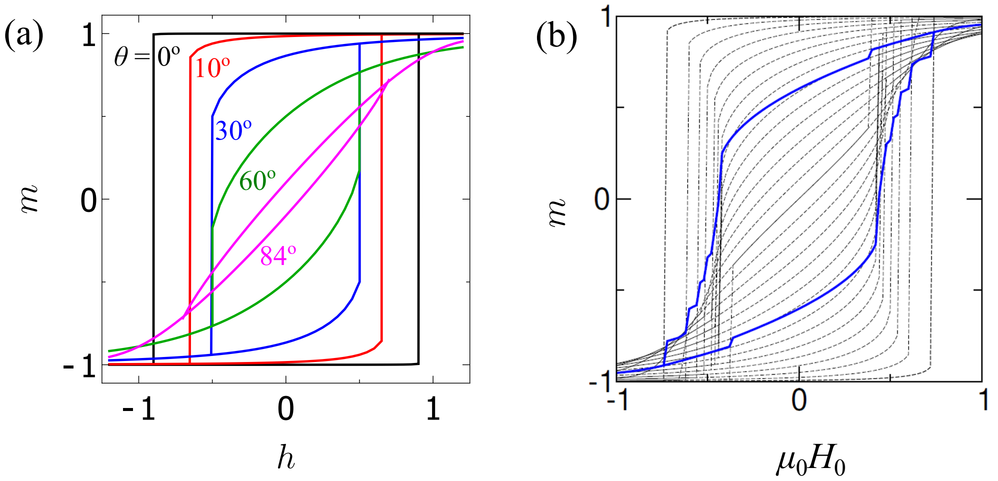

Figure 2.7: (a) Hysteresis curves according to the Stoner-Wohlfart model. Plotted is the normalized magnetization $m = \cos\phi$ as a function of the normalized applied field $h = \mu_0 H_0 M_\mathrm{s}/(2K_\mathrm{u})$ for diferent values of the angle θ between $\mathbf{H}_0$ and the uniaxial anisotropy axis. (b) Dashed lines are the hysteresis loops taken from micromagnetic simulations using the materials parameters of Cobalt with different easy axis directions. The solid blue line is the resulting averaged magnetization.

As we will demonstrate in Secs. 4 and 5, when the particles' spin structure is inhomogeneous, the $d\Sigma_\mathrm{M}/d\Omega$ and the corresponding $p(r)$ and $c(r)$ differ significantly from the homogeneous case [Eqs. (2.33) and (2.36)]. Due to the r^2 factor, features in $p(r)$ at medium and large distances are more pronounced than in $c(r)$.

2.6 The Stoner-Wohlfarth Model

For single-domain particles, the Stoner-Wohlfarth model can be used to calculate the magnetization curve [67]. In its original version, the model assumes that the magnetic anisotropy is of uniaxial symmetry, meaning that the particle possesses a single preferred direction of magnetization (due to magnetocrystalline or shape anisotropy). When an external magnetic field is applied, the magnetic moments within the particle start to rotate towards the direction of the field. At a certain critical field strength, known as the Stoner-Wohlfarth limit, the magnetic moments become completely aligned with the external field direction. This limit is determined by the balance between the magnetic anisotropy energy and the energy required to rotate the magnetic moments:

$$E = K_{\mathrm{u}} \sin^2(\phi - \theta) - \mu_0 M_{\mathrm{s}} H_0 \cos\phi, \tag{2.38}$$

where the first term is the magnetic anisotropy energy with ϕ and θ being, respectively, the angles between the magnetization and $\mathbf{H}_0$ and between $\mathbf{H}_0$ and the uniaxial easy axis. The second term is the Zeeman energy. We have written E as an energy per unit volume. To obtain the lowest energy, we normalized Eq. (2.38) and imposed that the derivative of E with respect to ϕ is zero:

$$\frac{\partial\eta}{\partial\phi} = \frac{1}{2}\sin\left(2(\phi - \theta)\right) + h\sin\phi = 0, \tag{2.39}$$

where $\eta = E/2K_{\mathrm{u}}$. There is an additional requirement for stability that we have to impose, namely $\partial^2\eta/\partial\phi^2 > 0$. We have solved these equations numerically and the results are displayed in Fig. 2.7(a).

The Stoner-Wohlfarth model is the simplest model to reproduce hysteresis effects. Well-known analytical and numerical results for the characteristic parameters coercivity and remanence exist for uniaxial and cubic particles [14]. The Stoner-Wohlfarth model is therefore very well suited to benchmark the micromagnetic SANS simulations of this project. We conducted a simulation of an isolated spherical Co nanoparticle with a diameter of 20 nm to prove the accuracy of our workflow. In this way, we replicated the Stoner-Wohlfarth results by Usov and Peschany [14]. The easy axis direction was varied in increments of 6° from 0° to 90°. As per comparison to Ref. [14] for systems with uniaxial anisotropy (see Table 2.1), it is found that the reduced remanence $m_{\mathrm{r}} = M_{\mathrm{r}}/M_{\mathrm{s}} = 0.5$, which is in excellent agreement with the outcome of our simulations. The case of a cubic particle anisotropy was also very well reproduced.

Table 2.1: Characteristic magnetic parameters of the Stoner-Wohlfarth model for particles with uniaxial and cubic anisotropy. Table taken from [14].

Property	Symbol and meaning	Uniaxial anisotropy	Cubic anisotropy	
			$K_1 < 0$	$K_1 > 0$
Reduced saturation remanence	$m_\mathrm{r}(\infty) = M_\mathrm{r}(\infty)/M_\mathrm{s}$	0.5^a	0.831^b	0.866^b
Maximal particle coercive force	$h_\mathrm{c}^\mathrm{max} = H_\mathrm{c}^\mathrm{max} M_\mathrm{s}/2\|K_1\|$	1^a	1^c	$2/3^c$
Assembly coercive force	$h_\mathrm{c} = H_\mathrm{c} M_\mathrm{s}/2\|K_1\|$	0.479	0.320 – 0.335	0.180 – 0.200
Reduced initial susceptibility	$\chi = (dm/dh)_{h->0})$	0.667	2/3	1

2.7 Details on the Micromagnetic Simulation Method

In this PhD project, the well-known open-source micromagnetic simulation software MuMax3 was used [68, 69]. MuMax3 uses a finite-difference discretization of space; it is written in Go language and uses Nvidia's GPU driver. All related information is available on http://mumax.github.io. The developers of the program are based in the DyNaMat group at Ghent University, Belgium.

The first dynamical model for the precessional motion of the magnetization was proposed by Landau and Lifshitz in 1935 [70]. MuMax3 uses the dynamic Landau-Lifshitz-Gilbert equation in the following form [68, 69]:

$$\frac{d\mathbf{m}}{dt} = \tau_{LL} = \gamma_{LL} \frac{1}{1+\alpha^2} [\mathbf{m} \times \mathbf{H}_\mathrm{eff} + \alpha(\mathbf{m} \times (\mathbf{m} \times \mathbf{H}_\mathrm{eff}))]. \tag{2.40}$$

The gyromagnetic torque τ_{LL} term in Eq. (2.40), illustrated in Fig. 2.8, encourages the magnetization to precess uniformly around the effective field $\mathbf{H}_\mathrm{eff}$. The second term in Eq. (2.40) is a damping torque which facilitates the loss of energy and the attainment of equilibrium by diminishing the precession of the magnetization around the effective field, where γ_{LL} is the gyromagnetic ratio and α is the Gilbert damping constant. In equilibrium, the magnetization has released its kinetic energy by damping losses and is parallel to the effective field, which contains the contributions due to the isotropic exchange interaction, DMI, magnetic anisotropy, and external and magnetodipolar fields.

The simulation space (= particle volume) is divided into a regular orthogonal grid with $N_x \times N_y \times N_z$ points in a Cartesian coordinate system. The majority of

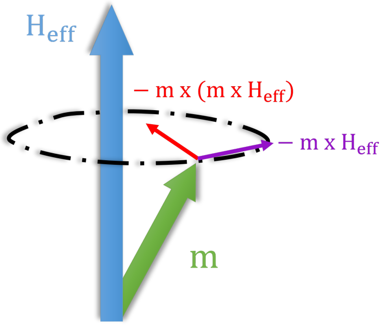

Figure 2.8: Illustration of the Landau-Lifshitz-Gilbert equation (2.40) for a single magnetic moment, with the gyromagnetic torque in purple and the damping term in red.

simulations in this thesis were carried out using a spherical particle shape, with sphere diameters ranging between about 10 – 200 nm. The sphere volume was discretized into cubical cells "i" with a size (volume) of $V_i = 2 \times 2 \times 2$ nm^3 (finite-difference method). This cell size is motivated by the values for the micromagnetic exchange lengths l_{M}, l_{K}, and l_{dmi} (see Section 3.6) and by the aim to resolve spatial variations in the magnetization that are smaller than these characteristic length scales (see the discussion in Refs. [69, 71]). In each cell "i" with volume V_i, the magnetic moment vector is given by $\boldsymbol{\mu}_i = \boldsymbol{\mu}_i(\mathbf{r}) = M_{\mathrm{s}} V_i \mathbf{m}_i(\mathbf{r})$, where $\mathbf{m}_i(\mathbf{r})$ is a unit vector along the local direction of the magnetization. Open boundary conditions were used, since we are interested in the scattering behavior of an ensemble of noninteracting single particles having random easy-axis orientations. In simulations on particles having a cubic crystal anisotropy, we have implemented the random anisotropy axes $\mathbf{c}_{1,2,3}$ as follows: $\mathbf{c}_1$ is a random unit vector that is generated using two random angles. A second random unit vector, say $\mathbf{a}$, is generated by another set of random angles, such that $\mathbf{c}_2 = (\mathbf{c}_1 \times \mathbf{a})/|\mathbf{c}_1 \times \mathbf{a}|$ and $\mathbf{c}_3 = \mathbf{c}_1 \times \mathbf{c}_2$.

All simulations were carried out by first saturating the nanoparticle with a strong external field $\mathbf{H}_0$, and then the field was decreased in steps of typically 5 mT following the major hysteresis loop. For each step of H_0 and for each particular easy-axis orientation, we have obtained the equilibrium spin structure $m_{x,y,z}(x, y, z)$ by employing both the "Relax" and "Minimize" functions of

MuMax3. The former solves the Landau-Lifshitz-Gilbert equation without the precessional term and the latter uses the conjugate-gradient method to find the configuration of minimum energy. The simulations are performed at a temperature that corresponds to zero Kelvin.

The duration of the simulations and the memory usage were extensive due to the need to consider, for a given particle diameter and for each field value along the hysteresis curve, several hundreds of random orientations of the anisotropy axes relative to the global direction of the applied magnetic field $\mathbf{H}_0$. The majority of simulations presented in this thesis were carried out using the HPC facilities of the University of Luxembourg (`https://hpc.uni.lu`).

Chapter 3

Micromagnetic Theory

Micromagnetic theory is a phenomenological continuum approach that has been created to calculate the magnetization vector field $\mathbf{M}(\mathbf{r})$ of any ferromagnetic body based on the value and direction of the applied magnetic field, the geometry of the ferromagnet, and the magnetic material parameters; see Refs. [60,67,72] for textbook expositions of this topic. This chapter will discuss the basic concepts of micromagnetism that are relevant to this PhD project. In a magnetic system, there are several different energy contributions that determine its magnetic properties. These energy contributions arise from different physical interactions between the magnetic moments, such as the isotropic exchange E_{ex}, magnetic anisotropy E_{ani}, Zeeman E_{z}, dipolar E_{d}, and Dzyalonshinskii-Moriya E_{dmi} interactions. The overall magnetic energy of a ferromagnetic material can be represented as follows:

$$E_{\mathrm{tot}} = E_{\mathrm{ex}} + E_{\mathrm{ani}} + E_{\mathrm{z}} + E_{\mathrm{d}} + E_{\mathrm{dmi}}. \tag{3.1}$$

The equilibrium magnetization distribution $\mathbf{M}(\mathbf{r})$ is obtained from variational calculus, which yields the following so-called balance of torques equation (known as Brown's equations) that represents a necessary criterion for a stable magnetization distribution [60, 67, 72]:

$$\mathbf{M}(\mathbf{r}) \times \mathbf{H}_{\mathrm{eff}}(\mathbf{r}) = 0. \tag{3.2}$$

This equation implies that the torque on the magnetization $\mathbf{M}(\mathbf{r})$ due to the effective magnetic field $\mathbf{H}_{\mathrm{eff}}(\mathbf{r})$ is zero everywhere inside the material. The field

$\mathbf{H}_{\text{eff}}$ is obtained as the functional derivative of the ferromagnetic total energy-density functional ω (with $E_{\text{tot}} = \int_V \omega[\mathbf{m}(\mathbf{r}), \nabla\mathbf{m}(\mathbf{r})]\mathrm{d}V$) with respect to the magnetization:

$$\begin{aligned} \mathbf{H}_{\text{eff}}(\mathbf{r}) &= -\frac{1}{\mu_0}\frac{\delta\omega}{\delta\mathbf{M}} \\ &= \mathbf{H}_0 + \mathbf{H}_{\text{ex}}(\mathbf{r}) + \mathbf{H}_{\text{ani}}(\mathbf{r}) + \mathbf{H}_{\text{d}}(\mathbf{r}) + \mathbf{H}_{\text{dmi}}(\mathbf{r}), \end{aligned} \tag{3.3}$$

where $\mathbf{H}_{\text{eff}}$ is (here) composed of a uniform applied magnetic field $\mathbf{H}_0$, the magnetostatic field $\mathbf{H}_{\text{d}}$, the magnetic anisotropy field $\mathbf{H}_{\text{ani}}$, the exchange field $\mathbf{H}_{\text{ex}}$, and the Dzyaloshinskii Moriya field $\mathbf{H}_{\text{dmi}}$; $\mu_0 = 4\pi \times 10^{-7}$ Tm/A denotes the permeability of free space.

The continuum theory of micromagnetism is based on the transition from a discrete atomic to a coarse-grained picture. According to this theory, the magnetization vector field in a material can be considered as a continuous function of position $\mathbf{r}$ inside the material. This function is obtained by taking the local thermodynamic average over N discrete atomic magnetic moments $\boldsymbol{\mu}_a$ within a volume V.

$$\mathbf{M} = \mathbf{M}(\mathbf{r}) = \begin{Bmatrix} M_x(x,y,z) \\ M_y(x,y,z) \\ M_z(x,y,z) \end{Bmatrix} = V^{-1}\sum_{i=1}^{N} \boldsymbol{\mu}_{a,i} \tag{3.4}$$

In the following, we will briefly discuss the main energy contributions.

3.1 Exchange Energy

The exchange interaction is caused by the Coulomb repulsion between electrons with the same spin. From the Heisenberg Hamiltonian

$$E_{\text{ex}} = -J\sum_{<i,j>} \mathbf{S}_i \cdot \mathbf{S}_j \tag{3.5}$$

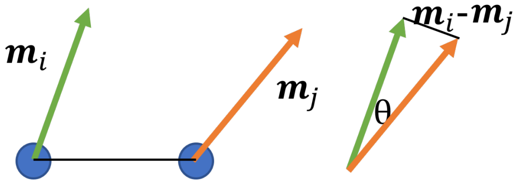

Figure 3.1: Illustration of two misaligned spins $\mathbf{m}_i$ and $\mathbf{m}_j$. θ denotes the angle between the spins. Figure adapted from [7].

the exchange energy E_{ex} is determined by the exchange constant J and the alignment of the magnetic spins $\mathbf{S}_i$ and $\mathbf{S}_j$ at neighboring lattice sites i and j. The dot product $\mathbf{S}_i \cdot \mathbf{S}_j$ is used to measure alignment. For ferromagnets with $J > 0$, the parallel alignment of magnetic moments is preferred, while the antiparallel configuration is preferred when J is negative.

Let us consider a classical scenario in which $\mathbf{S}_i$ can be depicted as a spin vector located on the lattice site i, rather than being a quantum mechanical operator. The Hamiltonian Eq. (3.5) can then be written as:

$$E_{\text{ex}} = -JS^2 \sum_{\langle i,j \rangle} \cos\theta_{ij}. \tag{3.6}$$

By assuming that the adjacent spins evolve smoothly in space (which is not significant for an antiferromagnetic arrangement), we can approximate $\cos\theta_{ij} \approx (1 - \frac{1}{2}\theta_{ij}^2)$. The first term will give rise to a constant energy value that will be neglected in the following. The second term relates the exchange energy to the square of the neighboring spin angle, which in the small angle approximation can be written as:

$$\theta_{ij} \approx (\mathbf{m}_i - \mathbf{m}_j), \tag{3.7}$$

where $\mathbf{m}$ is a unit vector (see Fig. 3.1). Further, one can approximate

$$(\mathbf{m}_i - \mathbf{m}_j) \approx (\Delta\mathbf{r}_{ji} \cdot \nabla)\, \mathbf{m}, \tag{3.8}$$

where $\Delta\mathbf{r}_{ij} = \mathbf{r}_i - \mathbf{r}_j$ is the position of the neighboring sites. Assuming an equidistant spacing of spins and a cubic lattice symmetry, the exchange energy in the continuum approximation can be written as [67]:

$$E_{\text{ex}} = A \int_V \left[(\nabla m_x)^2 + (\nabla m_y)^2 + (\nabla m_z)^2 \right] dV \tag{3.9}$$

where the integration is over the volume V of the ferromagnet, and $A > 0$ is the exchange stiffness constant. The gradient operator $\nabla = (\partial_x, \partial_y, \partial_z)$ is composed of the Cartesian unit vector axes $\mathbf{e}_x, \mathbf{e}_y, \mathbf{e}_z$, and the $m_{x,y,z}(x, y, z)$ are the components of the unit vector $\mathbf{m} = \mathbf{M}/M_{\text{s}}$ in the direction of the magnetization. Equation (3.9) implies that any nonuniformity (gradient) in the magnetization distribution is associated with an energy cost. It is also noteworthy that the exchange interaction is isotropic in space, meaning that the exchange energy of a given volume ΔV is the same for any orientation of the magnetic vector, provided that its strength remains the same. The exchange field is obtained as:

$$\mathbf{H}_{\text{ex}}(\mathbf{r}) = l_{\text{M}}^2 \nabla^2 \mathbf{M}, \tag{3.10}$$

where the exchange length $l_{\text{M}} = \sqrt{2A/(\mu_0 M_{\text{s}}^2)}$ ranges between ~3 – 10 nm [60] and will be further discussed in Section 3.6.

3.2 Dzyaloshinskii-Moriya Energy

In recent years, the Dzyaloshinskii-Moriya interaction has become the focus of a widespread research effort in condensed matter physics. Dzyaloshinskii first proposed that, based on symmetry considerations, the exchange interaction between spins could contain an antisymmetric contribution [50]. Moriya then explained this antisymmetric spin coupling in his theory of anisotropic superexchange involving the spin-orbit interaction [51]. This anisotropic antisymmetric exchange, known as DMI, is essential for understanding the spin structure of many “weakly ferromagnetic” antiferromagnets, and in particular for the recently discovered skyrmions. DMI is a magnetic energy contribution that is present in magnetic materials that lack inversion symmetry and give rise to antisymmetric magnetic interactions, such as at the boundaries between magnetic and nonmagnetic materials or in chiral magnetic materials [73–86]. For cubic crystal symmetry, this energy can be represented by:

$$E_{\mathrm{dmi}} = \mathcal{D} \int_V \mathbf{m} \cdot (\nabla \times \mathbf{m})\, dV \tag{3.11}$$

where $\mathbf{m}$ is the magnetization vector and $\nabla \times \mathbf{m}$ denotes the curl of $\mathbf{m}$. The DMI constant $\mathcal{D}$ describes the strength of the DMI and is typically expressed in units of energy per unit area J/m^2. The corresponding DMI field is obtained as:

$$\mathbf{H}_{\mathrm{dmi}}(\mathbf{r}) = -l_{\mathrm{dmi}} \nabla \times \mathbf{M} \tag{3.12}$$

where $l_{\mathrm{dmi}} = 2\mathcal{D}/(\mu_0 M_s^2)$ ($\sim 1-2\,\mathrm{nm}$) denotes the exchange length of the DMI (see Section 3.6).

3.3 Magnetocrystalline Anisotropy Energy

The magnetocrystalline anisotropy arises from the interplay between the spin-orbit coupling, which links the spin to the crystal lattice, and the crystal-field interaction. As a consequence, the magnetic energy of a magnetic material is dependent on the orientation of the magnetization vector relative to the crystal lattice. Magnetocrystalline anisotropy explains how the magnetic properties of a material are impacted by the crystal structure and the direction of the magnetization vector in comparison to the crystal axes.

Figure 3.2 illustrates how the magnetocrystalline anisotropy energy manifests in the magnetization curves of iron (bcc), nickel (fcc), and cobalt (hcp). Iron and nickel have a cubic anisotropy symmetry, while cobalt has a uniaxial anisotropy with an easy axis that (at room temperature) is parallel to the c axis of the hcp lattice. When a magnetic field is applied to iron in the [100] direction, the magnetization quickly reaches saturation. However, if the field is applied along (110) or (111) directions, the magnetization only reaches saturation at relatively

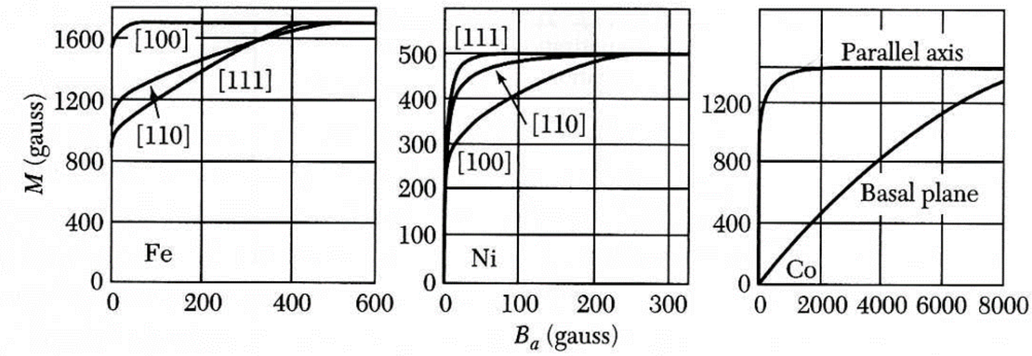

Figure 3.2: Room temperature magnetization curves of single crystals of iron, nickel, and cobalt. The results for iron reveal that the [100] direction is an easy axis of magnetization, while the [111] direction is a hard direction. The applied field is denoted as B_a and the magnetization is represented by M. Figure taken from [8].

high fields. Nickel behaves in the opposite way, while cobalt is easily magnetized along the c direction and possesses a magnetically hard basal plane.

In the book by Kronmüller and Fähnle [60], one can find expressions for the anisotropy energy of orthorhombic, tetragonal, cubic, and hexagonal crystal structures. This study will focus on uniaxial anisotropy, where the magnetic moments tend to align along one axis or within one plane, and cubic anisotropy, where the magnetic moments tend to align along one of the multiple equivalent cubic crystal axes.

One of the most common types of anisotropy is uniaxial anisotropy, which maybe characterized by a single easy direction or an easy plane (depending on the sign of the anisotropy constants, see below). For simplicity, we assume that the easy direction is given by a vector $\mathbf{u}$. The anisotropy energy can be seen as a functional of its energy density $f_{\text{an}}(\mathbf{m})$ as:

$$E_{\text{an}}(\mathbf{m}) = \int_V f_{\text{an}}(\mathbf{m}) dV. \tag{3.13}$$

The anisotropy energy is a time-reversal invariant quantity. However, the magnetization $\mathbf{m}$ breaks the time-reversal symmetry. Therefore, the phenomenological mathematical form of the uniaxial anisotropy energy density $f_{\text{u}}(\mathbf{m})$ contains (in lowest order) terms that are quadratic in $\mathbf{m}$ (plus higher orders):

$$f_\mathrm{u} = -K_1(\mathbf{m}\cdot\mathbf{u})^2 - K_2(\mathbf{m}\cdot\mathbf{u})^4 - K_3(\mathbf{m}\cdot\mathbf{u})^6 - \dots \tag{3.14}$$

K_1, K_2, K_3, … denote the temperature-dependent magnetocrystalline anisotropy constants having the dimensions of energy per unit volume $[\mathrm{J/m^3}]$. Let us assume that the easy direction coincides with the Cartesian z axis, then $(\mathbf{m}\cdot\mathbf{u})^2 = \cos^2\theta = 1-\sin^2\theta$. Using this, most of researchers prefer to write Eq. (3.14) in the following form:

$$f_\mathrm{u}(\mathbf{m}) = K_0 + K_1\sin^2\theta + K_2\sin^4\theta + K_3\sin^6\theta + \cdots, \tag{3.15}$$

where the anisotropy constants have been renormalized. We will limit our analysis to the case in which the Eq. (3.15) is cut off after the $\sin^2\theta$ term, i.e.:

$$f_\mathrm{u}(\mathbf{m}) = K_0 + K_1\sin^2\theta. \tag{3.16}$$

The anisotropic behavior is contingent on the sign of the constant K_1. When K_1 is positive, the anisotropy energy has two minima at $\theta = 0$ and $\theta = \pi$, meaning that the magnetization is directed either positively or negatively along the z axis with no preference. This is known as an easy axis anisotropy and shown in the left panel in Fig. 3.3. On the other hand, when K_1 is negative, the energy is minimized for $\theta = \pi/2$, meaning that any direction in the x-y plane is an easy direction. This is referred to as an easy plane anisotropy (see right panel in Fig. 3.3).

In a cubic crystal structure, the energy surface for magnetocrystalline anisotropy can (to lowest order) be described by a fourth-order polynomial in the spherical coordinates of the unit magnetization vector $\mathbf{m}$. The polynomial for the energy density can be expressed as:

$$f_\mathrm{c}(\mathbf{m}) = K_0 + K_1(m_x^2m_y^2 + m_x^2m_z^2 + m_y^2m_z^2) + K_2(m_x^4 + m_y^4 + m_z^4) + \cdots, \tag{3.17}$$

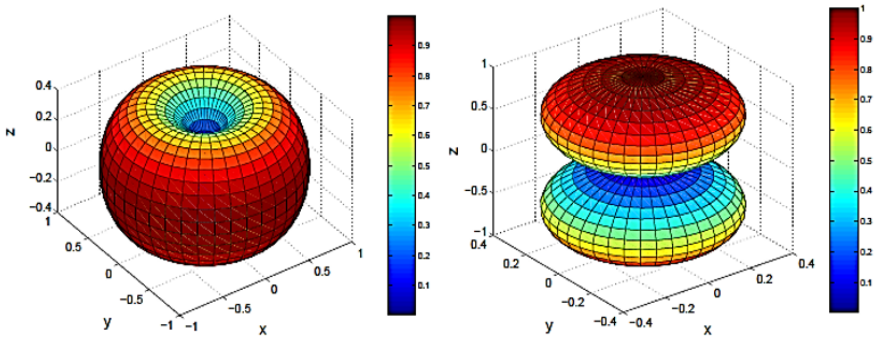

Figure 3.3: Uniaxial anisotropy energy density. The left figure is for an easy axis along the z direction ($K_1 > 0$), while the right figure is for an easy x-y plane ($K_1 < 0$). Figure taken from [9].

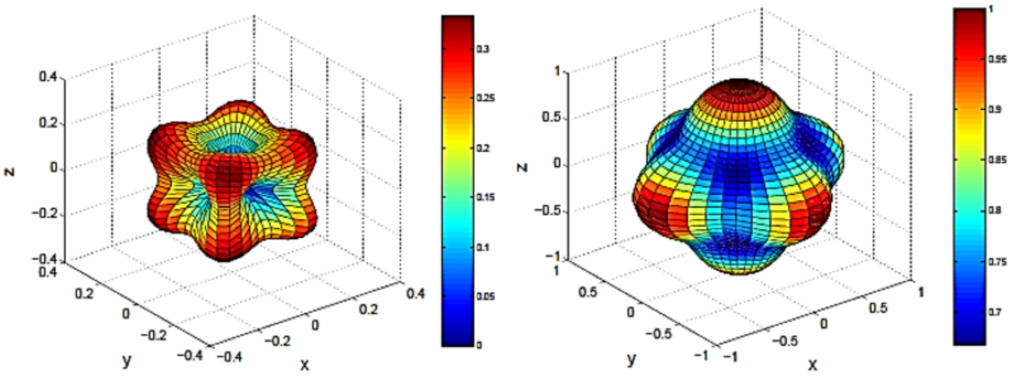

Figure 3.4: Similar to Fig. 3.3 but for a cubic anisotropy symmetry. Left panel shows the anisotropy energy for $K_1 > 0$, while the right image is for $K_1 < 0$. Figure taken from [9].

where $m_x = \mathbf{m} \cdot \mathbf{c}_1$, $m_y = \mathbf{m} \cdot \mathbf{c}_2$, and $m_z = \mathbf{m} \cdot \mathbf{c}_3$ represent the components of the magnetization vector along the three crystal axes $\mathbf{c}_1, \mathbf{c}_2, \mathbf{c}_3$ with $\mathbf{c}_3 = \mathbf{c}_1 \times \mathbf{c}_2$, and K_1 and K_2 are the cubic anisotropy constants. Higher-order terms will be neglected in the following ($K_2 = 0$). When K_1 is positive, there are six equivalent energy minima in the directions of x, y, and z, both positive and negative shown in the left panel in Fig. 3.4. However, when K_1 is negative, a more complex situation arises. In this case, there are eight equivalent minima along the directions of the vertices of the cube (e.g., the direction [1,1,1]), and the coordinate axes directions become hard axes (see the right panel in Fig. 3.4).

3.4 Zeeman Energy

The Zeeman energy (named after the Dutch physicist Pieter Zeeman) is the energy that results from the interaction between an external magnetic field and a magnetic moment. When a magnetic atom, molecule, or solid is exposed to an external magnetic field, the Zeeman effect is observed. This energy is not inherent to the material, but rather promotes the reorientation of the magnetization in the direction of the magnetic field. The Zeeman energy is given by the following expression:

$$E_{\mathrm{z}} = -\mu_0 M_{\mathrm{s}} \int\limits_V \mathbf{m} \cdot \mathbf{H}_0 \, dV \tag{3.18}$$

where $\mu_0 = 4\pi \times 10^{-7}$ Tm/A is the permeability of free space. In the micromagnetic simulations of the present project, $\mathbf{H}_0$ is assumed to be a constant vector in space.

3.5 Magnetodipolar Energy

The magnetodiplar energy arises from the interaction between the magnetic moments in the sample. Essentially, each magnetic moment interacts with the magnetic field that is produced by all the other moments. This is a long-range and anisotropic force that can be either attractive or repulsive, depending on the arrangement of the magnetic moments. The magnetodiplar interaction can be described by Maxwell's equations [87]. One of them states that there exist no magnetic monopoles, i.e.,

$$\nabla \cdot \mathbf{B} = 0, \tag{3.19}$$

where $\mathbf{B}$ is the magnetic induction field, which can be written as:

$$\mathbf{B} = \mu_0 (\mathbf{H}_0 + \mathbf{H}_{\mathrm{d}} + \mathbf{M}). \tag{3.20}$$

The contributions of exchange, DMI, and anisotropy fields are contained in the magnetization $\mathbf{M}$. As the external magnetic field $\mathbf{H}_0$ is here assumed to be constant in space, we can write:

$$\nabla \cdot \mathbf{H}_{\mathrm{d}} = -\nabla \cdot \mathbf{M}. \tag{3.21}$$

Equation (3.21) states that the sources of the magnetostatic field $\mathbf{H}_{\mathrm{d}}$ are nonzero divergences of the magnetization, so-called magnetic volume charge $-\nabla \cdot \mathbf{M} = \rho_v$. As we will see in the following, the role of the dipolar energy is to cancel the presence of these volume charges as well as the build up of surface charges on the boundary of the magnet.

Since we are dealing with magnetostatics in the absence of macroscopic currents, the following Maxwell relation applies [87]:

$$\nabla \times \mathbf{H}_{\mathrm{d}} = 0, \tag{3.22}$$

which allows us to relate $\mathbf{H}_{\mathrm{d}}$ to the (negative) gradient of a scalar potential (just like in electrostatics),

$$\mathbf{H}_{\mathrm{d}} = -\nabla \varphi. \tag{3.23}$$

Substituting Eq. (3.23) into Eq. (3.21) we obtain:

$$\begin{aligned} \nabla^2 \varphi_{\mathrm{in}} &= \nabla \cdot \mathbf{M}, \\ \nabla^2 \varphi_{\mathrm{out}} &= 0. \end{aligned} \tag{3.24}$$

Equation (3.24) is a Poisson equation, which has a formal solution whose uniqueness depends on the boundary condition. We note that the perpendicular component of $\mathbf{B}$ and the parallel component of $\mathbf{H}_{\mathrm{d}}$ should be continuous across the boundary between two regions in space. As a result, the potential is continuous across the boundary and its derivative is determined by the magnetization as follows:

$$\varphi_{\mathrm{in}} = \varphi_{\mathrm{out}} \quad \text{and} \quad \frac{\partial \varphi_{\mathrm{in}}}{\partial \mathbf{n}} - \frac{\partial \varphi_{\mathrm{out}}}{\partial \mathbf{n}} = \mathbf{n} \cdot \mathbf{M} \quad \text{on } S, \tag{3.25}$$

where $\mathbf{n}$ is a unit vector that is normal to the surface S and the directional derivative of φ (in the direction of $\mathbf{n}$) is denoted by $\partial\varphi/\partial\mathbf{n} = \nabla\varphi\cdot\mathbf{n}$. The formal solution of the Poisson Eq. (3.24) including the boundary condition is given by:

$$\varphi(\mathbf{r}) = \frac{1}{4\pi}\left(-\int\limits_V d^3\mathbf{r}' \, \frac{\nabla_{\mathbf{r}'}\cdot\mathbf{M}(\mathbf{r}')}{|\mathbf{r}-\mathbf{r}'|} + \int\limits_S d^2\mathbf{r}' \, \frac{\mathbf{n}\cdot\mathbf{M}(\mathbf{r}')}{|\mathbf{r}-\mathbf{r}'|}\right), \tag{3.26}$$

where $\mathbf{r}$ is the field point and $\mathbf{r}'$ denotes the source point. The resulting dipolar field then becomes ($\mathbf{H}_\mathrm{d} = -\nabla\varphi$)

$$\mathbf{H}_\mathrm{d}(\mathbf{r}) = \frac{1}{4\pi}\left(-\int\limits_V d^3\mathbf{r}' \, \frac{\nabla_{\mathbf{r}'}\cdot\mathbf{M}(\mathbf{r}')(\mathbf{r}-\mathbf{r}')}{|\mathbf{r}-\mathbf{r}'|^3} + \int\limits_S d^2\mathbf{r}' \, \frac{\mathbf{n}\cdot\mathbf{M}(\mathbf{r}')(\mathbf{r}-\mathbf{r}')}{|\mathbf{r}-\mathbf{r}'|^3}\right), \tag{3.27}$$

and the dipolar energy is given by the following expression [67]:

$$E_\mathrm{d} = -\frac{1}{2}\mu_0 \int\limits_V \mathbf{M}\cdot\mathbf{H}_\mathrm{d}\, dV = +\frac{1}{2}\mu_0 \int\limits_{\text{all space}} |\mathbf{H}_\mathrm{d}|^2 \, dV, \tag{3.28}$$

where the first integral is over the volume V of the ferromagnetic body, and the second integral is over all space. From Eq. (3.28), we note that the dipolar interaction energy is always positive and proportional to the square of the magnetization. The integral in Eq. (3.28) requires a six-fold integration, starting from Eq. (3.27) and subsequently Eq. (3.28). For a uniformly magnetized sphere, the magnetodipolar energy is given by $E_\mathrm{d} = \frac{1}{6}\mu_0 V_\mathrm{s} M_\mathrm{s}^2$, where V_s denotes the volume of the sphere [67].

3.6 Length Scales in Micromagnetism

A dimensional analysis of the quantities involved in the above considered magnetic energies leads to the following micromagnetic correlation or exchange lengths [60]:

$$\begin{aligned} l_{\mathrm{H}} &= \sqrt{\frac{2A}{\mu_0 M_{\mathrm{s}} H_{\mathrm{i}}}} && (3.29) \\ l_{\mathrm{M}} &= \sqrt{\frac{2A}{\mu_0 M_{\mathrm{s}}^2}} && (3.30) \\ l_{\mathrm{K}} &= \sqrt{\frac{A}{K_1}} && (3.31) \\ l_{\mathrm{dmi}} &= \frac{2\mathcal{D}}{\mu_0 M_{\mathrm{s}}^2} && (3.32) \\ D_{\mathrm{c}} &= 72\frac{\sqrt{AK_1}}{\mu_0 M_{\mathrm{s}}^2}, && (3.33) \end{aligned}$$

where A is the exchange-stiffness constant, $\mathcal{D}$ the DMI constant, M_{s} the saturation magnetization, K_1 an anisotropy constant, and H_{i} denotes the internal magnetic field. These length scales (used in the micromagnetic calculations) cover a range from a few nanometers up to a few hundred of nanometers, depending on the material parameters and the applied magnetic field [60]. This range of sizes overlaps with the resolution regime of the SANS technique, making it easy and straightforward to use micromagnetic theory to calculate the magnetic SANS cross section. Figure 3.5 displays these length scales for the materials parameters of Fe.

- l_{H} is the micromagnetic exchange length of the field. At a given magnetic field, this exchange length is a measure for the range of the exchange interaction between adjacent magnetic moments in a material. It may be used to characterize the spatial variation of the magnetization around microstructural defects [60].

- l_{M} is the magnetostatic exchange length, which characterizes the competition between the exchange and the magnetostatic interactions.

- l_{K} is the domain wall parameter, which characterizes the competition between the exchange interaction and the magnetic anisotropy.

- l_{dmi} is the exchange length of the DMI. The DMI energy between neighboring spins decays exponentially with distance, and l_{dmi} is a measure for the characteristic length over which this takes place.

- D_{c} is the critical single domain size, which can be seen as a measure for the smallest length scale at which the transition from a single domain state to a two domain state takes place in a spherical magnetic nanoparticle.

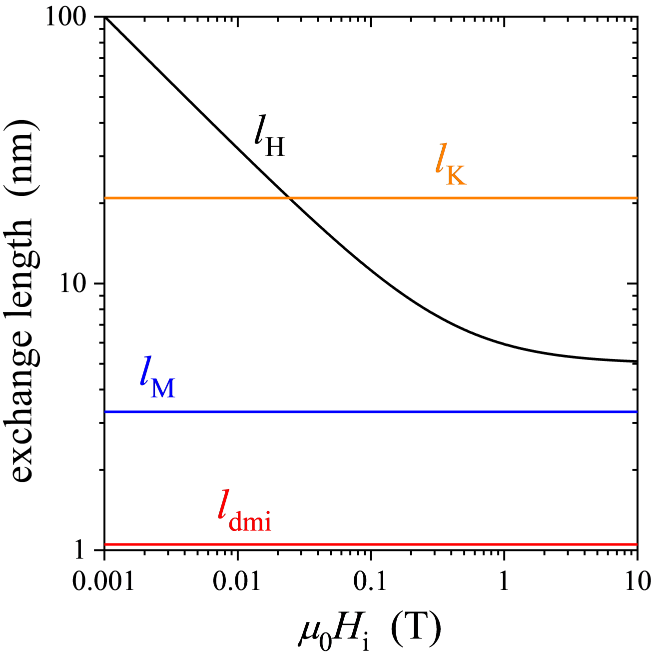

Figure 3.5: Micromagnetic exchange lengths l_{H}, l_{M}, l_{K}, and l_{dmi} (log-log scale). These length scales fall into the resolution range of the SANS technique. Materials parameters for Fe at room temperature were used. Figure taken from [4].

Chapter 4

Magnetic SANS from Spherical Nanoparticles with Pore-Type Defects

In a recent investigation, Vivas *et al.* [10] conducted numerical micromagnetic calculations to examine the magnetic small angle neutron scattering (SANS) cross section of defect-free Fe nanoparticles. Through these micromagnetic computations, the researchers explored the transition from a single-domain to a multidomain behavior in defect-free Fe nanoparticles (see Fig. 4.1), and the corresponding signatures in the SANS cross section. The magnetic SANS signal and correlation function exhibit notable distinctions compared to those of the superspin model. These findings provide valuable insights for experimentalists in identifying nonuniform dipole-field-induced vortex-type spin structures within nanoparticles [Fig. 4.1(c)].

This PhD project expands on the numerical micromagnetic approach of Ref. [10] to model the impact (on the SANS observables) of microstructural defects related to pores and a distribution function for particle sizes. [1]. The presence of defects in nanoparticles, such as vacancies, antiphase boundaries, or surface anisotropy has long been recognized to cause spin disorder, thereby influencing the overall magnetic properties (see, e.g., Refs. [38, 88–91] and references therein). Consequently, it is highly desirable to identify their characteristic features in the magnetic SANS cross section and correlation function. The results of this chapter are already published in Refs. [1, 13].

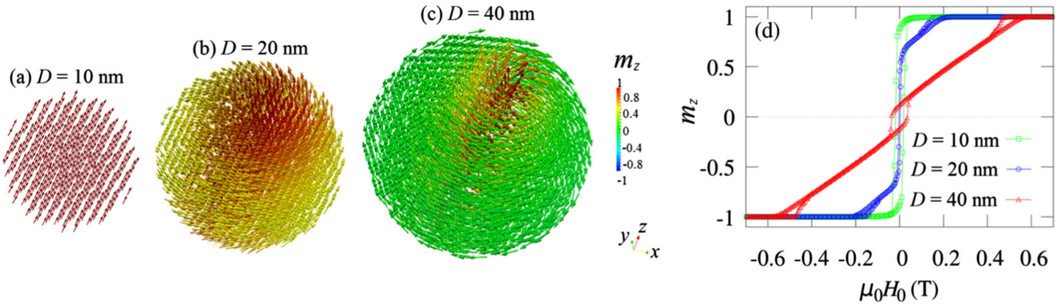

Figure 4.1: Transition from a single-domain to a multidomain behavior in defect-free Fe nanoparticles. Shown are numerically-computed spin structures of Fe nanospheres for three different diameters. (a) $D = 10\,\mathrm{nm}$, (b) $D = 20\,\mathrm{nm}$, and (c)$D = 40\,\mathrm{nm}$. (d) The corresponding normalized hysteresis loops (random particle orientations). Figure taken from [10].

4.1 Summary of Recent Results

In [10] as well as in this project [1], all four standard contributions to the overall magnetic Gibbs free energy are considered. These include the Zeeman energy E_z due to an external magnetic field $\mathbf{H}_0$, the energy due to the magnetodipolar interaction E_d, the energy arising from the (cubic) magnetocrystalline anisotropy E_ani, and the isotropic exchange energy E_ex. The continuum expressions for these energies are as follows (repeated here for the sake of a self-contained presentation):

$$\begin{aligned}
E_\mathrm{z} &= -\mu_0 M_\mathrm{s} \int \mathbf{m}\cdot\mathbf{H}_0\, dV, && (4.1)\\
E_\mathrm{d} &= -\frac{1}{2}\mu_0 M_\mathrm{s} \int \mathbf{m}\cdot\mathbf{H}_\mathrm{d}\, dV, && (4.2)\\
E_\mathrm{ani} &= K_\mathrm{c1} \int \big[(\mathbf{c}_1\cdot\mathbf{m})^2(\mathbf{c}_2\cdot\mathbf{m})^2 + (\mathbf{c}_1\cdot\mathbf{m})^2(\mathbf{c}_3\cdot\mathbf{m})^2 && (4.3)\\
&\quad +(\mathbf{c}_2\cdot\mathbf{m})^2(\mathbf{c}_3\cdot\mathbf{m})^2\big), &&\\
E_\mathrm{ex} &= A \int \left[(\nabla m_x)^2 + (\nabla m_y)^2 + (\nabla m_z)^2\right] dV, && (4.4)
\end{aligned}$$

where the integrals are taken over the volume of the sphere. $\mathbf{m}(\mathbf{r}) = \mathbf{M}(\mathbf{r})/M_\mathrm{s}$ is the unit magnetization vector, $\mathbf{H}_0$ is constant in space and parallel to the unit vector $\mathbf{e}_z$ of a global Cartesian coordinate system, the magnetodipolar self-interaction field $\mathbf{H}_\mathrm{d}(\mathbf{r})$ is given by Eq. (3.27), the first-order cubic anisotropy constant is denoted by K_c1, the vectors $\mathbf{c}_{1,2,3}$ are the local anisotropy axes of the particle, the exchange-stiffness constant is denoted by A, and $\nabla = \{\partial/\partial x, \partial/\partial y, \partial/\partial z\}$ denotes the gradient operator. In these simulations, material parameters for iron (Fe) were used: $M_{\mathrm{s}} = 1700\,\mathrm{kA/m}$, $A = 1.0 \times 10^{-11}\,\mathrm{J/m}$, and $K_{\mathrm{c1}} = 47\,\mathrm{kJ/m^3}$. The simulations are conducted at a temperature that corresponds to zero Kelvin.

The ensuing so-called Browns equations can be conveniently written in the form of a torque equation, $\mathbf{m}(\mathbf{r}) \times \mathbf{h}_{\mathrm{eff}}(\mathbf{r}) = \mathbf{0}$. For the energies Eqs. (4.1)–(4.4), the reduced effective field reads:

$$\mathbf{h}_{\mathrm{eff}} = \mathbf{h}_0 + \mathbf{h}_{\mathrm{d}} + \mathbf{h}_{\mathrm{ani}} + \mathbf{h}_{\mathrm{ex}}, \tag{4.5}$$

where $\mathbf{h}_0 = \mathbf{H}_0/M_{\mathrm{s}}$ is the normalized applied magnetic field, $\mathbf{h}_{\mathrm{d}} = \mathbf{H}_{\mathrm{d}}/M_{\mathrm{s}}$ is the magnetodipolar field,

$$\begin{aligned}
\mathbf{h}_{\mathrm{ani}} = & -\frac{2K_{\mathrm{c1}}}{\mu_0 M_{\mathrm{s}}^2}\Big\{\mathbf{c}_1(\mathbf{c}_1\cdot\mathbf{m})\left[(\mathbf{c}_2\cdot\mathbf{m})^2 + (\mathbf{c}_3\cdot\mathbf{m})^2\right] \\
& +\mathbf{c}_2(\mathbf{c}_2\cdot\mathbf{m})\left[(\mathbf{c}_1\cdot\mathbf{m})^2 + (\mathbf{c}_3\cdot\mathbf{m})^2\right] \\
& +\mathbf{c}_3(\mathbf{c}_3\cdot\mathbf{m})\left[(\mathbf{c}_1\cdot\mathbf{m})^2 + (\mathbf{c}_2\cdot\mathbf{m})^2\right]\Big\}
\end{aligned}$$

represents the cubic anisotropy field, $\mathbf{h}_{\mathrm{ex}} = l_{\mathrm{M}}^2 \nabla^2 \mathbf{m} = l_{\mathrm{M}}^2\{\nabla^2 m_x, \nabla^2 m_y, \nabla^2 m_z\}$ is the exchange field. Since the focus our research is on the randomly-averaged SANS observables, a stochastic approach was employed to distribute the orientations of the anisotropy directions relative to the global direction of $\mathbf{H}_0$. Initially, two random angles are generated to define the unit vector $\mathbf{c}_1$. Subsequently, another set of two random angles is generated to represent, for instance, the vector $\mathbf{a}$. Then $\mathbf{c}_2 = (\mathbf{c}_1 \times \mathbf{a})/|\mathbf{c}_1 \times \mathbf{a}|$, so that $\mathbf{c}_3 = \mathbf{c}_1 \times \mathbf{c}_2$. Figure 4.2 features the distribution of 100 randomly selected vectors $\mathbf{c}_1$ on the surface of the unit sphere.

Figure 4.3 illustrates how the defects (black squares) are implemented in the simulations. To begin with, the volume of the sphere is subdivided into cubical cells with dimensions of $2 \times 2 \times 2\ \mathrm{nm}^3$ using the finite difference method. The size of these cells is determined by the values of the micromagnetic exchange lengths l_{M} and l_{K} (see Fig. 3.5) and by the goal to resolve spatial changes in the

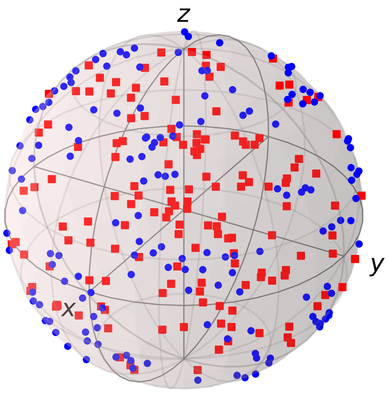

Figure 4.2: Illustration of a random distribution of $N = 100$ magnetic easy axes. The blue dots represent the spread of the cubic anisotropy axes $\mathbf{c}_1$. Each blue dot has a red dot (vector $\mathbf{c}_2$) as a corresponding partner.

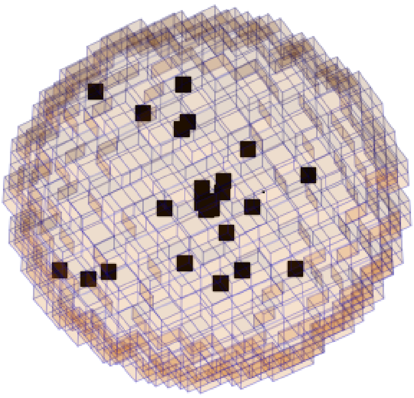

Figure 4.3: The micromagnetic simulation volume V, which has the shape of a sphere, is partitioned into cubical cells that have a typical size of $2 \times 2 \times 2\,\mathrm{nm}^3$. "Defect" cells (represented by the black squares) have been randomly selected and are characterized by a magnetization value of $M_\mathrm{s} = 0$. Figure taken from [1].

magnetization that are smaller than these characteristic length scales. The defects (with a volume fraction of x_d) are randomly assigned to this structure, and are defined as cells with a saturation magnetization of $M_\mathrm{s} = 0$. These defects might represent nonmagnetic pore-type defects. Assuming the size of a single atom to be 0.1 nm, a hole of this size consists of approximately 8000 atoms, resulting in a significant perturbation in the magnetic nanoparticle structure.

All simulations followed the same procedure. The nanoparticle is initially exposed to a strong external field $\mathbf{H}_0$, and then the field is gradually decreased in increments of typically 5 mT, following the main hysteresis loop. Micromagnetic simulations are conducted for each given volume concentration of defects ($x_\mathrm{d} \sim 0$–$20\,\%$) at each value of H_0, using approximately $N \sim 100$ random orientations of the magnetic easy axis. The defect distribution is randomly chosen for each random particle orientation. Simulations on single-domain particles with a size of 10 nm [e.g., Fig. 4.1)(a)] yield the expected values for the reduced remanence (~ 0.831) and coercivity of cubic particles, as predicted by the Stoner-Wohlfarth model [14]. From the materials parameters of Fe, the critical single-domain diameter is estimated as $D_\mathrm{c} \sim 72\sqrt{AK_\mathrm{c1}}/(\mu_0 M_\mathrm{s}^2) = 13.6$ nm [60]. Therefore, one expects inhomogeneous magnetization states for particles sizes $D \gtrsim D_\mathrm{c}$.

The translational invariance of the grid obtained by the finite-difference method allows us to use the direct Fourier transformation technique to calculate the Cartesian Fourier components $\widetilde{M}_{x,y,z}(q_x, q_y, q_z)$ of $M_{x,y,z}(x, y, z)$. To compute and analyze the Fourier components of our nanoscopic magnetic configurations, we employed the discrete Fourier transformation (see Appendix C). We have computed the magnetic SANS cross section $d\Sigma_\mathrm{M}/d\Omega$ for the random particle arrangement according to:

$$\frac{d\Sigma_\mathrm{M}}{d\Omega} = \frac{1}{N}\sum_{i=1}^{N}\frac{d\Sigma_{\mathrm{M},i}}{d\Omega}, \tag{4.6}$$

where N specifies the number of random particle orientations (typically a few hundred). The quantity $d\Sigma_{\mathrm{M},i}/d\Omega$ denotes (for a given defect concentration x_d and field value H_0) the magnetic SANS cross section of a single spherical particle of size D and with a specific random easy-axis orientation "i". Equation 4.6 implies the absence of any interference effects between the particles.

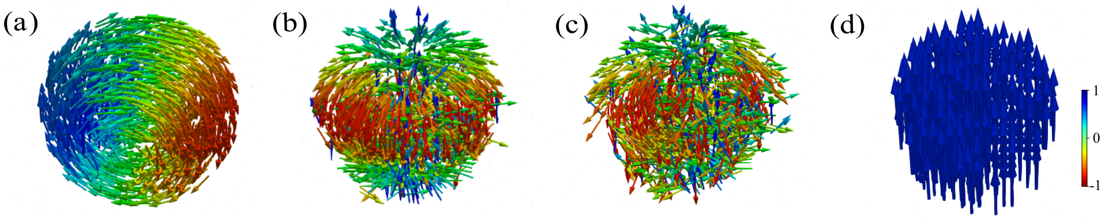

Figure 4.4: Effect of defect concentration on the spin structure. Snapshots of spin structures are shown for 40 nm diameter Fe spheres with different defect concentrations x_d ($\mu_0 H_0$ = 0.02 T). (a) No defects ($x_\mathrm{d} = 0\,\%$), (b) $x_\mathrm{d} = 5\,\%$, (c) $x_\mathrm{d} = 15\,\%$, and (d) $x_\mathrm{d} = 0\,\%$ with $E_\mathrm{d} = 0$. Figure taken from [1].

4.2 Effect of Pore-Type Defects on Spin Structure and Magnetization

The effect of the defect concentration x_d on the spin configurations of Fe spheres with a diameter of 40 nm are shown in Fig. 4.4. The external magnetic field ($\mu_0 H_0$ = 0.02 T) is applied along the z axis. Note that in the actual magnetic SANS simulations the random anisotropy direction across ~ 100 angles relative to $\mathbf{H}_0$ are selected. Initially, all the structures in Fig. 4.4 were fully magnetized. However, for the purpose of comparison, the easy axis was kept the same in Fig. 4.4(a)–(d). The spin configuration for $x_\mathrm{d} = 0\,\%$ [Fig. 4.4(a)] exhibits a vortex-type structure, which is consistent with the findings in [10]. However, when the defect concentration x_d is increased, the structure becomes progressively disordered [Fig. 4.4(b) and (c)]. In the case of the particle size $D = 40$ nm considered here, which is larger than the critical single-domain size of Fe ($D_\mathrm{c} \cong 13.6$ nm), the vortex structure observed in Fig. 4.4(a) is primarily due to the dipolar interaction. By omitting the dipolar self-energy ($E_\mathrm{d} = 0$), a uniform spin configuration is obtained [see Fig. 4.4(d)]. For $x_\mathrm{d} = 0\,\%$ and small applied fields, the vortex structure is observed for particle sizes $D \gtrsim 20$ nm. Overall, it can be observed that the addition of defects significantly alters the vortex-type spin structure towards more disordered configurations, particularly for $D = 40$ nm.

Figure 4.5 presents the reduced hysteresis curves $m_z(H_0) = M_z(H_0)/M_\mathrm{s}^{*}$ for different values of $x_\mathrm{d} \sim 0$–$20\,\%$. It is important to note that the magnetization is

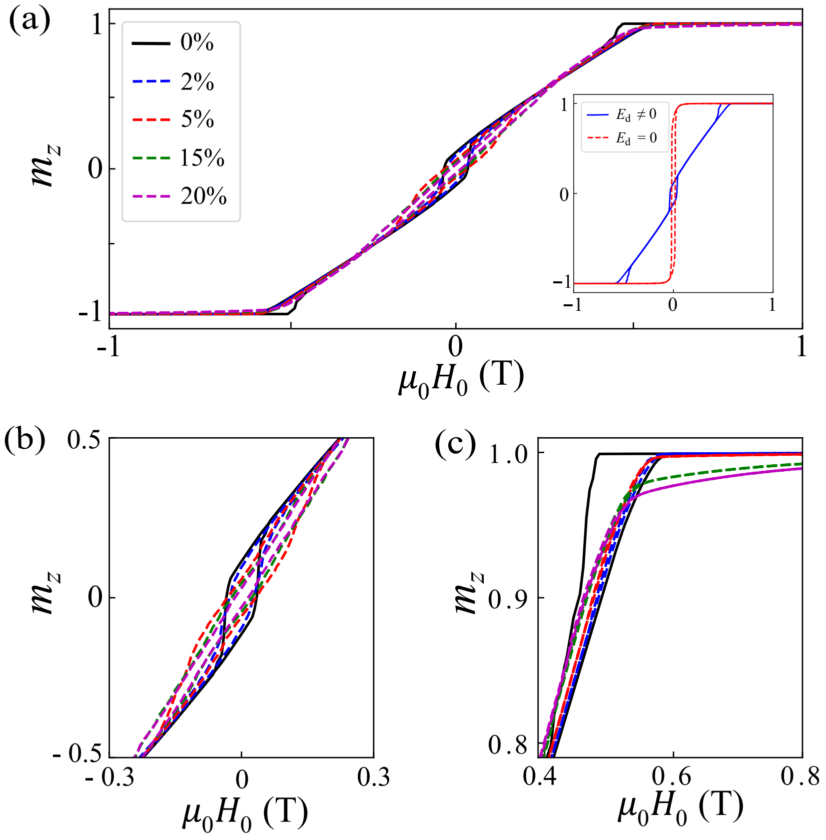

Figure 4.5: (a) Effect of defect concentration x_d (see inset) on the randomly-averaged magnetization curves of Fe spheres with a diameter of 40 nm. (b) and (c): Zoomed-in view of $m_z(H_0)$ around $H_0 = 0$ (b) and $\mu_0 H_0 = 0.6\,\mathrm{T}$ (c). The inset in (a) compares the magnetization curves of defect-free Fe spheres for zero and nonzero dipolar energy E_d. Figure taken from [1].

normalized by the defect concentration, where M_s^* is given by $M_\mathrm{s}^* = (1 - x_\mathrm{d}) M_\mathrm{s}$. As expected, an increase in x_d leads to a decrease in the magnetization, especially in the remanent state and close to the saturation regime [compare Fig. 4.5(b) and (c)]. To provide more quantitative information, the reduced remanent magnetization m_r decreases from approximately 0.11 at $x_\mathrm{d} = 0\,\%$ to around 0.04 at $x_\mathrm{d} = 20\,\%$, while the coercive field decreases from 35 mT at $x_\mathrm{d} = 0\,\%$ to 18 mT at $x_\mathrm{d} = 20\,\%$. Additionally, the saturation field increases from approximately 0.48 T for $x_\mathrm{d} = 0\,\%$ to around 0.53 T for $x_\mathrm{d} = 20\,\%$. The inset in Fig. 4.5(a) illustrates the effect of the dipolar interaction (for $x_\mathrm{d} = 0\,\%$). When $E_\mathrm{d} = 0$, the $m_z(H_0)$ loop has a rectangular shape, fully consistent with the predictions of the Stoner-Wohlfarth model (see Section 2.6). In this case, the reduced remanence is approximately

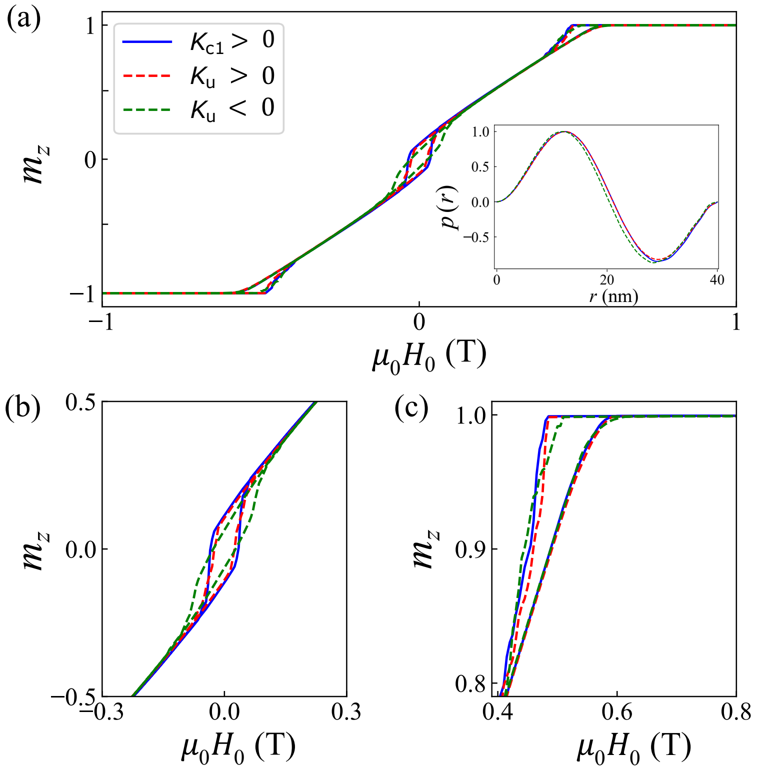

Figure 4.6: Effect of the symmetry of the magnetic anisotropy (cubic or uniaxial) on the randomly-averaged magnetization curve $m_z(H_0)$ and pair distance distribution function $p(r)$ of Fe spheres with a size of 40 nm (defect concentration $x_{\mathrm{d}} = 0\,\%$, see inset). (b) and (c): Zoomed-in view of $m_z(H_0)$ around $H_0 = 0$ (b) and $\mu_0 H_0 = 0.6\,\mathrm{T}$ (c). The anisotropy constants K_{u} and K_{c1} have the same magnitude. The inset in (a) shows the normalized pair distance distribution function $p(r)$ corresponding to each type of magnetic anisotropy.

0.83 and the coercivity is $0.33 \times 2K_{\mathrm{c1}}/M_{\mathrm{s}} \cong 18\,\mathrm{mT}$ [14]. However, when the dipolar interaction is present, two regions with significant hysteresis are observed. One region occurs at high field, around 0.5 T [Fig. 4.5(c)], indicating the departure from the single-domain state. The other region is observed around the remanent state [Fig. 4.5(b)], where the vortex spin structure emerges. In the analysis of the SANS observables [$d\Sigma_{\mathrm{M}}/d\Omega$, $p(r)$, $c(r)$] in Section 4.3, the emphasis will be on these two field regions.

Figure 4.6 illustrates the effect of the symmetry of the magnetic anisotropy (cubic or uniaxial) on the randomly-averaged magnetization curve $m_z(H_0)$ and the pair distance distribution function $p(r)$ (as a representative of the SANS observables). Simulations were carried out for a positive and negative uniaxial

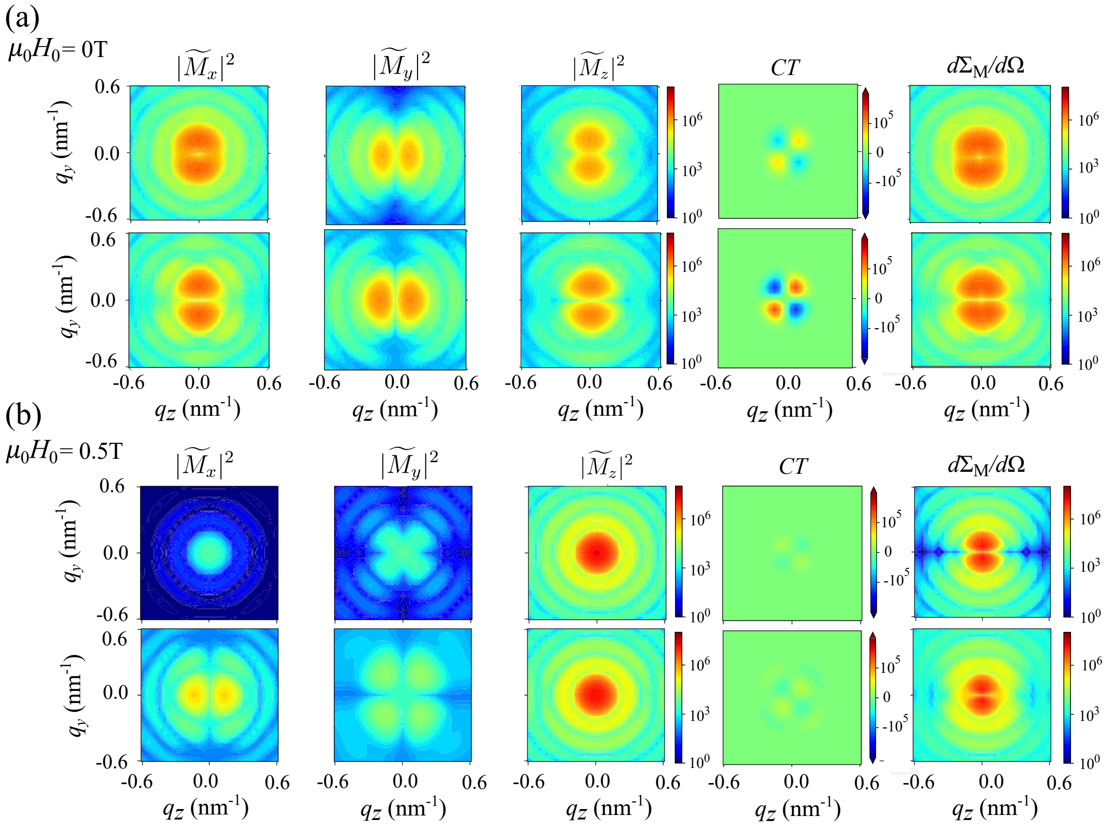

Figure 4.7: (a) Two-dimensional Fourier components $|\widetilde{M}_x|^2$, $|\widetilde{M}_y|^2$, $|\widetilde{M}_z|^2$, $CT = -(\widetilde{M}_y\widetilde{M}_z^* + \widetilde{M}_y^*\widetilde{M}_z)$, and the magnetic SANS cross section $d\Sigma_{\mathrm{M}}/d\Omega$ (in units of cm^{-1}) of 40-nm-sized Fe spheres at $\mu_0H_0 = 0\,\mathrm{T}$. Upper row is for a defect concentration of $x_{\mathrm{d}} = 0\,\%$, lower row is for $x_{\mathrm{d}} = 15\,\%$. (b) Same as in (a), but for $\mu_0H_0 = 0.5\,\mathrm{T}$. Logarithmic color scale is used for all quantities except for the CT values, which are plotted on a linear color scale. Figure adapted from [1, 11].

anisotropy constant K_{u} having the same magnitude as the cubic anisotropy K_{c1} ($x_{\mathrm{d}} = 0\,\%$); $K_{\mathrm{u}} > 0$ corresponds to an easy-plane and $K_{\mathrm{u}} < 0$ to an easy-axis anisotropy. The figure depicts that there is no discernible distinction between $K_{\mathrm{c1}} > 0$ and $K_{\mathrm{u}} > 0$ in both the vicinity of the remanent state [Fig. 4.6(b)] and within the range of 0.5 T [Fig. 4.6(c)]. Negative K_{u} results in a somewhat different $m_z(H_0)$ behavior in the low-field region. The inset in Fig. 4.6(a) displays the pair distance distribution function $p(r)$ for each type of magnetic anisotropy, illustrating that the differences are negligible.

4.3 Effect of Defects on the Magnetic SANS Observables

In this section, we discuss the effect of the porous defects on the magnetic SANS cross section $d\Sigma_{\mathrm{M}}/d\Omega$ and on the pair distance distrubution function $p(r)$ [and the correlation function $c(r) = p(r)/r^2$]. Figure 4.7 displays the two-dimensional magnetic SANS cross section $d\Sigma_{\mathrm{M}}/d\Omega$ along with the Fourier components $|\widetilde{M}_x|^2$, $|\widetilde{M}_y|^2$, $|\widetilde{M}_z|^2$, $CT = -(\widetilde{M}_y\widetilde{M}_z^* + \widetilde{M}_y^*\widetilde{M}_z)$ at remanence and at $\mu_0 H_0 = 0.5\,\mathrm{T}$ and for two different values of the defect concentration x_{d}; Fig. 4.7(a) corresponds to $x_{\mathrm{d}} = 0\,\%$ (upper row) and $x_{\mathrm{d}} = 15\,\%$ (lower row) at $\mu_0 H_0 = 0\,\mathrm{T}$, while Fig. 4.7(b) is the same as (a), but for $\mu_0 H_0 = 0.5\,\mathrm{T}$. Note that the Fourier components are multiplied by the constant $8\pi^3 V^{-1} b_{\mathrm{H}}^2$ in order to have the same unit as $d\Sigma_{\mathrm{M}}/d\Omega$ [compare Eq. (2.26)].

In the remanent state for both cases $x_{\mathrm{d}} = 0\,\%$ and $x_{\mathrm{d}} = 15\,\%$, we see that the $d\Sigma_{\mathrm{M}}/d\Omega$ are vertically elongated [Fig. 4.7(a)]. Moreover, the Fourier components $|\widetilde{M}_x|^2$, $|\widetilde{M}_y|^2$, $|\widetilde{M}_z|^2$ exhibit only a small variation with the defect concentration, particularly in terms of their angular anisotropy. The cross term $CT = -(\widetilde{M}_y\widetilde{M}_z^* + \widetilde{M}_y^*\widetilde{M}_z)$ becomes larger when defects are present. The Fourier components $|\widetilde{M}_x|^2$, $|\widetilde{M}_y|^2$, and $|\widetilde{M}_z|^2$ contribute with similar orders of magnitude to the scattering in the remanent state. On the other hand, near saturation at $0.5\,\mathrm{T}$ [Fig. 4.7(b)], $d\Sigma_{\mathrm{M}}/d\Omega$ is dominated by the $|\widetilde{M}_z|^2$ Fourier component and shows the expected $\sin^2\theta$ angular anisotropy, which is the hallmark of a uniform spin configuration [compare Eq. (2.26)]. The contribution of the transverse Fourier components $|\widetilde{M}_x|^2$ and $|\widetilde{M}_y|^2$ to $d\Sigma_{\mathrm{M}}/d\Omega$ is much weaker than the longitudinal contribution $|\widetilde{M}_z|^2$. At $0.5\,\mathrm{T}$, $|\widetilde{M}_x|^2$ changes from isotropic to a $\cos^2\theta$-type anisotropy in the presence of defects. Meanwhile, $|\widetilde{M}_y|^2$ displays a more pronounced clover-leaf-type pattern in the defective case.

The CTs change their sign at the borders between the quadrants on the detector, e.g., in Fig. 4.7(a) we see that $CT > 0$ for $0^\circ < \theta < 90^\circ$, $CT < 0$ for $90^\circ < \theta < 180^\circ$, and so on. We note that the CT needs to be multiplied with

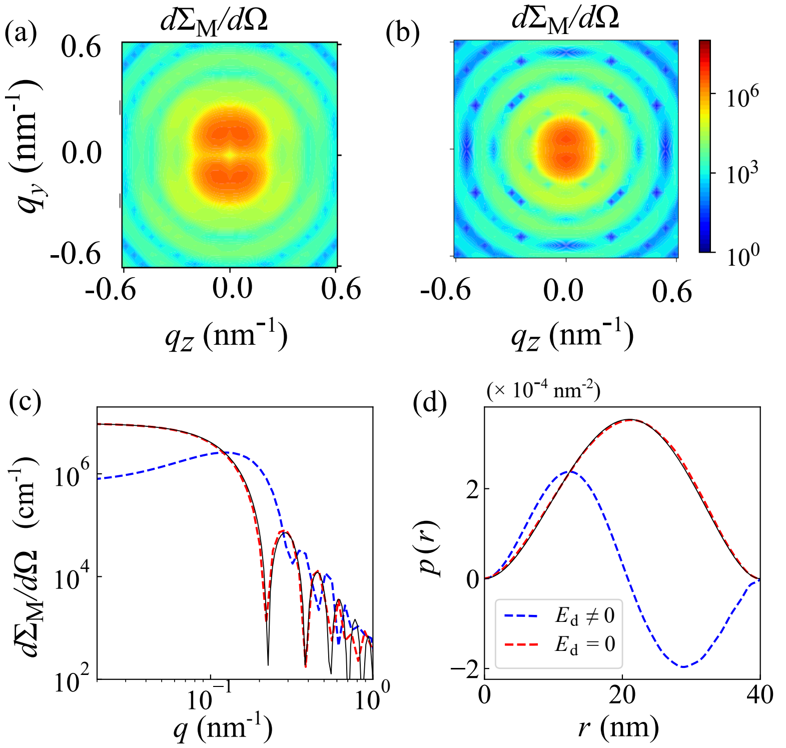

Figure 4.8: Influence of the dipolar interaction on the SANS observables for $D = 40\,\mathrm{nm}$, $x_d = 2\,\%$, and $\mu_0 H_0 = 0\,\mathrm{T}$. (a) $d\Sigma_M/d\Omega$ with E_d (logarithmic color scale), (b) $d\Sigma_M/d\Omega$ without E_d (logarithmic color scale), (c) azimuthally-averaged $d\Sigma_M/d\Omega$ (log-log scale), and (d) pair distance distribution function $p(r)$. The analytical results for uniformly magnetized spheres are represented by the thin black lines in (c) and (d). Figure taken from [1].

$\sin\theta\cos\theta$ in order to obtain the corresponding contribution to the magnetic SANS cross section [compare Eq. (2.26)]. We also emphasize that the $CT\sin\theta\cos\theta$ contribution to $d\Sigma_M/d\Omega$ can be negative, in contrast to the other three contributions, which are strictly positive. Using the inequality $|\widetilde{M}_y\cos\theta - \widetilde{M}_z\sin\theta|^2 \geq 0$, it is easily seen that the contribution $CT\sin\theta\cos\theta$ is, however, always smaller than the sum of the other terms (as it must be). The results in Fig. 4.7 underline that, generally, the Fourier components in the magnetic SANS cross section are anisotropic functions of the angle θ.

The angular anisotropy of the magnetization Fourier components is caused by the dipolar interaction [92], which is a long-range, nonlocal, and anisotropic magnetic energy term. Figure 4.8 compares, at remanence, results for $d\Sigma_M/d\Omega$ with and without the dipolar energy E_d. It is seen that $d\Sigma_M/d\Omega$ is highly anisotropic (elongated along the vertical direction) when E_d is included in the computations

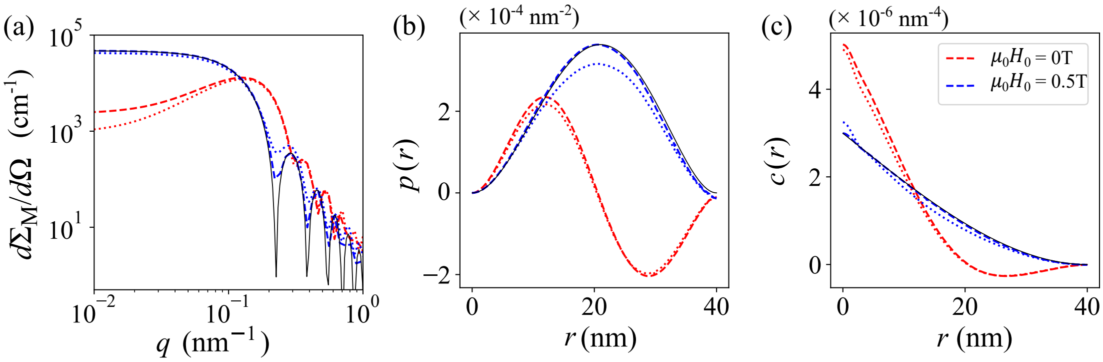

Figure 4.9: (a) Azimuthally-averaged magnetic SANS cross section $d\Sigma_{\mathrm{M}}/d\Omega$ (log-log scale), (b) $p(r)$, and (c) $c(r)$ for applied magnetic fields of 0 T and 0.5 T. The dashed lines represent the case with $x_{\mathrm{d}} = 0\,\%$, the dotted lines represent the case with $x_{\mathrm{d}} = 15\,\%$, and the thin black lines correspond to the analytically-known (defect-free) uniform cases for both $p(r)$ and $c(r)$. Figure taken from [1].

[Fig. 4.8(a)], while it becomes weakly anisotropic (slightly elongated along the vertical direction) when $E_{\mathrm{d}} = 0$ [Fig. 4.8(b)]. For $E_{\mathrm{d}} = 0$, the spin structure remains essentially uniform throughout the magnetization process [compare inset in Fig. 4.5(a) and related text] and one observes the analytical sphere form factor results (thin black lines) for the azimuthally-averaged $d\Sigma_{\mathrm{M}}/d\Omega$ [Fig. 4.8(c)] and the pair-distance distribution function $p(r)$ [Fig. 4.8(d)]. The results in Fig. 4.8 emphasize the importance of considering complex dipolar-field-induced nonuniform spin textures for the understanding of magnetic SANS patterns. We emphasize, however, that the dipolar energy might be of minor relevance for smaller-sized (nearly uniformly magnetized) nanomagnets and in the presence of the Dzyaloshinskii-Moriya interaction, which may give rise to flux-closure-type magnetization patterns [93, 94].

The results for the 2π azimuthally-averaged $d\Sigma_{\mathrm{M}}/d\Omega$ and for the correlation functions $p(r)$ and $c(r)$ are shown in Fig. 4.9 and support the findings from the analysis of the two-dimensional SANS cross sections. Specifically, they indicate a weak dependence on the defect concentration x_{d}. The presence of a vortex-type real-space spin structure can be observed in Fig. 4.4(a), which is characterized by an oscillatory behavior in $p(r)$ [as seen in Figs. 4.8(d) and 4.9(b)]. This oscillatory behavior appears to be relatively stable even when spin perturbations are induced by hole-type defects. Additionally, it is worth noting that there is no Guinier behavior ($d\Sigma_{\mathrm{M}}/d\Omega \propto \exp[-\frac{1}{5}(qR)^2]$) observed at low momentum transfers q and for small fields, as shown in Fig. 4.9(a). Only when the field strength increases, resulting in a more uniform spin structure, does the system exhibit a Guinier-type behavior. This can also be observed in Fig. 4.10(a), which shows the field dependence of $d\Sigma_{\mathrm{M}}/d\Omega$ for $x_{\mathrm{d}} = 15\,\%$. The presence of internal spin disorder causes a shift of the characteristic form-factor oscillations towards larger q values (smaller structures) and smears out these features. This effect resembles the influence of a particle-size distribution and/or instrumental resolution, as can be seen by comparison to Fig. 4.8(c) and Fig. 4.9(a).

As the field increases, the values of $p(r)$ and $c(r)$ in Fig. 4.10 tend to approach the analytical expressions for uniformly magnetized spheres, which are given by Eq. (2.37). However, it is important to consider that the microstructure of the nanoparticles with a high density of defects resembles a porous structure. This can be seen in Fig. 4.3, where the defect cells have a volume of $2 \times 2 \times 2\,\mathrm{nm}^3$. Magnetic voids of this nature represent a significant perturbation in the microstructure, leading to a sudden jump in the saturation magnetization and to the generation of stray-field torques that result in spin disorder. Consequently, when the nanoparticles (with defects) approach a state of uniform magnetization at high fields, it is expected that their $c(r)$ values at small and intermediate r will exhibit slight deviations from the completely uniform scenario [compare to Fig. 4.9(c) and Fig.4.10(c)]. The resolution of the feature at small r is more pronounced in $c(r)$ as compared to $p(r)$ (due to the r^2 factor). This can be see in Fig. 4.9(b), where at 0.5 T the overall shape of $p(r)$ remains unchanged (for $x_{\mathrm{d}} = 0\,\%$ and $x_{\mathrm{d}} = 15\,\%$) and only the maximum is decreased with increasing x_{d}.

The investigation of the correlation function $c(r)$ as r approaches zero is a topic of interest as it sheds light on the characteristics of the scattering contrast [95]. When a sample consists of distinct regions with constant (uniform) scattering length density separated by sharp interfaces, the correlation function

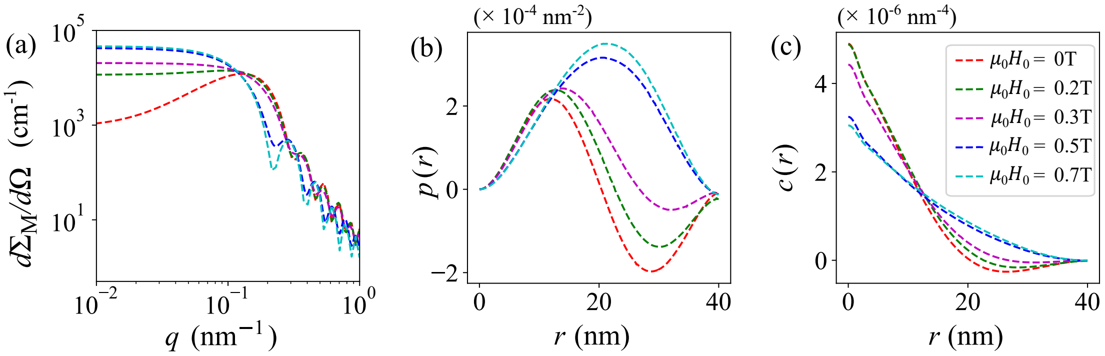

Figure 4.10: Field dependence of (a) the azimuthally-averaged $d\Sigma_{\mathrm{M}}/d\Omega$ (log-log scale), (b) $p(r)$, and (c) $c(r)$. Simulations were made for a defect concentration of $x_{\mathrm{d}} = 15\,\%$. Figure taken from [1].

exhibits a nonzero slope at the origin (compare, e.g., Eqs. (2.36) and (2.37) for uniformly magnetized spherical nanoparticles). This behavior is commonly referred to as the Porod law, which predicts that the SANS cross section has an asymptotic dependency of q^{-4}, as derived e.g. in Ref. [64]. By contrast, structures that have a nonuniform scattering length density profile, such as the smoothly-varying magnetization profiles $\mathbf{M}(\mathbf{r})$ of micromagnetics, are distinguished by a $c(r)$ that shows a zero slope at $r = 0$ and correspondingly steeper power-law exponents of the magnetic SANS cross section [4, 42]. In the present simulations, we are dealing with a system with a potentially nonuniform magnetization on one side of the interface (inside the particle) and a zero magnetization on the other side of the interface. The behavior of $c(r)$ at small distances also depends on the spin distribution in the vicinity of the surface and, therefore, on the surface anisotropy and the related boundary conditions for the magnetization. This question deserves a separate consideration and is beyond the scope of the present PhD project.

4.4 Effect of a Particle-Size Distribution Function

In SANS experiments on nanoparticles one always has to deal with a distribution of particle sizes and shapes. The size of a particle has an important effect on its spin structure; for instance, smaller particles generally tend to be uniformly magnetized, whereas larger particles may exhibit inhomogeneous spin structures [37]. It is therefore also of interest to study the influence of a distribution of particle sizes on the magnetic SANS observables $d\Sigma_{\mathrm{M}}/d\Omega$, $p(r)$, and $c(r)$ (see also Appendix D).

In Ref. [1], we have used a lognormal distribution function for this purpose, which is defined as [96]:

$$f(D) = \frac{1}{\sqrt{2\pi} D \log\sigma} e^{-\frac{1}{2}\left(\frac{\log D - \log D_0}{\log\sigma}\right)^2}, \tag{4.7}$$

where D_0 is the median and σ the variance of the distribution ($\int_0^\infty f(D)dD = 1$). For the above function, the mean particle size $\overline{D}$ [first moment of $f(D)$] is related to the parameters of the distribution as $\overline{D} = D_0 e^{\frac{(\log\sigma)^2}{2}}$. For a given defect concentration x_{d} and field H_0, randomly averaged magnetic SANS sections were computed for particle diameters D ranging between 10 nm and 100 nm in binning intervals of $\Delta D = 2\,\mathrm{nm}$. The magnetic SANS cross section averaged over the distribution, $\langle d\Sigma_{\mathrm{M}}/d\Omega\rangle_f$, is computed as:

$$\left\langle\frac{d\Sigma_{\mathrm{M}}}{d\Omega}\right\rangle_f = \sum_k w_k \frac{d\Sigma_{\mathrm{M},k}}{d\Omega}, \tag{4.8}$$

where

$$w_k = \int\limits_{D_k-\Delta D/2}^{D_k+\Delta D/2} f(D)dD. \tag{4.9}$$

denotes the weight of the size class D_k, which can be computed for given values of D_0 and σ. $d\Sigma_{\mathrm{M},k}/d\Omega$ represents the orientationally-averaged magnetic SANS cross section corresponding to the size class D_k. Particle diameters outside of the above interval, i.e., smaller than $D_{\mathrm{min}} = 10\,\mathrm{nm}$ and larger than $D_{\mathrm{max}} = 10\,\mathrm{nm}$, were not considered in this analysis, i.e., $w_k = 0$ for $D < 10\,\mathrm{nm}$ and $D > 100\,\mathrm{nm}$.

Figure 4.11 depicts the evolution of the azimuthally-averaged magnetic SANS cross section $d\Sigma_{\mathrm{M}}/d\Omega$ and of both correlation functions $p(r)$ and $c(r)$ with the width σ of the lognormal distribution at zero field and at 1.0 T (for $D_0 = 40\,\mathrm{nm}$ and $x_\mathrm{d} = 0\,\%$). Note that the $p(r)$ and $c(r)$ are (for each D_0 and σ) normalized to unity after the cross section has been computed according to Eq. (4.8). The $d\Sigma_\mathrm{M}/d\Omega$ [Fig. 4.11(a)] exhibit the "usual" behavior known, e.g., from the study of instrumental broadening, namely a smearing of the form-factor oscillations with increasing σ. The remaining oscillations of $d\Sigma_\mathrm{M}/d\Omega$ for small σ are more pronounced in the high-field regime [Fig. 4.11(d)] than at remanence [Fig. 4.11(a)]. It is generally seen in Fig. 4.11(b) and Fig. 4.11(e) that the $p(r)$ are more affected by the variation of σ than the $c(r)$ [Fig. 4.11(c) and Fig. 4.11(f)], which is related to the r^2 factor [$p(r) = r^2 c(r)$]. For all values of σ does the oscillatory $p(r)$ behavior remain at zero field, and one observes a shift of the maximum in $d\Sigma_\mathrm{M}/d\Omega$ to lower momentum transfers with increasing σ. This is further illustrated in the inset of Fig. 4.11(a), which shows the inverse of the q value of the maximum in $d\Sigma_\mathrm{M}/d\Omega$, q_max^{-1}, versus σ. The shift to smaller q, corresponding to intraparticle real-space correlations on a scale of about 8−14 nm, can be understood by noting that the magnetic SANS cross section scales with the squared particle volume [compare Eq. (2.29)], so that with increasing σ the larger particle sizes in the distribution gain more weight.

For the materials parameters chosen and a spherical particle shape, the vortex structure appears at low fields for particle sizes larger than about $D = 20\,\mathrm{nm}$ and is present at least up to $D = 100\,\mathrm{nm}$ (larger sizes were not taken into account in our simulations) [10]. This explains why we see an oscillatory $p(r)$ at zero field for increasing σ [Fig. 4.11(b)]; in other words, at remanence we have a weighted superposition of vortex structures with different sizes, while at 1.0 T we deal with a weighted superposition of nearly uniformly magnetized spheres [Fig. 4.11(e)]. The global minimum of $p(r)$ at zero field shifts to larger distances with increasing σ, from $r \cong 29\,\mathrm{nm}$ for $\sigma = 1.1$ to $r \cong 50\,\mathrm{nm}$ for $\sigma = 1.6$. For a nonzero defect concentration $x_\mathrm{d} \neq 0$, the behavior of the $d\Sigma_\mathrm{M}/d\Omega$, $p(r)$, and $c(r)$ are qualitatively similar, demonstrating the rather robust character of the

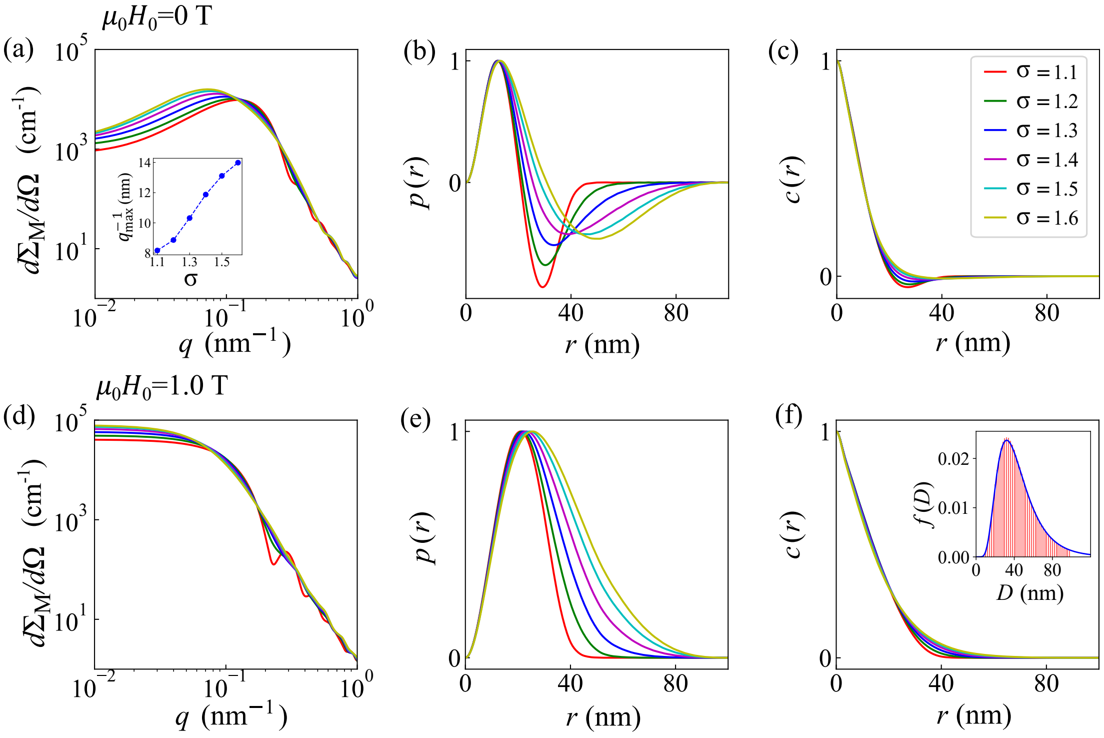

Figure 4.11: Effect of a log-normal particle-size distribution on the azimuthally-averaged magnetic SANS cross section $d\Sigma_{\mathrm{M}}/d\Omega$ and on the correlation functions $p(r)$ and $c(r)$. Upper row [(a)–(c)] is for $\mu_0 H_0 = 0$ T and the lower row [(d)–(f)] is for $\mu_0 H_0 = 1.0$ T. Parameters are $D_0 = 40\,\mathrm{nm}$ and $x_{\mathrm{d}} = 0\,\%$, and σ varies between 1.1 and 1.6 [see inset in (c)]. For each σ, the $p(r)$ and $c(r)$ were normalized to their respective maximum value at 0 T and 1.0 T. The inset in (a) displays $q_{\max}^{-1}$ versus σ, where $q_{\max}$ is the position of the maximum of $d\Sigma_{\mathrm{M}}/d\Omega$ (line is a guide to the eye). The inset in (f) depicts the used size-distribution function $f(D)$ for $D_0 = 40\,\mathrm{nm}$ and $\sigma = 1.6$. For each size class, 40 random particle orientations were used to compute the averaged magnetic SANS cross section. Figure taken from [1].

oscillatory low-field feature in $p(r)$ [1].

4.5 Comparison to Experimental Results

As shown in Ref. [10] and in this thesis (see, e.g., Figs. 4.4 and 4.8), the magnetodipolar interaction gives rise to vortex-like flux-closure structures in a set of spherical magnetic nanoparticles. These magnetization textures can be studied using the correlation function analysis of the corresponding magnetic SANS cross section; their characteristic signature is a damped oscillatory behavior in the correlation function. In Ref. [13], this specific analysis technique has been applied to experimental scattering data to find strong evidence for the existence of vortexlike flux-closure textures within the grains of a Nd-Fe-B magnet. These results will be discussed in the following.

Figures 4.12 and 4.13 summarize the results. Figure 4.12(a) and (b) show the two-dimensional total nuclear and magnetic SANS cross section $d\Sigma/d\Omega$ at a field close to saturation, $\mu_0 H_0 = 10$ T, and at remanence, $\mu_0 H_0 = 0$ T. At the highest field, the total $d\Sigma/d\Omega$ is elongated perpendicular to the applied field $\mathbf{H}_0$, which is indicative for the dominance of longitudinal $|\widetilde{M}_z|^2 \sin^2\theta$ correlations in the unpolarized SANS cross section [compare Eq. (2.26)]. At remanence, we observe an elongation of $d\Sigma/d\Omega$ along $\mathbf{H}_0$, which is known as the so-called spike anisotropy. The origin of this scattering pattern, which becomes more pronounced when subtracting the high-field measurement (a) from the low-field data (b) to obtain the pureley magnetic SANS cross section $d\Sigma_{\mathrm{M}}/d\Omega$ [Fig. 4.12(c)], is related to the magnetodipolar interaction (see Ref. [12] for details).

The magnetic correlation function can be computed from azimuthally-averaged data for $d\Sigma_{\mathrm{M}}/d\Omega$ via the following one-dimensional Fourier transformation:

$$C(r) = \frac{1}{r} \int_0^\infty \frac{d\Sigma_{\mathrm{M}}}{d\Omega}(q) \sin(qr) q dq. \tag{4.10}$$

The results for $C(r)$ are displayed in Fig. 4.12(d) for applied fields ranging between zero field and 4 T; Fig. 4.12(e) shows the corresponding data for the pair distance distribution function $P(r) = r^2 C(r)$. Due to the r^2 factor, a damped oscillatory feature at intermediate r becomes clearly visible in $P(r)$. Based on the simulation results on spherical nanoparticles [1,10], one may relate this feature in the correlation function to a vortex-type spin structure in the Nd-Fe-B magnet. The $C(r)$ of a uniformly magnetized sphere is given by

$$C_0(r) = 1 - \frac{3r}{4R} + \frac{r^3}{16R^3} \tag{4.11}$$

[compare Eq. (2.36)]. For comparison, this function is plotted in Fig. 4.12(d) for $R = 560\,\mathrm{nm}$ and exhibits a slower decay than the experimental data.

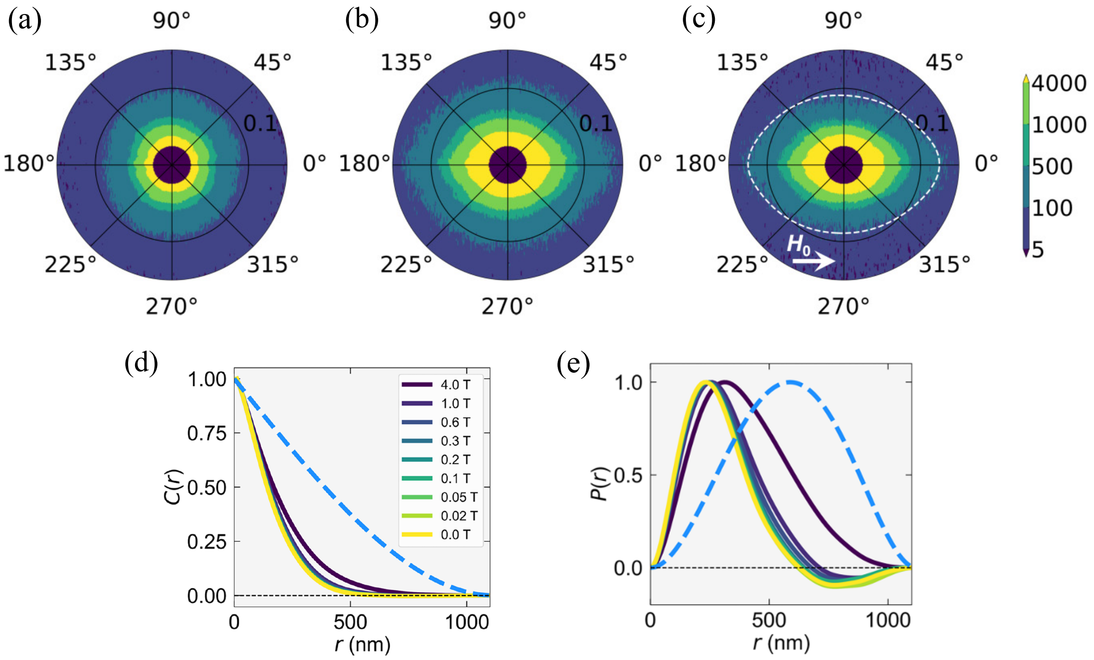

Figure 4.12: Correlation function analysis of the experimental unpolarized SANS cross section of an isotropic Nd-Fe-B permanent magnet. Total nuclear and magnetic SANS at (a) $\mu_0 H_0 = 10\,\mathrm{T}$ (near saturation) and at (b) $\mu_0 H_0 = 0\,\mathrm{T}$ (remanence). (c) Purely magnetic SANS cross section $d\Sigma_{\mathrm{M}}/d\Omega$ obtained by subtracting (a) from (b). The white dashed line in (c) is a guide for the eyes to emphasize the spike-type angular anisotropy due to the magnetodipolar interaction [12]. (d) Experimental field dependence of the magnetic correlation function $C(r)$. Blue dashed line: $C_0(r) = 1 - 3r/(4R) + r^3/(16R^3)$ of a uniformly magnetized sphere with a radius of $R = 560$ nm. (e) Corresponding pair distance distribution function $P(r) = r^2 C(r)$. Figures taken from Ref. [13].

Using the experimental $C(r)$ data in Fig. 4.12(d), a magnetic correlation length L_c can be computed using the following expression (first moment of the correlation function):

$$L_c(H_0) = \frac{\int\limits_0^\infty r C(r, H_0) dr}{\int\limits_0^\infty C(r, H_0) dr}. \tag{4.12}$$

Figure 4.13 shows L_c as a function of H_0. The experimental results (open circles) are compared with simulation data (filled circles) that were obtained on a single 40 nm-sized spherical Fe particle.[1] The $L_c(H_0)$ data are described by the following

---

[1] Due to the large magnetocrystalline anisotropy of Nd-Fe-B, the corresponding single-domain size (for a spherical particle) is relatively large, about 210 nm [60]. To disclose a vortex structure eventually in a Nd-Fe-B sphere requires a much larger particle diameter, on the order of 500 nm, which from a micromagnetic simulation point of view is computationally very challenging. Therefore, to see the general field-dependent behavior of the correlation length of a single vortex, we assumed (for the simulation results displayed in Fig. 4.13) the materials parameters

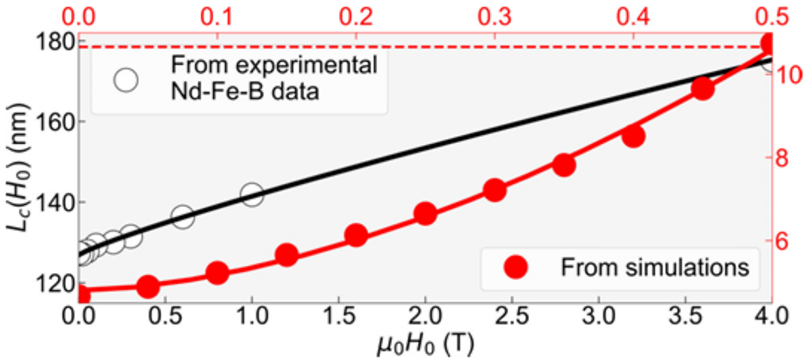

Figure 4.13: Magnetic correlation length L_c as a function of the externally applied magnetic field H_0. Open (filled) circles refer to the experimental (simulation) data (note the different scales). Solid lines: Fit to Eq. (4.13). Figure taken from Ref. [13].

phenomenological power law (solid lines in Fig. 4.13):

$$L_c(H_0) = L_c(H_0 = 0) + \beta H_0^p. \tag{4.13}$$

At low fields, when the vortex is present, one expects an L_c that is significantly smaller than the size of the sphere, while, towards saturation, L_c increases with field and takes on its maximum value. This consideration motivates the above choice for $L_c(H_0)$. Using the analytical expression for $C_0(r)$ in Eq. (4.12), we obtain the limiting value of L_c at saturation as $L_c^{H_0 \to \infty} = \frac{8}{15} R$, or $L_c^{H_0 \to \infty} = 297$ nm using the experimental parameter $R = 560$ nm, and $L_c^{H_0 \to \infty} = 10.7$ nm using $R = 20$ nm from the micromagnetic simulations.

From the fit analysis, we obtain $L_c(0) = 127.0 \pm 0.3$ nm, $\beta = 14.5 \pm 0.5 \mathrm{nm/T}^p$, and $p = 0.86 \pm 0.02$ for the experimental data, and $L_c(0) = 4.8 \pm 0.1$ nm, $\beta = 19.0 \pm 1.0 \mathrm{nm/T}^p$, and $p = 1.70 \pm 0.09$ for the simulation data. As discussed already above, at low magnetic fields, one expects the value of L_c to be significantly smaller than the saturated ones due to the presence of the vortex structure. This prediction, which is very well followed in the simulations (see the red dashed line in

---

of Fe, for which a vortex-type structure already appears for diameters larger than about 20 nm [11,27]. These results are expected to be qualitatively transferable to the case of Nd-Fe-B. The value of 40 nm for the Fe sphere diameter is arbitrary, and we could have equally well chosen a larger size. The simulations on the 40 nm sphere serve as a guide that also allow us to test the predictions for the correlation length [Eq. (4.13)] in the limiting case of a saturated sphere.

Fig. 4.13), also seems to describe the experimental data. However, to demonstrate unambiguously the suitability of Eq. (4.13), further neutron experiments at larger field values are necessary.

The different values for the characteristic power law exponent p in the simulations ($p = 1.70$) and experiment ($p = 0.86$) might be due to the presence of vortex-vortex interactions in the Nd-Fe-B sample. This type of interaction is currently absent in the simulations. To better understand the dependency of the magnetic correlation length L_c on the applied magnetic field requires the inclusion of interacting vortexlike structures in the micromagnetic SANS theory [97, 98].

4.6 Conclusion

In summary, by employing micromagnetic simulations, we have examined the influence of pore-type microstructural defects in spherical magnetic nanoparticles on their magnetic SANS cross section $d\Sigma_{\mathrm{M}}/d\Omega$, pair-distance distribution function $p(r)$, and correlation function $c(r)$. These simulations consider the isotropic exchange interaction, magnetocrystalline anisotropy, dipolar interaction, and an externally applied magnetic field. Notably, the $d\Sigma_{\mathrm{M}}/d\Omega$ and $p(r)$ of nonuniformly magnetized nanoparticles can no longer be accurately described using the superspin model, which assumes a homogeneous spin structure. The dipolar interaction gives rise to various complex magnetization structures and associated anisotropic scattering patterns. For small applied magnetic fields and sufficiently large particle sizes (specifically, for $D \gtrsim 20\,\mathrm{nm}$), the dipolar energy induces a vortex-type spin structure and a concomitant oscillatory feature in the $p(r)$ function. This characteristic signature appears stable against the pore-type defects considered here. The oscillatory shape of $p(r)$ persists even in the presence of a particle size distribution. At low fields, deviations from the Guinier law and intricate real-space correlations are observed. In the current defect modeling approach where defects are represented by computational cells with zero saturation magnetization M_{s}, their effect on the SANS observables is relatively minor. The predominant defect in spherical nanoparticles seems to be the particles' outer surface. A more realistic defect treatment could involve moderate changes in material parameters, such as reducing the saturation magnetization to a lower, but nonzero value and/or diminishing the exchange interaction between the defects and the other cells [99]. Additionally, incorporating the magnetoelastic interaction into the micromagnetic energy functional could be considered. This interaction is currently not implemented in most micromagnetic codes, although recent research efforts are moving in this direction [100]. Similarly, phenomenological models for surface anisotropy, such as Néel anisotropy, which introduce additional boundary conditions on the surface, are also not included in numerical simulations of magnetic SANS. The micromagnetic approach to magnetic SANS involves determining, through magnetic energy minimization, the three-dimensional vector field of the magnetization $\mathbf{M}(\mathbf{r})$. This represents a conceptual shift and is fundamentally different from the traditional approach of finding a scalar function describing the structural saturation-magnetization profile $M_{\mathrm{s}}(\mathbf{r})$ of the particle ensemble. The simulation approach has been successfully used to analyze experimental magnetic SANS data on an isotropic Nd-Fe-B magnet.

Chapter 5

Signature of the Dzyaloshinskii-Moriya Interaction in the SANS Signal of Spherical Nanoparticles

The Dzyaloshinskii-Moriya interaction (DMI) arises in systems with broken inversion symmetry and strong spin-orbit coupling [50, 51]. Examples for materials with intrinsic DMI [75, 76] are MnSi and FeGe which exhibit noncentrosymmetric crystal structures. Other examples where a DMI may appear are materials with a high volume fraction of microstructural defects, where the DMI is a result of the disruption of the structural inversion symmetry at the defect sites [47, 101–108].

The competition between the exchange interaction and the DMI gives rise to various complex chiral magnetization configurations of topological spin structures, such as skyrmions which might be of importance for spintronics applications (see, e.g., Refs. [109–114]). Using micromagnetic simulations, we study the effects of the DMI on the magnetic SANS cross section and the related pair distance distribution function of FeGe nanoparticles. This work will consider a total magnetic Gibbs free energy that consists of the Zeeman energy, magnetostatic energy, exchange energy, magnetocrystalline energy, and the DMI energy. It is worth mentioning that the DMI does not inherently lead to the presence of topological spin structures. Typically, these structures are only detected within a limited region of the associated phase space. The results of this chapter are already published in Ref. [2].

5.1 Details on the Micromagnetic Simulations of FeGe Nanospheres

This project investigates spherical nanoparticles made of FeGe and focuses on the impact of the DMI on the spin-flip SANS cross section and the associated chiral function [54]. The continuum expressions for the energies are the same as those in Section 4.1 (see alsoChapter 3); here, we add the DMI energy as:

$$E_{\mathrm{dmi}} = \mathcal{D} \int \mathbf{m} \cdot \nabla \times \mathbf{m} \, dV, \tag{5.1}$$

where $\mathcal{D}$ represents the bulk DMI constant. The material parameters of FeGe are [93, 115]: $M_{\mathrm{s}} = 384\,\mathrm{kA/m}$, $K_{\mathrm{c1}} = 1.0 \times 10^4\,\mathrm{J/m^3}$, $A = 8.8 \times 10^{-12}\,\mathrm{J/m}$, and $\mathcal{D} = 1.6 \times 10^{-3}\,\mathrm{J/m^{-2}}$. These values yield the following micromagnetic exchange lengths: $l_{\mathrm{M}} = \sqrt{2A/(\mu_0 M_{\mathrm{s}}^2)} = 9.7\,\mathrm{nm}$, $l_{\mathrm{K}} = \sqrt{A/K_{\mathrm{c1}}} = 29.7\,\mathrm{nm}$, and a helical period of $l_{\mathrm{d}} = 4\pi A/\mathcal{D} = 69.1\,\mathrm{nm}$ [93, 116].

Both the magnetic field and magnetization are pseudovectors, which means that they manifest an even behavior under the space-inversion operation ($\mathbf{r} \to -\mathbf{r}$) [117]. The micromagnetic energy expressions [Eqs. (4.1)–(4.4)] (Zeeman, magnetostatic, exchange, and magnetocrystalline energy) remain invariant under space inversion. However, the ∇ (del operator) breaks the space-inversion symmetry, causing the DMI energy [Eq. (5.1)] to be a pseudoscalar that changes sign under $\mathbf{r} \to -\mathbf{r}$. These symmetry properties persist after the variation of the total magnetic Gibbs free energy (with respect to $\mathbf{m}$) is performed to derive the partial differential equations that describe the system's behavior. In this case, the effective field is given by:

$$\mathbf{h}_{\mathrm{eff}} = \mathbf{h}_0 + \mathbf{h}_{\mathrm{d}} + \mathbf{h}_{\mathrm{ani}} + \mathbf{h}_{\mathrm{ex}} + \mathbf{h}_{\mathrm{dmi}}, \tag{5.2}$$

where $\mathbf{h}_{\mathrm{dmi}} = -l_{\mathrm{dmi}} \nabla \times \mathbf{m}$ refers to the field conjugate to the DMI and $l_{\mathrm{dmi}} = 2\mathcal{D}/(\mu_0 M_{\mathrm{s}}^2) = 17.3\,\mathrm{nm}$ is the characteristic length scale of the DMI. On space

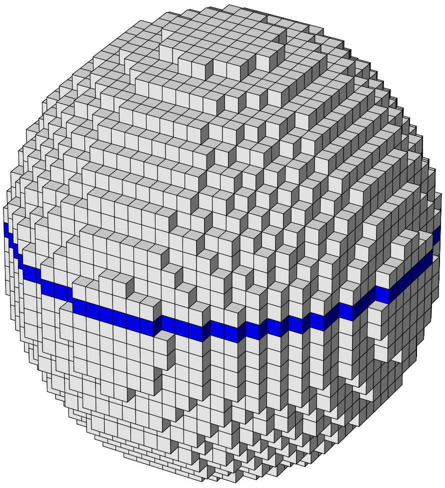

Figure 5.1: Illustration of the discretization of a nanosphere into cubical cells with a size of $2 \times 2 \times 2\,\mathrm{nm}^3$. The blue-colored cells mark the middle layer through the center of the particle for which the topological charge [Eq. (5.6)] has been computed. Note that she small-angle scattering from such a sphere in the saturated state agrees very well with the analytical solution for the sphere form factor [1, 10]. Figure taken from [2].

inversion, only $\mathbf{h}_{\mathrm{dmi}}$ changes its sign in Eq. (5.2).

The simulation model which is used in this project of FeGe nanospheres is shown in Fig. 5.1. The finite-difference method was used to divide the volume of the sphere into cubical cells "i" with a volume of $V_i = 2 \times 2 \times 2\,\mathrm{nm}^3$. Simulations were performed for sphere diameters D ranging between 60 nm to 200 nm. The magnetic moment vector for each cell "i" with volume V_i is given by $\boldsymbol{\mu}_i = \boldsymbol{\mu}_i(\mathbf{r}) = M_{\mathrm{s}} V_i \mathbf{m}_i(\mathbf{r})$, where the vector $\mathbf{m}_i(\mathbf{r})$ represents the unit vector pointing in the direction of the magnetization at a given position $\mathbf{r}$. The winding number [Eq. (5.6)] for the middle layer of the sphere (represented by blue color) has been computed. The simulations were carried out by first applying a large external field to fully align all the spins in the system, then the external field was gradually reduced in steps of typically 5 mT to follow the hysteresis loop. Open boundary conditions were used in the simulations, since we are interested in the scattering behavior of an ensemble of noninteracting single particles having random easy-axis orientations $\mathbf{c}_{1,2,3}$ [compare Eq. (4.3)].

As discussed in Appendix C, the Fourier components $\widetilde{M}_{x,y,x}(\mathbf{q})$ of the magnetization are evaluated in the plane $q_x = 0$ (corresponding to the perpendicular scattering geometry Fig. 2.2) and then used to compute the SANS cross section. In this chapter, we focus on the spin-flip SANS cross section $d\Sigma_{\mathrm{sf}}/d\Omega$ and on the so-called chiral function χ as follows [Eqs. (5.12) and (5.9) below]:

$$\langle f \rangle_{\mathrm{EA}} = \sum_{i=1}^{\mathcal{N}} f_i, \tag{5.3}$$

where the variable f_i represents either $d\Sigma_{\mathrm{sf}}/d\Omega$ or $-iK\chi$ for a spherical particle with diameter D and a specific random easy axis orientation denoted by "i". The SANS observables are examined in the context of a scenario in which the cubic magnetocrystalline anisotropy axes ("EA") of the particles are randomly distributed with respect to the direction of the external magnetic field $\mathbf{H}_0$ (which is parallel to the global $\mathbf{e}_z$ direction). For each value of H_0, micromagnetic simulations are performed considering approximately $\mathcal{N} \sim 500$ random orientations between the easy axis and $\mathbf{H}_0$. It should be noted that the simulations do not take into account interparticle-interference effects, as indicated by Eq. 5.3.

Moreover, in Section 5.5, we will discuss azimuthally-averaged data for the spin-flip SANS cross section $d\Sigma_{\mathrm{sf}}/d\Omega$, which is computed as follows:

$$I_{\mathrm{sf}}(q) = \frac{1}{2\pi} \int_0^{2\pi} \frac{d\Sigma_{\mathrm{sf}}}{d\Omega}(q,\theta)\, d\theta. \tag{5.4}$$

Using Eq. (5.4), the pair distance distribution function is then obtained as:

$$p_{\mathrm{sf}}(r) = r \int\limits_0^{\infty} I_{\mathrm{sf}}(q) \sin(qr) q dq. \tag{5.5}$$

5.2 Skyrmions in FeGe Nanoparticles

Skyrmions, which are of interest in the field of condensed matter physics, are fascinating spin structures that have attracted the attention of researchers since they were first proposed by Tony Skyrme in the 1960s [111,112]. These small-scale particle-like entities resemble whirlpools and represent localized and stable spin configurations. One key characteristic that sets skyrmions apart is their quantized winding number or skyrmion number, which represents the extent of spin rotation within the structure. This winding number is a topological property that imparts skyrmions their robustness against local disturbances. The topological protection of skyrmions makes them particularly interesting for fundamental research, as they provide insights into the underlying principles of condensed matter systems.

In order to investigate the presence of a skyrmion in FeGe nanoparticles, we performed numerical calculations to determine the winding number Q for the middle layer in the x-y plane of a nanoparticle (with the applied field $\mathbf{H}_0$ defining the z direction), as shown in Fig. 5.1 [52, 118]:

$$Q = \frac{1}{4\pi} \int \mathbf{m} \cdot \left(\frac{\partial \mathbf{m}}{\partial x} \times \frac{\partial \mathbf{m}}{\partial y} \right) dxdy, \tag{5.6}$$

where $\mathbf{m}$ is the unit magnetization vector field. For a vortex-type planar configuration with $\mathbf{m} = \frac{1}{2}\{-y, x, 0\}$ and $\nabla \times \mathbf{m} = \{0, 0, 1\}$, the topological charge Q is calculated as 0. In contrast, for skyrmions, Q assumes values of ± 1 [111]. It is important to keep in mind that a Q value of unity supposes that the skyrmion fully fits inside a nanoparticle and that the magnetization vector far away from the skyrmion center approaches a constant value (the so-called ferromagnetic background). This is of course fulfilled by the mathematical trial functions that are used to describe Néel and Bloch skyrmions (e.g., [76]). In the micromagnetic simulations on finite-sized nanoparticles, the magnetodipolar interaction (which is always present) aims to avoid volume and surface charges by demanding that $\nabla \cdot \mathbf{m} = 0$ and $\mathbf{m} \cdot \mathbf{n} = 0$, where $\mathbf{n}$ denotes the local unit normal vector to the surface. This implies that the surface spins (those far away from the skyrmion center, which is supposed to be localized in the sphere center due to symmetry reasons) may not attain a constant value, but vary over the sphere surface. Therefore, in micromagnetic simulations using open boundary conditions on finite-sized systems one should not expect to find Q values very close to unity.

Figure 5.2 depicts the numerically-computed values of the topological charge Q [Eq. (5.6)] of a single nanoparticle for sphere diameters D between 60 nm and

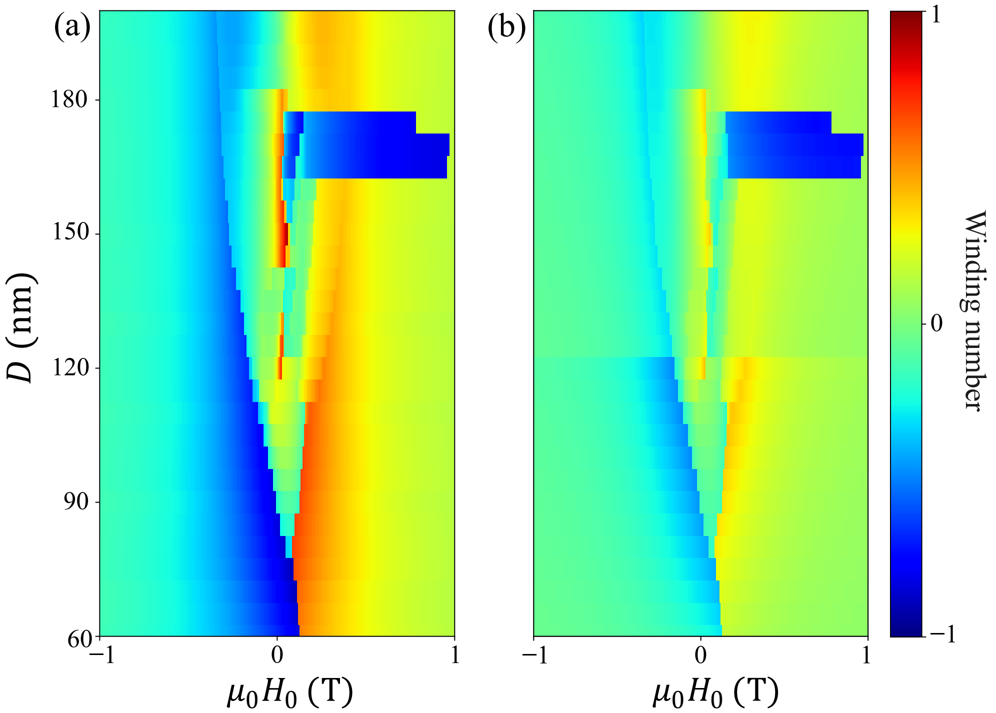

Figure 5.2: The field-diameter phase diagram of an oriented FeGe sphere with particle sizes D ranging between 60 nm and 200 nm and $-1\,\mathrm{T} \leq \mu_0 H_0 \leq 1\,\mathrm{T}$. One of the cubic anisotropy axes is parallel to the externally applied magnetic field $\mathbf{H}_0 \parallel \mathbf{e}_z$. (a) Toplogical charge Q [Eq. (5.6)] numerically calculated for the middle layer in the x-y plane. (b) Q averaged of all layers in the particle. The spacing (resolution) in D and H_0 is, respectively, 5 nm and 5 mT. Figure taken from [2].

200 nm and for applied fields $\mu_0 H_0$ ranging from $-1\,\mathrm{T}$ to $+1\,\mathrm{T}$. In this particular example one of the cubic anisotropy axes has been chosen to be parallel to $\mathbf{H}_0$, so that the results in Fig. 5.2 are representative for an oriented particle, and not for an ensemble of randomly-oriented nanoparticles (to be discussed in Section 5.5). The topological charge has been computed for the middle layer in the x-y plane [Fig. 5.2(a)], and Q has also been averaged over all the layers in the particle [Fig. 5.2(b)]. As can be seen, the averaging procedure results (as expected) in a smearing of the data, leaving however the main features unaltered. Several regions with Q values approaching unity are found indicating a possible skyrmion phase, most prominently is a region $165\,\mathrm{nm} \lesssim D \lesssim 175\,\mathrm{nm}$ and $0.05\,\mathrm{T} \lesssim \mu_0 H_0 \lesssim 0.65\,\mathrm{T}$ where $Q \to -1$.

Figure 5.2 aims to demonstrate that also skyrmionic spin structures may form in individual, favorably-oriented nanoparticles of an ensemble [93]. Changing the direction of the (here cubic) magnetic anisotropy axes of the particle relative to the global direction given by $\mathbf{H}_0$, as it is required for the description of a randomly-oriented nanoparticle ensemble, alters the energetics of the problem and may result in a fraction of the particles being in a skyrmion or a vortex-like state while other particles exhibit textures with zero net topological charge, such as spiral-type textures or even near single-domain structures.

This is illustrated in Fig. 5.3(a)–(d), where the spin structures of two differently-oriented FeGe nanoparticles are shown. In Fig. 5.3(a) we display the structure of a 170 nm-sized FeGe sphere at a field of 5 mT and with one of the cubic anisotropy axes aligned parallel to $\mathbf{H}_0$; Fig. 5.3(b) features the spin distribution in the middle-layer x-y plane, which is characterized by a topological charge of $Q \cong -0.94$. When the particle is oriented with the same cubic anisotropy axis at an angle of ~72° relative to $\mathbf{H}_0$ [Fig. 5.3(c)] a significantly different magnetization distribution is obtained, with $Q \cong -0.39$ in the middle-layer plane [Fig. 5.3(d)]. These considerations imply that for a dilute set of randomly-arranged FeGe nanoparticles, the different spin configurations of differently oriented nanoparticles give rise to a spin-disorder-induced smearing of the SANS observables, even in the absence of a particle-size distribution. This smearing effect is naturally the most pronounced at low fields [see, e.g., Fig. 5.7(a) below].

In the remaining part of this chapter, we will concentrate on the effect of the DMI on the randomly-averaged SANS observables, keeping in mind that a variety of different spin structures may co-exist at a particular field in a set of nanoparticles.

5.3 Symmetry Properties of the Spin-Flip SANS Cross Section and the Chiral Function

This project aims to investigate the elastic differential spin-flip scattering cross section and its associated chiral function. These are fundamental quantities in polarized neutron scattering that can be determined through an experiment in-

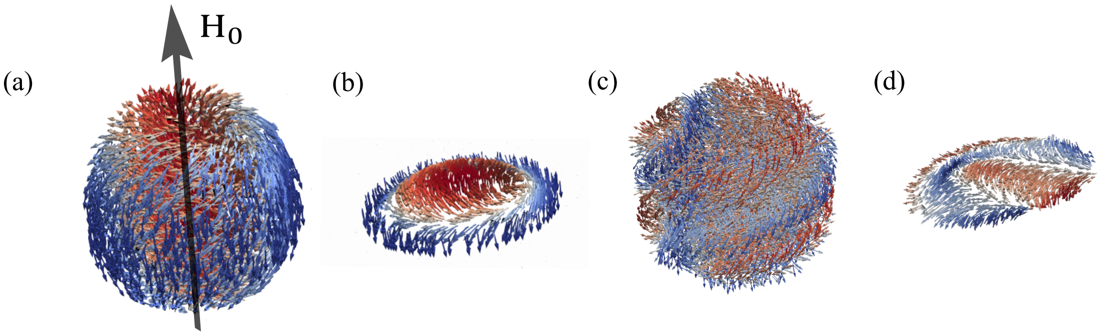

Figure 5.3: (a) Spin structure (snapshot) of a 170 nm-sized FeGe sphere at an external magnetic field of $\mu_0 H_0 = 5\,\mathrm{mT}$. Initially, the spin structure was saturated along $\mathbf{H}_0 \parallel \mathbf{e}_z$. One of the three cubic anisotropy axes was chosen to be parallel to the global $\mathbf{H}_0$ direction. In panel (b) we display the spin structure within the middle-layer x-y plane, resulting in a topological charge of $Q \cong -0.94$. (c) Similar to (a), but with the same cubic anisotropy axis from (a) oriented at an angle of 72° relative to $\mathbf{H}_0$. (d) Same as in (b), but with the cubic axis at 72° relative to $\mathbf{H}_0$ ($Q \cong -0.39$). Figure taken from [2].

volving uniaxial polarization analysis (e.g., [28, 38, 54, 119]). Specifically, we consider a situation where the applied magnetic field $\mathbf{H}_0 \parallel \mathbf{e}_z$ is perpendicular to the wave vector $\mathbf{k}_0 \parallel \mathbf{e}_x$ of the incident neutrons (compare Fig. 2.2). For this scattering geometry, the two spin-flip SANS cross sections $d\Sigma_{\mathrm{sf}}^{+-}/d\Omega$ and $d\Sigma_{\mathrm{sf}}^{-+}/d\Omega$ can be written as (compare Section 2.4.2):

$$\frac{d\Sigma_{\mathrm{sf}}^{+-}}{d\Omega} = \frac{8\pi^3}{V} b_{\mathrm{H}}^2 \Big(|\widetilde{M}_x|^2 + |\widetilde{M}_y|^2 \cos^4\theta + |\widetilde{M}_z|^2 \sin^2\theta \cos^2\theta - (\widetilde{M}_y \widetilde{M}_z^* + \widetilde{M}_y^* \widetilde{M}_z) \sin\theta \cos^3\theta - i\chi \Big), \tag{5.7}$$

$$\frac{d\Sigma_{\mathrm{sf}}^{-+}}{d\Omega} = \frac{8\pi^3}{V} b_{\mathrm{H}}^2 \Big(|\widetilde{M}_x|^2 + |\widetilde{M}_y|^2 \cos^4\theta + |\widetilde{M}_z|^2 \sin^2\theta \cos^2\theta - (\widetilde{M}_y \widetilde{M}_z^* + \widetilde{M}_y^* \widetilde{M}_z) \sin\theta \cos^3\theta + i\chi \Big), \tag{5.8}$$

where V is scattering volume, $b_{\mathrm{H}} = 2.91 \times 10^8\,\mathrm{A}^{-1}\mathrm{m}^{-1}$, θ is the angle between $\mathbf{q}$ and $\mathbf{H}_0$, the complex-conjugated quantity is denoted by an asterisk "$*$", and $\chi = \chi(\mathbf{q})$ denotes the chiral function, which characterizes the nonreciprocity in the polarized neutron scattering cross section. χ is obtained by taking (one-half times) the difference between the two spin-flip SANS cross sections:

$$\begin{aligned} -iK\chi(\mathbf{q}) &= \frac{1}{2}\left(\frac{d\Sigma_{\mathrm{sf}}^{+-}}{d\Omega} - \frac{d\Sigma_{\mathrm{sf}}^{-+}}{d\Omega}\right) \\ &= -iK\left[(\widetilde{M}_x\widetilde{M}_y^* - \widetilde{M}_x^*\widetilde{M}_y)\cos^2\theta - (\widetilde{M}_x\widetilde{M}_z^* - \widetilde{M}_x^*\widetilde{M}_z)\sin\theta\cos\theta\right], \end{aligned} \tag{5.9}$$

where $K = \frac{8\pi^3}{V}b_{\mathrm{H}}^2$. The magnetization Fourier components $\widetilde{M}_{x,y,z}$ can be represented by their real ("R") and imaginary ("I") parts, i.e., $\widetilde{M}_x = \widetilde{M}_x^{\mathrm{R}} + i\widetilde{M}_x^{\mathrm{I}}$, $\widetilde{M}_x^* = \widetilde{M}_x^{\mathrm{R}} - i\widetilde{M}_x^{\mathrm{I}}$ (where $\widetilde{M}_x^{\mathrm{R}} \in \mathbb{R}$ and $\widetilde{M}_x^{\mathrm{I}} \in \mathbb{R}$). By rearranging the expression (5.9), $-iK\chi(\mathbf{q}) \in \mathbb{R}$ can be written as follows:

$$-iK\chi(\mathbf{q}) = -2K\left[(\widetilde{M}_x^{\mathrm{R}}\widetilde{M}_y^{\mathrm{I}} - \widetilde{M}_x^{\mathrm{I}}\widetilde{M}_y^{\mathrm{R}})\cos^2\theta - (\widetilde{M}_x^{\mathrm{R}}\widetilde{M}_z^{\mathrm{I}} - \widetilde{M}_x^{\mathrm{I}}\widetilde{M}_z^{\mathrm{R}})\sin\theta\cos\theta\right], \tag{5.10}$$

which shows that the chiral function vanishes at complete magnetic saturation ($M_x = M_y = 0$), or when the Fourier components of the magnetization $\widetilde{M}_{x,y,z}$ are either purely real-valued or purely imaginary. Moreover, by using the fact that the magnetization vector is a real-valued quantity, i.e., $M_{x,y,z}(\mathbf{r}) \in \mathbb{R}$, one can utilize the well-known result that the real parts of $\widetilde{M}_{x,y,z}(\mathbf{q})$ are even functions of $\mathbf{q}$, while the imaginary parts are odd functions of $\mathbf{q}$. In other words:

$$\widetilde{M}_{x,y,z}^{\mathrm{R}}(\mathbf{q}) = \widetilde{M}_{x,y,z}^{\mathrm{R}}(-\mathbf{q}) \quad \text{and} \quad \widetilde{M}_{x,y,z}^{\mathrm{I}}(\mathbf{q}) = -\widetilde{M}_{x,y,z}^{\mathrm{I}}(-\mathbf{q}),$$

where $\mathbf{q} = \{q_y, q_z\}$ represents the two-dimensional Cartesian scattering vector in the detector plane. Consequently, both terms in Eq. (5.10), which always involve the product of two even functions (e.g., $\widetilde{M}_x^{\mathrm{R}}$ and $\sin\theta\cos\theta$) and one odd function (e.g., $\widetilde{M}_z^{\mathrm{I}}$), are odd functions of $\mathbf{q}$. Therefore, the following symmetry relation holds for the chiral function (odd under spatial inversion of $\mathbf{q}$):

$$iK\chi(\mathbf{q}) = -iK\chi(-\mathbf{q}). \tag{5.11}$$

Table 5.1: Summary of all the possible combinations of symmetry properties (even or odd) of the real-space magnetization components $M_{x,y,z}(\mathbf{r})$ and the ensuing symmetries (real or imaginary) of the Fourier-space magnetization components $\widetilde{M}_{x,y,z}(\mathbf{q})$ and the chiral function χ (zero or nonzero). The case that the $M_{x,y,z}(\mathbf{r})$ are composed of a nonzero even and odd part will always result in a nonzero chiral function. Table taken from [2].

$M_x(\mathbf{r})$	$M_y(\mathbf{r})$	$M_z(\mathbf{r})$	$\widetilde{M}_x(\mathbf{q})$	$\widetilde{M}_y(\mathbf{q})$	$\widetilde{M}_z(\mathbf{q})$	$iK\chi(\mathbf{q})$
odd	odd	odd	imaginary	imaginary	imaginary	zero
even	odd	odd	real	imaginary	imaginary	nonzero
odd	even	odd	imaginary	real	imaginary	nonzero
even	even	odd	real	real	imaginary	nonzero
odd	odd	even	imaginary	imaginary	real	nonzero
even	odd	even	real	imaginary	real	nonzero
odd	even	even	imaginary	real	real	nonzero
even	even	even	real	real	real	zero

Table 5.1 lists the chiral function (zero or nonzero) for all the possible combinations of symmetry properties (odd or even) of the real-space magnetization components. We also refer to the review by Maleev [120] for a discussion of the symmetry properties of the chiral function.

In addition to the difference between $d\Sigma_{\mathrm{sf}}^{+-}/d\Omega$ and $d\Sigma_{\mathrm{sf}}^{-+}/d\Omega$, one can also examine (one-half times) their sum:

$$\begin{aligned}\frac{d\Sigma_{\mathrm{sf}}}{d\Omega} &= \frac{1}{2}\left(\frac{d\Sigma_{\mathrm{sf}}^{+-}}{d\Omega} + \frac{d\Sigma_{\mathrm{sf}}^{-+}}{d\Omega}\right) \\ &= K\Big(|\widetilde{M}_x|^2 + |\widetilde{M}_y|^2\cos^4\theta + |\widetilde{M}_z|^2\sin^2\theta\cos^2\theta \\ &\quad -(\widetilde{M}_y\widetilde{M}_z^* + \widetilde{M}_y^*\widetilde{M}_z)\sin\theta\cos^3\theta\Big),\end{aligned} \tag{5.12}$$

where the quantity $d\Sigma_{\mathrm{sf}}/d\Omega$ is called the (polarization-independent) spin-flip SANS cross section. Based on the foregoing, it is easily seen that $d\Sigma_{\mathrm{sf}}/d\Omega$ is an even function of $\mathbf{q}$ (even under spatial inversion of $\mathbf{q}$) [7]:

$$\frac{d\Sigma_{\mathrm{sf}}}{d\Omega}(\mathbf{q}) = \frac{d\Sigma_{\mathrm{sf}}}{d\Omega}(-\mathbf{q}). \tag{5.13}$$

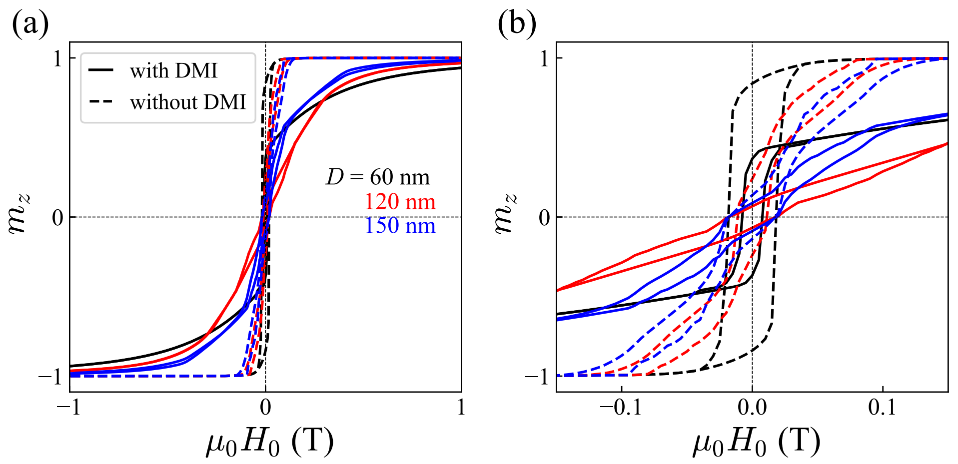

Figure 5.4: (a) Normalized magnetization curves of randomly-oriented FeGe nanoparticles with particle diameters of $D = 60\,\mathrm{nm}$, $120\,\mathrm{nm}$, and $150\,\mathrm{nm}$ (see inset). The solid lines are with DMI and the dashed lines are without DMI. (b) Same as (a), but for $-0.15\,\mathrm{T} \leq \mu_0 H_0 \leq 0.15\,\mathrm{T}$. The reduced remanence of the $D = 60\,\mathrm{nm}$ "sample" is ~0.832 (without DMI), which is very close to the Stoner-Wohlfarth value, suggesting the presence of single-domain particles [14]. Figure taken from [2].

5.4 Effect of DMI on Magnetization

Figure 5.4 illustrates the effect of the DMI on the randomly-averaged magnetization of an ensemble of noninteracting spherical FeGe nanoparticles. Normalized magnetization curves $m_z(H_0)$ for different particle diameters with and withoput the DMI are shown. The black line represents particles with a diameter of $D = 60$ nm, the red line with a diameter of $D = 120\,\mathrm{nm}$, and the blue line with a diameter of $D = 150\,\mathrm{nm}$. The solid lines correspond to simulations with DMI, while the dashed line correspond to simulations without DMI. Figure 5.4(b) shows an enlarged region close to the remanent state. Without DMI, the hysteresis curve for $D = 60\,\mathrm{nm}$ agrees with the predictions of the Stoner-Wohlfart model (see Section 2.6), i.e., the reduced remanence for particles with a positive cubic anisotropy evaluates to $m_\mathrm{r} \cong 0.832$, indicating that the system is in a single-domain state. This is also supported by an estimate for the critical single-domain size of spherical FeGe particles, $D_\mathrm{c} = 72\frac{\sqrt{AK_1}}{\mu_0 M_s^2} \cong 115\,\mathrm{nm}$, which suggests that for particle diameters below 115 nm the system is in a single-domain state. When the

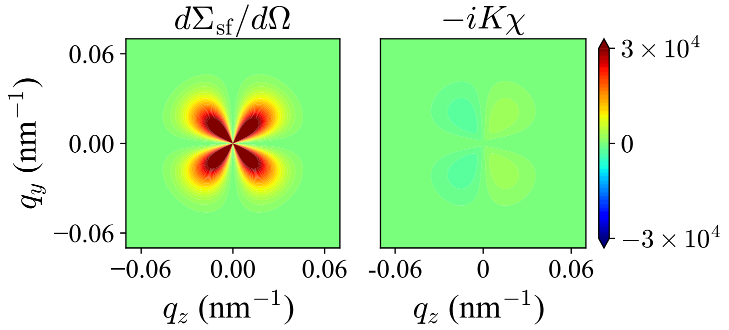

Figure 5.5: (a) The randomly-averaged spin-flip SANS cross section $d\Sigma_{\mathrm{sf}}/d\Omega$ and (b) chiral function $-iK\chi$ of FeGe nanoparticles with a diameter of 170 nm and at a saturating field of $\mu_0 H_0 = 3\,\mathrm{T}$ ($\mathbf{H}_0 \parallel \mathbf{e}_z$).

DMI is included, the remanent magnetization of the particle ensemble is reduced. Similar results were previously reported in Ref. [121].

5.5 Effect of DMI on Spin-Flip SANS Cross Section, Chiral Function, and Correlation Function

Figure 5.5 shows the two-dimensional (2D) spin-flip SANS cross section $d\Sigma_{\mathrm{sf}}/d\Omega$ and the chiral function $-iK\chi$ of 170 nm-sized FeGe nanoparticles at a saturating field of 3 T. In this case, $d\Sigma_{\mathrm{sf}}/d\Omega$ [Fig. 5.5(a)] is determined by the longitudinal magnetization Fourier component $|\widetilde{M}_z|^2$ and exhibits the characteristic $\sin^2\theta\cos^2\theta$ angular anisotropy [compare Eq. (5.12)]. As expected, $-iK\chi$ [Fig. 5.5(b)], and the effect of the DMI, is negligible at saturation, since $M_{x,y} \rightarrow 0$ at 3 T.

The corresponding results for the randomly-averaged $d\Sigma_{\mathrm{sf}}/d\Omega$ and $-iK\chi$ with and without the DMI and at a small applied field of $\mu_0 H_0 = 5\,\mathrm{mT}$ are shown in Fig. 5.6. Figure 5.6(c) and 5.6(f) display examples (snapshots) of real-space spin structures contributing to the respective scattering cross section [Fig. 5.6(c) with DMI and Fig. 5.6(f) without the DMI]. The reduction of the field results in the appearance of various complex $\mathbf{M}(\mathbf{r})$ patterns [compare, e.g., Fig. 5.3(a) and (c)] and in a correspondingly complicated randomly-averaged $d\Sigma_{\mathrm{sf}}/d\Omega$ [Fig. 5.6(a)]. If the DMI is omitted in the simulations, a significantly altered $d\Sigma_{\mathrm{sf}}/d\Omega$ arises [Fig. 5.6(d)], which exhibits (here for 5 mT) a $\sin^2\theta$ type anisotropy, characteristic

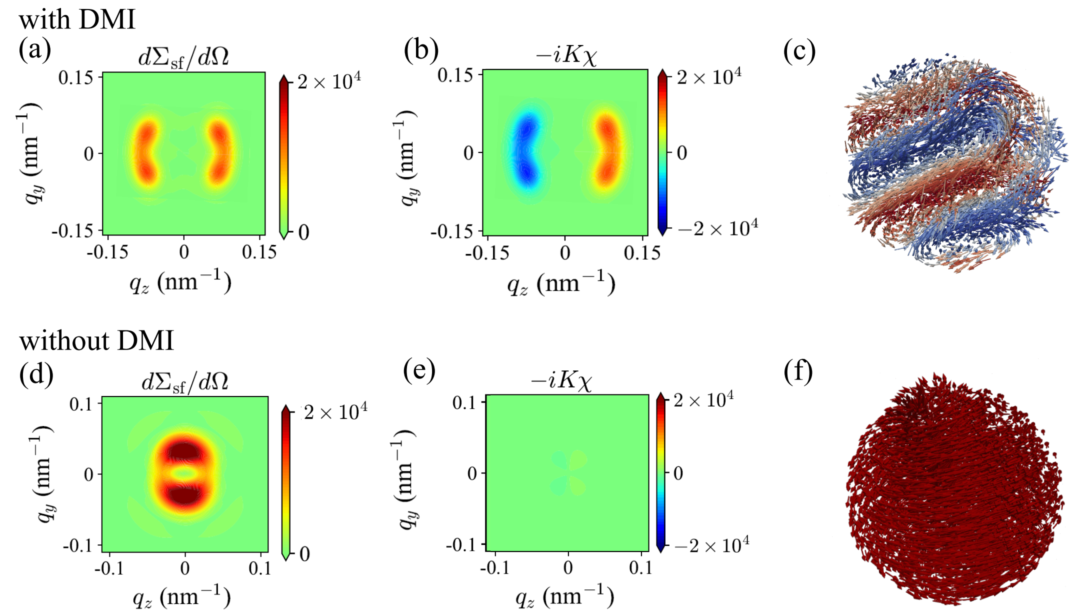

Figure 5.6: (a) $d\Sigma_{\mathrm{sf}}/d\Omega$ and (b) $-iK\chi$ at an applied magnetic field of 5 mT for an ensemble of 500 randomly-oriented FeGe nanoparticles with a diameter of 170 nm. (c) Example for a real-space spin structure at 5 mT. (d)–(f) Corresponding results for $d\Sigma_{\mathrm{sf}}/d\Omega$, $-iK\chi$, and the spin structure without the DMI. Figure taken from [2].

of the saturated state in unpolarized SANS in the $\mathbf{H}_0 \perp \mathbf{k}_0$ scattering geometry [compare Eq. (2.26)].

One of the main results of this project on randomly arranged particle ensembles is that for $60\,\mathrm{nm} \leq D \leq 200\,\mathrm{nm}$ and $-1\,\mathrm{T} \leq \mu_0 H_0 \leq 1\,\mathrm{T}$, the chiral function $-iK\chi$ vanishes when the DMI is not included in the simulations [compare Fig. 5.6(b) and (e) and the corresponding data in Appendix A]; in other words, due to the absence of chirality selection, the individual Fourier cross correlations in the expression for $-iK\chi$ [Eqs. (5.9) and (5.10)] add up to zero in the random average case and no DMI. Similar to previous simulations on Fe nanospheres [1,10], we find dipolar-energy-driven vortex-type structures in FeGe when the DMI is not taken into account [e.g., Fig. 5.6(f)]. The ensemble of vortex configurations exhibit, on the average, an equal amount of clockwise and counterclockwise rotation senses, so that the corresponding chiral function averages to zero. This result is somehow expected (no chirality selection), and the symmetry properties of the chiral function are well known [120], but here we comprehensively study the signature of the DMI on the diffuse SANS cross section of an ensemble of randomly-oriented magnetic nanoparticles.

Figures 5.7 and 5.8 display the results for the azimuthally-averaged neutron data $I_{\mathrm{sf}}(q)$ and the pair distance distribution $p_{\mathrm{sf}}(r)$ [computed using Eqs. (5.4) and (5.5)]. In Fig. 5.7, the effect of the DMI is shown for FeGe particle sizes of $D = 60\,\mathrm{nm}$, $120\,\mathrm{nm}$ and $150\,\mathrm{nm}$ at an applied magnetic field of $\mu_0 H_0 = 20\,\mathrm{mT}$. Fig. 5.8 highlights the field dependence of $I_{\mathrm{sf}}(q)$ and $p_{\mathrm{sf}}(r)$ at a fixed particle size of $D = 170\,\mathrm{nm}$ (including the DMI). While it is challenging to make general statements about the spin structure of individual nanoparticles, we observe the tendency of the formation of periodic domain structures when the DMI is present [see, e.g., Fig. 5.6(c)]. This is evident in the $p_{\mathrm{sf}}(r)$ data, which (for $D = 120\,\mathrm{nm}$ and $D = 150\,\mathrm{nm}$) exhibit three zero crossings with DMI [Fig. 5.7(b)], while only one such zero crossing is observed when the DMI is absent [Fig. 5.7(d)]. The $D = 60\,\mathrm{nm}$ spheres are in a nearly single-domain state without DMI [Fig. 5.7(d)] and exhibit a vortex-type spin structure with DMI [Fig. 5.7(b)].

As depicted in Fig. 5.8, when the field reaches a saturation level of $3\,\mathrm{T}$, the analytical results for a uniformly magnetized sphere are retrieved [yellow dashed line in Fig. 5.8(b)]. However, when the field is decreased to $0.12\,\mathrm{T}$ and $0.02\,\mathrm{T}$, the scattering curves exhibit the previously mentioned blurring caused by spin disorder, i.e., the sample is composed of particles that all have the same structural size D, but their internal spin structures may be different. Therefore, the form factor oscillations (which are most prominent at $3\,\mathrm{T}$) become progressively smeared and damped at lower fields. At large values of q, where structure on a nanometer-scale is probed, all the scattering curves follow the well-known Porod law $I_{\mathrm{sf}}(q) \propto q^{-4}$ [as shown by the black dashed line in Fig. 5.8(a)]. Furthermore, the nucleation of an inhomogeneous spin structure at lower fields leads to the appearance of a peak in the $I_{\mathrm{sf}}(q)$ curve at intermediate momentum transfers, accompanied by a decrease in the value of I_{sf} as $q \to 0$, reflecting the behavior of the average ensemble magnetization.

In order to characterize the way in which the system of randomly-oriented

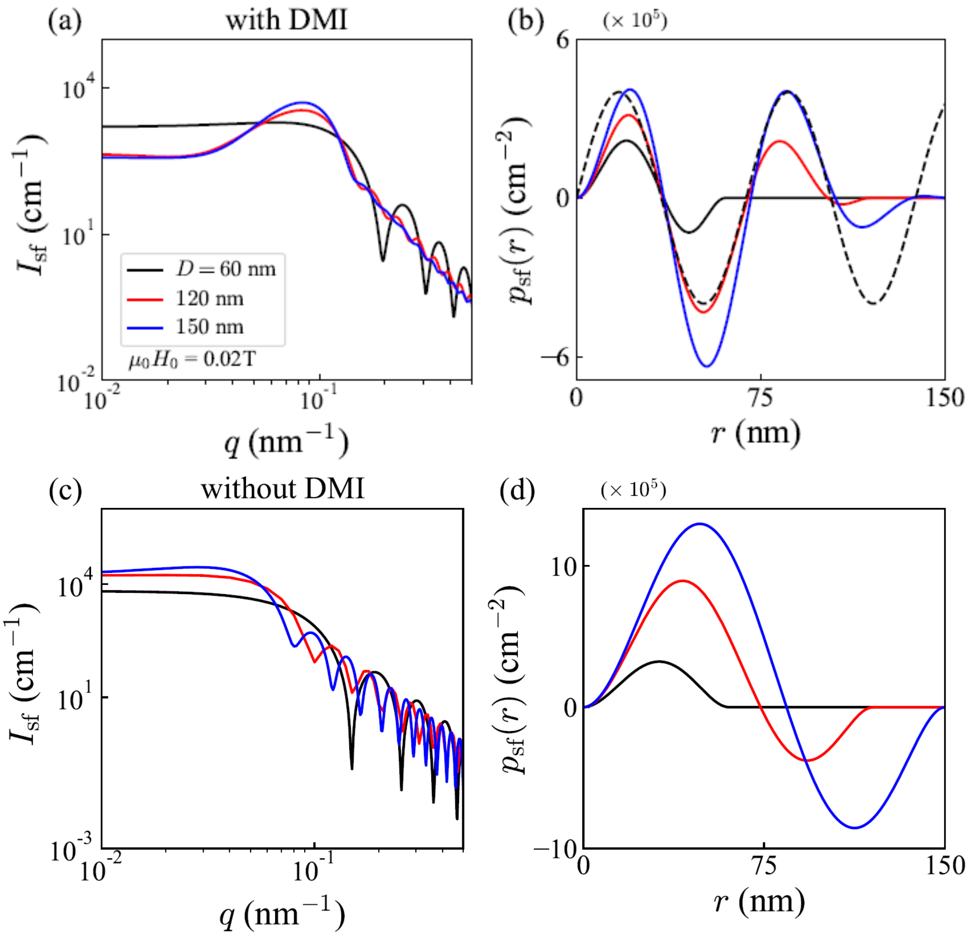

Figure 5.7: (a) $I_{\rm sf}(q)$ and (b) $p_{\rm sf}(r)$ for randomly-oriented FeGe nanoparticles with $D = 60$ nm, 120 nm and 150 nm and at an applied magnetic field of $\mu_0 H_0 = 0.02$ T (see inset). (c) $I_{\rm sf}(q)$ and (d) $p_{\rm sf}(r)$ without DMI. Black dashed line in (b): $p_{\rm sf}(r) \propto \sin(k_{\rm d} r)$ with $k_{\rm d} = 0.09\,{\rm nm}^{-1}$. Figure taken from [2].

FeGe nanoparticles scatters at low fields and for not too small particle sizes (so that a DMI-induced spin modulation appears), we present the following phenomenological expression ("educated guess") for the spin-flip correlation function:

$$c_{\rm sf}(r) = B\, j_0(k_{\rm d} r) \exp(-r/R), \tag{5.14}$$

where B is a scaling constant, $R = D/2$ is the sphere radius, and $j_0(z) = \sin z/z$ denotes the zeroth-order spherical Bessel function that provides a damped oscillation with a wave number of $\sim k_{\rm d}$. We emphasize that Eq. (5.14) does not represent a true particle correlation function, since it extends to infinity and vanishes for $r > D$. The exponential decay forces the spatial extent of $c_{\rm sf}(r)$ to be roughly

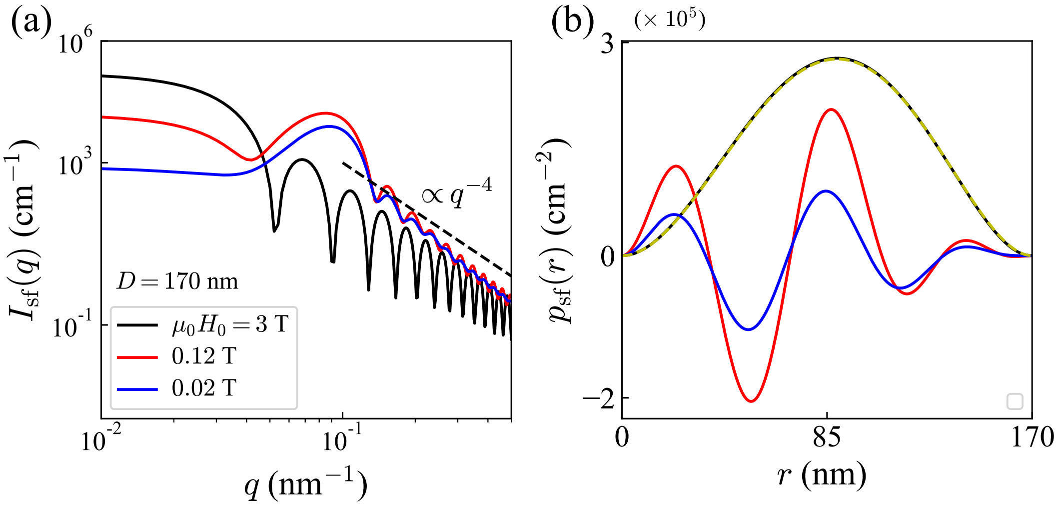

Figure 5.8: (a) $I_{\rm sf}(q)$ and (b) $p_{\rm sf}(r)$ of randomly-oriented FeGe nanoparticles with $D = 170$ nm and at three different applied magnetic fields (3 T, 0.12 T, 0.02 T, see inset). The DMI is included in the simulations. Black dashed line in (a): $I_{\rm sf}(q) \propto q^{-4}$. Yellow dashed line in (b): analytical expression for $p_{\rm sf}(r)$ for a uniformly magnetized sphere [Eq. (2.36)]. Figure taken from [2].

limited to $r \lesssim D$. Equation (5.14) is an easy-to-implement expression that, as we will see below, grasps the main low-field characteristics found in the simulations. The corresponding analytical expression for the spin-flip SANS cross section is given by:

$$\begin{aligned} I_{\rm sf}(q) &= \int\limits_0^{\infty} c_{\rm sf}(r) j_0(qr) r^2 dr \\ &= \frac{2BR^3}{\left[1 + (q - k_{\rm d})^2 R^2\right]\left[1 + (q + k_{\rm d})^2 R^2\right]}, \end{aligned} \tag{5.15}$$

which exhibits a field-independent maximum at $q_{\max} = \sqrt{k_{\rm d}^2 R^2 - 1}/R \cong k_{\rm d}$ and an asymptotic q^{-4} dependency; $I_{\rm sf}(q = 0) = 2BR^3/(1 + k_{\rm d}^2 R^2)^2$.

Figure 5.9 features a comparison between Eqs. (5.14) and (5.15) and the numerically computed $I_{\rm sf}(q)$, $c_{\rm sf}(r)$, and $p_{\rm sf}(r) = r^2 c_{\rm sf}(r)$. Overall, we see that the expressions reproduce the main features of the spin-flip scattering, i.e., a peak at about the helical wavevector $k_{\rm d}$ followed by a q^{-4} Porod decay at large q. The r^2 factor in the definition of $p_{\rm sf}(r)$ amplifies the error at the larger distances. The behavior of $I_{\rm sf}(q)$ at large q does not depend on $k_{\rm d}$.

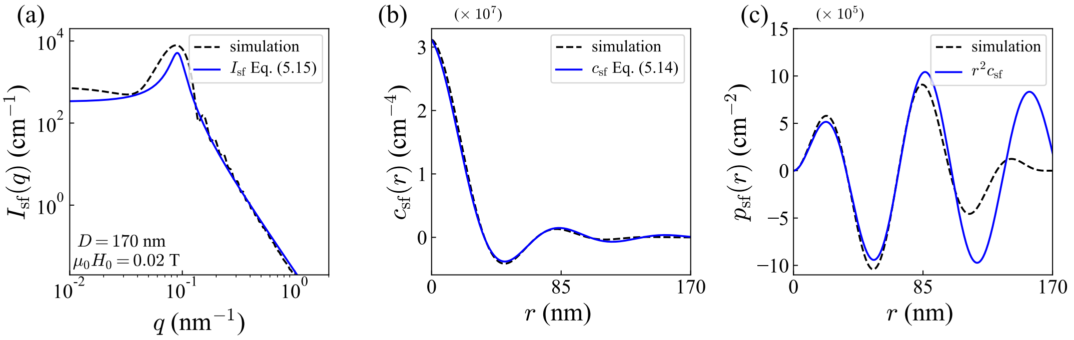

Figure 5.9: Comparison between the simplified analytical model [Eqs. (5.14) and (5.15)] and the numerical micromagnetic simulations. (a) $I_{\mathrm{sf}}(q)$, (b) $c_{\mathrm{sf}}(r)$, and (c) $p_{\mathrm{sf}}(r)$ of randomly-oriented FeGe nanoparticles ($D = 170$ nm and $\mu_0 H_0 = 0.02$ T). Black dashed lines: micromagnetic simulation. Blue solid lines: Eqs. (5.14) and (5.15) (scaled to the simulation data). Figure taken from [2].

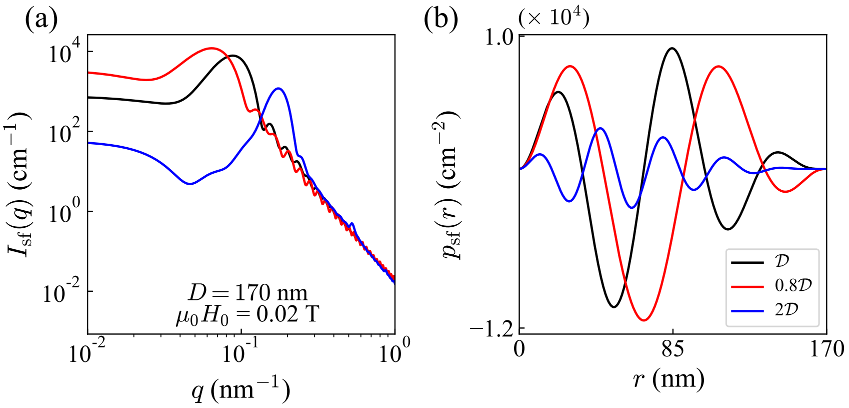

Figure 5.10: Dependence of the randomly-averaged $I_{\mathrm{sf}}(q)$ (a) and $p_{\mathrm{sf}}(r)$ (b) of FeGe nanospheres on the DMI constant (see inset) ($D = 170$ nm and $\mu_0 H_0 = 0.02$ T). The peak maximum in $I_{\mathrm{sf}}(q)$ scales with $k_{\mathrm{d}} = D/(2A)$. Peak positions in (a): 0.062 nm^{-1}, 0.086 nm^{-1}, and 0.172 nm^{-1}. Figure taken from [2].

To confirm that the helical period due to the DMI is indeed observable in the spin-flip SANS cross section, we compare $I_{\mathrm{sf}}(q)$ and $p_{\mathrm{sf}}(r)$ data for different values $\mathcal{D}$ of the DMI constant. Figure 5.10(a) displays $I_{\mathrm{sf}}(q)$ for $D = 170$ nm, $\mu_0 H_0 = 0.02$ T, and for $\mathcal{D}$ values of $\mathcal{D} = 1.6 \times 10^{-3}\,\mathrm{J/m^{-2}}$ (black line), $0.8\mathcal{D}$ (red line), and $2\mathcal{D}$ (blue line). Previous analysis suggests that the peak position of I_{sf} appears at $k_{\mathrm{d}} = \mathcal{D}/(2A)$, so that a shift should occur as $\mathcal{D}$ increases, which is indeed observable in Fig. 5.10(a). The pair distance distribution [Fig. 5.10(b)] exhibits oscillations with a shorter (longer) period as the DMI constant becomes larger (smaller). All these results suggest that the helical period due the DMI is indeed observable in $I_{\mathrm{sf}}(q)$ and $p_{\mathrm{sf}}(r)$ for nanoparticles with sizes larger than the helical period ($D > l_{\mathrm{d}}$) and for small applied magnetic fields.

5.6 Conclusion

To summarize, numerical micromagnetic simulations were used to study the impact of the antisymmetric DMI on the diffuse magnetic spin-flip SANS cross section for a collection of randomly-oriented FeGe nanoparticles. Unlike the other magnetic interactions accounted for in our simulations (isotropic exchange, magnetic anisotropy, dipolar, and Zeeman interactions), the DMI energy is a pseudoscalar that breaks space-inversion symmetry. The relative alignment between the magnetic anisotropy axes of the nanoparticles and the orientation of the externally applied magnetic field can lead to a variety of spin configurations within nanoparticles of a specific size class D (e.g., skyrmions, vortex and spiral type, nearly single domain). This results in an intrinsic broadening of the spin-flip SANS cross section due to spin disorder (even when all particles are of the same size). Within the explored parameter range for particle size ($60\,\mathrm{nm} \leq D \leq 200\,\mathrm{nm}$) and applied magnetic field ($-1\,\mathrm{T} \leq \mu_0 H_0 \leq 1\,\mathrm{T}$), we discovered that the ensemble-averaged chiral function $-iK\chi$ is nonzero exclusively when the DMI is included in the simulations. An intriguing open issue in this context is the correlation between the symmetry properties of the micromagnetic energies (and their conjugate fields) under space inversion and the real and imaginary components of $\widetilde{M}_{x,y,z}(\mathbf{q})$. To address this, one would need to Fourier transform Brown's nonlinear equations, involving complex convolution products that are challenging to compute directly. However, it has been demonstrated in Ref. [46] that within a linearized analytical framework applicable to bulk ferromagnets, a nonzero DMI yields complex $\widetilde{M}_{x,y,z}(\mathbf{q})$ and subsequently a nonzero chiral function. Inspired by the emergence of low field spin textures modulated by the characteristic wave number $k_{\mathrm{d}} = \mathcal{D}/(2A)$, we proposed phenomenological formulas for the correlation function and the resulting SANS cross section [Eqs. (5.14) and (5.15)], which can replicate the principal features of a random assembly of FeGe nanoparticles.

Chapter 6

Summary and Outlook

The objective of this doctoral thesis was to investigate the magnetic small angle neutron scattering (SANS) cross section and related correlation function of spherical magnetic nanoparticles using micromagnetic simulations. The research has focused on two key aspects:

1. Analyzing the magnetic SANS observables (mainly cross section and correlation function) in the presence of pore-type defects in spherical Fe nanoparticles [1].

2. Investigating the impact of the Dzyaloshinskii-Moriya interaction on the randomly-averaged magnetic SANS observables of spherical FeGe nanoparticles [2].

Micromagnetic simulation techniques have been used to examine how microstructural defects of the pore-type affect the observable parameters of diffuse magnetic SANS in spherical magnetic nanoparticles made of Fe. The simulations took into account various magnetic energy contributions, such as the isotropic exchange interaction, the (cubic) magnetocrystalline anisotropy, the magnetodipolar interaction, and an external magnetic field. The presence of pore-type defects gives rise to nonuniformly magnetized nanoparticles, the scattering behavior of which deviates from the superspin model. This clearly shows that assuming a homogeneous spin microstructure is insufficient for the description of magnetic SANS. Additionally, the dipolar interaction resulted in complex magnetization structures, causing anisotropic scattering patterns. Under certain conditions (low fields and particle sizes larger than about 20 nm), a vortex-type spin structure appears in the magnetic microstructure; its signature in the pair-distribution function $p(r)$ is a damped oscillatory behavior due to negative correlations.

This thesis also examined the impact of the antisymmetric Dzyaloshinkii-Moriya interaction (DMI) on the randomly-averaged diffuse magnetic SANS cross section of FeGe nanoparticles through numerical micromagnetic simulations. Different spin structures, including skyrmions, vortex and spiral types, and nearly single domains, were observed depending on the relative orientations of the magnetic anisotropy axes and the external magnetic field. The investigation focused on the spin-flip SANS cross section as well as on the associated chiral function and pair distance distribution function. A central finding is that the randomly-averaged chiral function vanishes when the DMI is not taken into account in the simulations, highlighting its essential role for understanding magnetic SANS. This result has been discussed within the context of the symmetry properties of the magnetization Fourier components and of the involved energies under space inversion. A phenomenological expression describing the correlations in FeGe at low fields has been suggested, which explains the main features found in the simulations.

In the future, the defect modeling of magnetic SANS might be improved by the adjustment of the material parameters and by the integration of the magnetoelastic interaction due to the strain field around the defects (see, e.g., Ref. [100]). Atomistic SANS simulations [122,123], although more time consuming, might also be of interest due to possibility to take the lattice structure into account. This would allow e.g. to model more complex exchange interactions, such as in iron oxide nanostructures [90]. Furthermore, future research may explore the incorporation of phenomenological models for surface anisotropy (e.g., Néel or conventional surface anisotropy [122,123]) in numerical MuMax3 simulations of magnetic SANS. The present shift from scalar functions to three-dimensional vector fields in micromagnetic SANS approaches demonstrates the continuous development in understanding the magnetic scattering behavior of magnetic nanoparticles.

REFERENCES

[1] E. Pratami Sinaga, M. P. Adams, M. Bersweiler, L. G. Vivas, E. H. Hasdeo, J. Leliaert, P. Bender, D. Honecker, and A. Michels, *Phys. Rev. B*, vol. 107, p. 014416, Jan 2023.

[2] E. P. Sinaga, M. P. Adams, E. H. Hasdeo, and A. Michels, 2024, arXiv:2402.00558 (cond-mat.mes-hall).

[3] S. Mühlbauer, D. Honecker, E. A. Périgo, F. Bergner, S. Disch, A. Heinemann, S. Erokhin, D. Berkov, C. Leighton, M. R. Eskildsen, and A. Michels, *Rev. Mod. Phys.*, vol. 91, p. 015004, Mar 2019.

[4] A. Michels, *Magnetic Small-Angle Neutron Scattering: A Probe for Mesoscale Magnetism Analysis.* Oxford: Oxford University Press, 2021.

[5] R. Pynn, *Los Alamos Science*, vol. 19, pp. 1–31, 1990.

[6] M. Bersweiler, E. Pratami Sinaga, I. Peral, N. Adachi, P. Bender, N.-J. Steinke, E. P. Gilbert, Y. Todaka, A. Michels, and Y. Oba, *Phys. Rev. Mater.*, vol. 5, p. 044409, Apr 2021.

[7] G. L. Squires, *Introduction to the Theory of Thermal Neutron Scattering.* Cambridge: Cambridge University Press, 2012.

[8] C. Kittel, *Introduction to solid state physics.* John Wiley & Sons, 2024.

[9] M. d'Aquino, "Nonlinear magnetization dynamics in thin-films and nanoparticle," Ph.D. dissertation, Università degli Studi di Napoli Federico II, 2004.

[10] L. G. Vivas, R. Yanes, D. Berkov, S. Erokhin, M. Bersweiler, D. Honecker, P. Bender, and A. Michels, *Phys. Rev. Lett.*, vol. 125, p. 117201, Sep 2020.

[11] Note that in the paper by Sinaga *et al.* [1] the coordinates of q_y and q_z have been swapped.

[12] E. A. Périgo, E. P. Gilbert, K. L. Metlov, and A. Michels, *New. J. Phys.*, vol. 16, p. 123031, 2014.

[13] M. Bersweiler, Y. Oba, E. Pratami Sinaga, I. Peral, I. Titov, M. P. Adams, V. Rai, K. L. Metlov, and A. Michels, *Phys. Rev. B*, vol. 108, p. 094434, Sep 2023.

[14] N. A. Usov and S. E. Peschany, *J. Magn. Magn. Mater.*, vol. 174, pp. 247–260, 1997.

[15] S. Mühlbauer, D. Honecker, E. A. Périgo, F. Bergner, S. Disch, A. Heinemann, S. Erokhin, D. Berkov, C. Leighton, M. R. Eskildsen, and A. Michels, *Rev. Mod. Phys.*, vol. 91, p. 015004, 2019.

[16] S. Bharathala and P. Sharma, in *Nanotechnology in Modern Animal Biotechnology*, P. K. Maurya and S. Singh, Eds. Elsevier, 2019, pp. 113–132.

[17] J. Jose, R. Kumar, S. Harilal, G. E. Mathew, D. G. T. Parambi, A. Prabhu, M. S. Uddin, L. Aleya, H. Kim, and B. Mathew, *Environmental Science and Pollution Research*, vol. 27, no. 16, pp. 19 214–19 225, Jun 2020.

[18] A. Avasthi, C. Caro, E. Pozo-Torres, M. P. Leal, and M. L. García-Martín, *Topics in Current Chemistry*, vol. 379, no. 4, p. 30, Jun 2021.

[19] B. Jiang, L. Lian, Y. Xing, N. Zhang, Y. Chen, P. Lu, and D. Zhang, *Environmental Science and Pollution Research*, vol. 25, no. 31, pp. 30 863–30 879, Nov 2018.

[20] N. S. Kumar, R. P. Suvarna, K. C. Babu Naidu, and B. V. S. Reddy, in *Fundamentals and Industrial Applications of Magnetic Nanoparticles*, ser. Woodhead Publishing Series in Electronic and Optical Materials, C. M. Hussain and K. K. Patankar, Eds. Woodhead Publishing, 2022, pp. 601–618.

[21] Q. Zhang, X. Yang, and J. Guan, *ACS Applied Nano Materials*, vol. 2, no. 8, pp. 4681–4697, Aug 2019.

[22] H. S. Hussein, *Bulletin of the National Research Centre*, vol. 47, no. 1, p. 7, Jan 2023.

[23] H. Abele, *Prog. Part. Nuc. Phys.*, vol. 60, pp. 1–81, 2008.

[24] X. Chen, P. Zhao, L. Wang, and J. Zhan, *Nanoscale Research Letters*, vol. 13, no. 1, pp. 1–10, 2018.

[25] Z. Zhou, Y. Zhang, Z. Wang, H. Chen, T. Jiang, and X. Yu, *Nanoscale Research Letters*, vol. 15, no. 1, pp. 1–21, 2020.

[26] C. Kons, K. L. Krycka, J. Robles, N. Ntallis, M. Pereiro, M.-H. Phan, H. Srikanth, J. A. Borchers, and D. A. Arena, *ACS Appl. Nano Mater.*, vol. 6, pp. 10 986–11 000, 2023.

[27] S. Disch, E. Wetterskog, R. P. Hermann, A. Wiedenmann, U. Vainio, G. Salazar-Alvarez, L. Bergström, and T. Brückel, *New J. Phys.*, vol. 14, p. 013025, 2012.

[28] K. L. Krycka, J. A. Borchers, R. A. Booth, Y. Ijiri, K. Hasz, J. J. Rhyne, and S. A. Majetich, *Phys. Rev. Lett.*, vol. 113, p. 147203, 2014.

[29] K. Hasz, Y. Ijiri, K. L. Krycka, J. A. Borchers, R. A. Booth, S. Oberdick, and S. A. Majetich, *Phys. Rev. B*, vol. 90, p. 180405(R), 2014.

[30] A. Günther, D. Honecker, J.-P. Bick, P. Szary, C. D. Dewhurst, U. Keiderling, A. V. Feoktystov, A. Tschöpe, R. Birringer, and A. Michels, *J. Appl. Cryst.*, vol. 47, pp. 992–998, 2014.

[31] T. Maurer, S. Gautrot, F. Ott, G. Chaboussant, F. Zighem, L. Cagnon, and O. Fruchart, *Phys. Rev. B*, vol. 89, p. 184423, 2014.

[32] C. L. Dennis, K. L. Krycka, J. A. Borchers, R. D. Desautels, J. van Lierop, N. F. Huls, A. J. Jackson, C. Gruettner, and R. Ivkov, *Adv. Funct. Mater.*, vol. 25, pp. 4300–4311, 2015.

[33] A. J. Grutter, K. L. Krycka, E. V. Tartakovskaya, J. A. Borchers, K. S. M. Reddy, E. Ortega, A. Ponce, and B. J. H. Stadler, *ACS Nano*, vol. 11, pp. 8311–8319, 2017.

[34] S. D. Oberdick, A. Abdelgawad, C. Moya, S. Mesbahi-Vasey, D. Kepaptsoglou, V. K. Lazarov, R. F. L. Evans, D. Meilak, E. Skoropata, J. van Lierop, I. Hunt-Isaak, H. Pan, Y. Ijiri, K. L. Krycka, J. A. Borchers, and S. A. Majetich, *Sci. Rep.*, vol. 8, p. 3425, 2018.

[35] Y. Ijiri, K. L. Krycka, I. Hunt-Isaak, H. Pan, J. Hsieh, J. A. Borchers, J. J. Rhyne, S. D. Oberdick, A. Abdelgawad, and S. A. Majetich, *Phys. Rev. B*, vol. 99, p. 094421, 2019.

[36] P. Bender, D. Honecker, and L. F. Barquín, *Appl. Phys. Lett.*, vol. 115, p. 132406, 2019.

[37] M. Bersweiler, P. Bender, L. G. Vivas, M. Albino, M. Petrecca, S. Mühlbauer, S. Erokhin, D. Berkov, C. Sangregorio, and A. Michels, *Phys. Rev. B*, vol. 100, p. 144434, 2019.

[38] D. Zákutná, D. Nižňanský, L. C. Barnsley, E. Babcock, Z. Salhi, A. Feoktystov, D. Honecker, and S. Disch, *Phys. Rev. X*, vol. 10, p. 031019, 2020.

[39] D. Honecker, M. Bersweiler, S. Erokhin, D. Berkov, K. Chesnel, D. A. Venero, A. Qdemat, S. Disch, J. K. Jochum, A. Michels, and P. Bender, *Nanoscale Adv.*, vol. 4, pp. 1026–1059, 2022.

[40] D. Honecker and A. Michels, *Phys. Rev. B*, vol. 87, p. 224426, 2013.

[41] A. Michels, S. Erokhin, D. Berkov, and N. Gorn, *J. Magn. Magn. Mater.*, vol. 350, pp. 55–68, 2014.

[42] D. Mettus and A. Michels, *J. Appl. Cryst.*, vol. 48, pp. 1437–1450, 2015.

[43] S. Erokhin, D. Berkov, and A. Michels, *Phys. Rev. B*, vol. 92, p. 014427, 2015.

[44] K. L. Metlov and A. Michels, *Phys. Rev. B*, vol. 91, p. 054404, 2015.

[45] K. L. Metlov and A.Michels, *Sci. Rep.*, vol. 6, p. 25055, 2016.

[46] A. Michels, D. Mettus, D. Honecker, and K. L. Metlov, *Phys. Rev. B*, vol. 94, p. 054424, 2016.

[47] A. Michels, D. Mettus, I. Titov, A. Malyeyev, M. Bersweiler, P. Bender, I. Peral, R. Birringer, Y. Quan, P. Hautle, J. Kohlbrecher, D. Honecker, J. R. Fernández, L. F. Barquín, and K. L. Metlov, *Phys. Rev. B*, vol. 99, p. 014416, 2019.

[48] A. A. Mistonov, I. S. Dubitskiy, I. S. Shishkin, N. A. Grigoryeva, A. Heinemann, N. A. Sapoletova, G. A. Valkovskiy, and S. V. Grigoriev, *J. Magn. Magn. Mater.*, vol. 477, pp. 99–108, 2019.

[49] V. D. Zaporozhets, Y. Oba, A. Michels, and K. L. Metlov, *Journal of Applied Crystallography*, vol. 55, no. 3, pp. 592–600, Jun 2022.

[50] I. Dzyaloshinsky, *J. Phys. Chem. Solids*, vol. 4, pp. 241–255, 1958.

[51] T. Moriya, *Phys. Rev.*, vol. 120, pp. 91–98, 1960.

[52] H.-B. Braun, *Adv. Phys.*, vol. 61, pp. 1–116, 2012.

[53] S.-W. C. Shuai Dong, Jun-Ming Liu and Z. Ren, *Adv. Phys.*, vol. 64, no. 5-6, pp. 519–626, 2015.

[54] D. Honecker, A. Ferdinand, F. Döbrich, C. D. Dewhurst, A. Wiedenmann, C. Gómez-Polo, K. Suzuki, and A. Michels, *Eur. Phys. J. B*, vol. 76, pp. 209–213, 2010.

[55] A. Michels, *J. Phys.: Condens. Matter*, vol. 26, p. 383201, 2014.

[56] S. Mühlbauer, A. Heinemann, A. Wilhelm, L. Karge, A. Ostermann, I. Defendi, A. Schreyer, W. Petry, and R. Gilles, *Nucl. Instrum. Methods Phys. Res. A*, vol. 832, pp. 297–305, 2016.

[57] H. Schober, *J. Neutron Res.*, vol. 17, pp. 109–357, 2014.

[58] S. W. Lovesey, *Theory of Neutron Scattering from Condensed Matter.* Oxford: Clarendon Press, 1984, vol. I and II.

[59] D. Sivia, *Elementary Scattering Theory: For X-ray and Neutron Users.* Oxford University Press, 01 2011.

[60] H. Kronmüller and M. Fähnle, *Micromagnetism and the Microstructure of Ferromagnetic Solids.* Cambridge: Cambridge University Press, 2003.

[61] J. Schweizer, “Polarized Neutrons and Polarization Analysis,” in *Neutron Scattering from Magnetic Materials*, T. Chatterji, Ed. Amsterdam: Elsevier, 2006, pp. 153–213.

[62] M. P. Adams, A. Michels, and H. Kachkachi, *Journal of Applied Crystallography*, vol. 55, no. 6, pp. 1475–1487, Dec 2022.

[63] A. Guinier, *X-Ray Diffraction in Crystals, Imperfect Crystals, and Amorphous Bodies.* New York: Dover Publications, 1994.

[64] G. Porod, "General Theory," in *Small Angle X-ray Scattering*, O. Glatter and O. Kratky, Eds. London: Academic Press, 1982, pp. 17–51.

[65] O. Glatter, "Interpretation," in *Small Angle X-ray Scattering*, O. Glatter and O. Kratky, Eds. London: Academic Press, 1982, pp. 167–196.

[66] D. I. Svergun and M. H. J. Koch, *Rep. Prog. Phys.*, vol. 66, pp. 1735–1782, 2003.

[67] A. Aharoni, *Introduction to the Theory of Ferromagnetism*, 2nd ed. Oxford: Oxford University Press, 2000.

[68] A. Vansteenkiste, J. Leliaert, M. Dvornik, M. Helsen, F. Garcia-Sanchez, and B. Van Waeyenberge, *AIP Advances*, vol. 4, p. 107133, 2014.

[69] J. Leliaert, M. Dvornik, J. Mulkers, J. De Clercq, M. V. Milošević, and B. Van Waeyenberge, *J. Phys. D: Appl. Phys.*, vol. 51, p. 123002, 2018.

[70] L. Landau and E. Lifshitz, *Phys. Z. Sowjetunion*, vol. 8, pp. 153–169, 1935.

[71] L. Lopez-Diaz, D. Aurelio, L. Torres, E. Martinez, M. A. Hernandez-Lopez, J. Gomez, O. Alejos, M. Carpentieri, G. Finocchio, and G. Consolo, *J. Phys. D: Appl. Phys.*, vol. 45, p. 323001, 2012.

[72] W. F. Brown Jr., *Micromagnetics.* New York: Interscience Publishers, 1963.

[73] A. N. Bogdanov, U. K. Rössler, and C. Pfleiderer, *Physica B*, vol. 359-361, pp. 1162–1164, 2005.

[74] S. V. Maleyev, *Phys. Rev. B*, vol. 73, p. 174402, 2006.

[75] A. N. Bogdanov and D. A. Yablonskiĭ, *Sov. Phys. JETP*, vol. 68, pp. 101–103, 1989.

[76] A. Bogdanov and A. Hubert, *J. Magn. Magn. Mater.*, vol. 138, pp. 255–269, 1994.

[77] A. N. Bogdanov and U. K. RökJ.kg^{-1}K^{-1}ler, *Phys. Rev. Lett.*, vol. 87, p. 037203, 2001.

[78] Y. Yamasaki, H. Sagayama, T. Goto, M. Matsuura, K. Hirota, T. Arima, and Y. Tokura, *Phys. Rev. Lett.*, vol. 98, p. 147204, 2007.

[79] N. Kanazawa, J.-H. Kim, D. S. Inosov, J. S. White, N. Egetenmeyer, J. L. Gavilano, S. Ishiwata, Y. Onose, T. Arima, B. Keimer, and Y. Tokura, *Phys. Rev. B*, vol. 86, p. 134425, 2012.

[80] H. Wilhelm, M. Baenitz, M. Schmidt, C. Naylor, R. Lortz, U. K. RökJ.kg^{-1}K^{-1}ler, A. A. Leonov, and A. N. Bogdanov, *J. Phys.: Condens. Matter*, vol. 24, p. 294204, 2012.

[81] S. Rohart and A. Thiaville, *Phys. Rev. B*, vol. 88, p. 184422, 2013.

[82] F. N. Rybakov, A. B. Borisov, S. Blügel, and N. S. Kiselev, *Phys. Rev. Lett.*, vol. 115, p. 117201, 2015.

[83] J. S. White, A. Butykai, R. Cubitt, D. Honecker, C. D. Dewhurst, L. F. Kiss, V. Tsurkan, and S. Bordács, *Phys. Rev. B*, vol. 97, p. 020401(R), 2018.

[84] J. Kindervater, I. Stasinopoulos, A. Bauer, F. X. Haslbeck, F. Rucker, A. Chacon, S. Mühlbauer, C. Franz, M. Garst, D. Grundler, and C. Pfleiderer, *Phys. Rev. X*, vol. 9, p. 041059, 2019.

[85] E. Jellyman, P. Jefferies, S. Pollard, E. M. Forgan, E. Blackburn, E. Campillo, A. T. Holmes, R. Cubitt, J. Gavilano, H. Wang, J. Du, and M. Fang, *Phys. Rev. B*, vol. 101, p. 134523, 2020.

[86] S. Mühlbauer, B. Binz, F. Jonietz, C. Pfleiderer, A. Rosch, A. Neubauer, R. Georgii, and P. Böni, “Skyrmion lattice in a chiral magnet,” *Science*, vol. 323, no. 5916, pp. 915–919, 2009.

[87] J. D. Jackson, *Klassische Elektrodynamik*, 2nd ed. Berlin: Walter de Gruyter, 1983.

[88] D. A. Garanin and H. Kachkachi, *Phys. Rev. Lett.*, vol. 90, p. 065504, 2003.

[89] Z. Nedelkoski, D. Kepaptsoglou, L. Lari, T. Wen, R. A. Booth, S. D. Oberdick, P. L. Galindo, Q. M. Ramasse, R. F. L. Evans, S. Majetich, and V. K. Lazarov, *Sci. Rep.*, vol. 7, p. 45997, 2017.

[90] A. Lappas, G. Antonaropoulos, K. Brintakis, M. Vasilakaki, K. N. Trohidou, V. Iannotti, G. Ausanio, A. Kostopoulou, M. Abeykoon, I. K. Robinson, and E. S. Bozin, *Phys. Rev. X*, vol. 9, p. 041044, 2019.

[91] A. Lak, S. Disch, and P. Bender, *Adv. Sci.*, vol. 8, p. 2002682, 2021.

[92] S. Erokhin, D. Berkov, N. Gorn, and A. Michels, *Phys. Rev. B*, vol. 85, p. 024410, 2012.

[93] S. A. Pathak and R. Hertel, *Phys. Rev. B*, vol. 103, p. 104414, 2021.

[94] T. Köhler, A. Feoktystov, O. Petracic, N. Nandakumaran, A. Cervellino, and T. Brückel, *J. Appl. Cryst.*, vol. 54, pp. 1719–1729, 2021.

[95] S. Ciccariello, J. Goodisman, and H. Brumberger, *J. Appl. Cryst.*, vol. 21, pp. 117–128, 1988.

[96] C. E. Krill and R. Birringer, *Philos. Mag. A*, vol. 77, pp. 621–640, 1998.

[97] K. L. Metlov and A. Michels, *Scientific Reports*, vol. 6, no. 1, p. 25055, Apr 2016.

[98] I. Mirebeau, N. Martin, M. Deutsch, L. J. Bannenberg, C. Pappas, G. Chaboussant, R. Cubitt, C. Decorse, and A. O. Leonov, *Phys. Rev. B*, vol. 98, p. 014420, Jul 2018.

[99] J. Leliaert, B. Van de Wiele, A. Vansteenkiste, L. Laurson, G. Durin, L. Dupré, and B. Van Waeyenberge, *J. Appl. Phys.*, vol. 115, p. 17D102, 2014.

[100] F. Vanderveken, J. Mulkers, J. Leliaert, B. Van Waeyenberge, B. Sorée, O. Zografos, F. Ciubotaru, and C. Adelmann, *Open Research Europe*, vol. 1, no. 35, 2021.

[101] A. Arrott, *J. Appl. Phys.*, vol. 34, pp. 1108–1109, 1963.

[102] A. Fert and P. M. Levy, *Phys. Rev. Lett.*, vol. 44, pp. 1538–1541, 1980.

[103] V. I. Fedorov, A. G. Gukasov, V. Kozlov, S. V. Maleyev, V. P. Plakhty, and I. A. Zobkalo, *Phys. Lett. A*, vol. 224, pp. 372–378, 1997.

[104] S. V. Grigoriev, Y. O. Chetverikov, D. Lott, and A. Schreyer, *Phys. Rev. Lett.*, vol. 100, p. 197203, 2008.

[105] P. Beck and M. Fähnle, *J. Magn. Magn. Mater.*, vol. 322, pp. 3701–3703, 2010.

[106] A. B. Butenko and U. K. RökJ.kg^{-1}K^{-1}ler, *EPJ Web of Conferences*, vol. 40, p. 08006, 2013.

[107] D. A. Kitchaev, I. J. Beyerlein, and A. Van der Ven, *Phys. Rev. B*, vol. 98, p. 214414, 2018.

[108] D.-H. Kim, M. Haruta, H.-W. Ko, G. Go, H.-J. Park, T. Nishimura, D.-Y. Kim, T. Okuno, Y. Hirata, Y. Futakawa, H. Yoshikawa, W. Ham, S. Kim, H. Kurata, A. Tsukamoto, Y. Shiota, T. Moriyama, S.-B. Choe, K.-J. Lee, and T. Ono, *Nat. Mater.*, vol. 18, pp. 685–690, 2019.

[109] S. Mühlbauer, B. Binz, F. Jonietz, C. Pfleiderer, A. Rosch, A. Neubauer, R. Georgii, and P. Böni, *Science*, vol. 323, pp. 915–919, 2009.

[110] A. Bauer and C. Pfleiderer, in *Topological Structures in Ferroic Materials*, J. Seidel, Ed. Cham: Springer International Publishing, 2010, pp. 1–28.

[111] N. Nagaosa and Y. Tokura, *Nat. Nanotech.*, vol. 8, pp. 899–911, 2013.

[112] R. Wiesendanger, *Nat. Rev. Mater.*, vol. 1, p. 16044, 2016.

[113] C. Back, V. Cros, H. Ebert, K. Everschor-Sitte, A. Fert, M. Garst, T. Ma, S. Mankovsky, T. L. Monchesky, M. Mostovoy, N. Nagaosa, S. S. P. Parkin, C. Pfleiderer, N. Reyren, A. Rosch, Y. Taguchi, Y. Tokura, K. von Bergmann, and J. Zang, *J. Phys. D: Appl. Phys.*, vol. 53, p. 363001, 2020.

[114] A. N. Bogdanov and C. Panagopoulos, *Nat. Rev. Phys.*, vol. 2, pp. 492–498, 2020.

[115] R. Takagi, D. Morikawa, K. Karube, N. Kanazawa, K. Shibata, G. Tatara, Y. Tokunaga, T. Arima, Y. Taguchi, Y. Tokura, and S. Seki, *Phys. Rev. B*, vol. 95, p. 220406, 2017.

[116] H. Kronmüller and S. Parkin, *Handbook of Magnetism and Advanced Magnetic Materials.* Chichester: Wiley, 2007, volume 2.

[117] J. D. Jackson, *Classical Electrodynamics*, 3rd ed. Hoboken: Wiley, 1999.

[118] J.-V. Kim and J. Mulkers, *IOP SciNotes*, vol. 1, p. 025211, 2020.

[119] V. Ukleev, F. Ajejas, A. Devishvili, A. Vorobiev, N.-J. Steinke, R. Cubitt, C. Luo, R.-M. Abrudan, F. Radu, V. Cros, N. Reyren, and J. S. White, *STAM Methods*, vol. 25, p. 2315015, 2024.

[120] S. V. Maleev, *Physics–Uspekhi*, vol. 45, pp. 569–596, 2002.

[121] S. Erokhin, D. Berkov, and A. Michels, *New. J. Phys.*, vol. 25, p. 083018, 2023.

[122] M. P. Adams, A. Michels, and H. Kachkachi, *Journal of Applied Crystallography*, vol. 55, no. 6, pp. 1488–1499, Dec 2022.

[123] M. P. Adams, E. P. Sinaga, H. Kachkachi, and A. Michels, *Phys. Rev. B*, vol. 109, p. 024429, 2024.

[124] D. Cortés-Ortuño, M. Beg, V. Nehruji, L. Breth, R. Pepper, T. Kluyver, G. Downing, T. Hesjedal, P. Hatton, T. Lancaster, R. Hertel, O. Hovorka, and H. Fangohr, *New. J. Phys.*, vol. 20, no. 11, p. 113015, nov 2018.

Appendix A

SANS results for $d\Sigma_{\mathrm{sf}}/d\Omega$ and $iK\chi$ with and without the Dzyaloshinskii-Moriya Interaction

In this Appendix, we display additional results (Figs. A.1–A.3) for the randomly-averaged spin-flip SANS cross section $d\Sigma_{\mathrm{sf}}/d\Omega$ and the chiral function $iK\chi$ of FeGe nanoparticles [2]. All the magnetic interactions (Zeeman, isotropic exchange, anisotropy, and dipolar energy) were taken into account, and we compare results with and without the DMI energy. By varying the particle diameter and the applied magnetic field ($60\,\mathrm{nm} \leq D \leq 200\,\mathrm{nm}$ and $-1\,\mathrm{T} \leq \mu_0 H_0 \leq 1\,\mathrm{T}$), we find that the chiral function vanishes in the case when the DMI is absent, while including the DMI gives rise to complex scattering patterns.

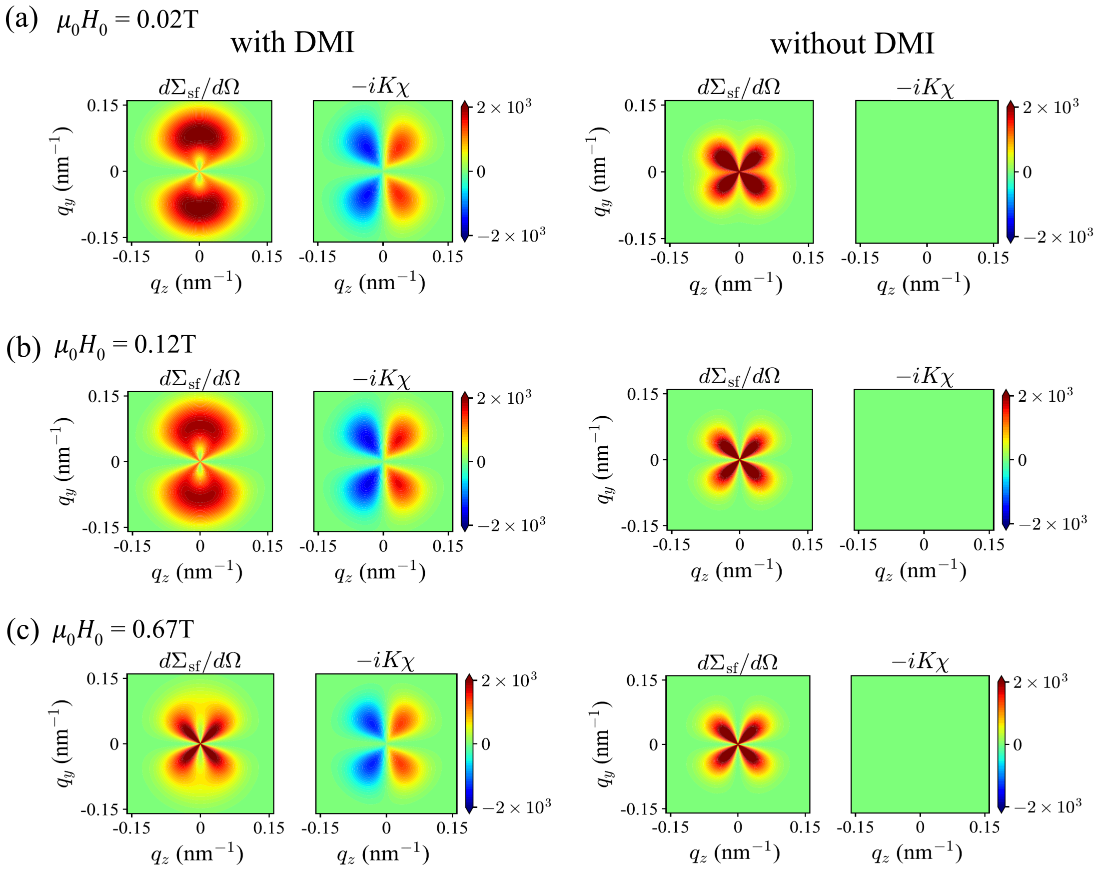

Figure A.1: Micromagnetic simulation results for the randomly-averaged spin-flip SANS cross section $d\Sigma_{\mathrm{sf}}/d\Omega$ and the chiral function $iK\chi$ of FeGe nanoparticles with a diameter of $D = 60$ nm. Results are shown for three different applied magnetic fields: (a) $\mu_0 H_0 = 0.02$ T, (b) $\mu_0 H_0 = 0.12$ T, and (c) $\mu_0 H_0 = 0.67$ T. The left panel displays the simulation results with the Dzyaloshinskii-Moriya interaction (DMI), while the data in the right panel do not include the DMI. Image taken from [2].

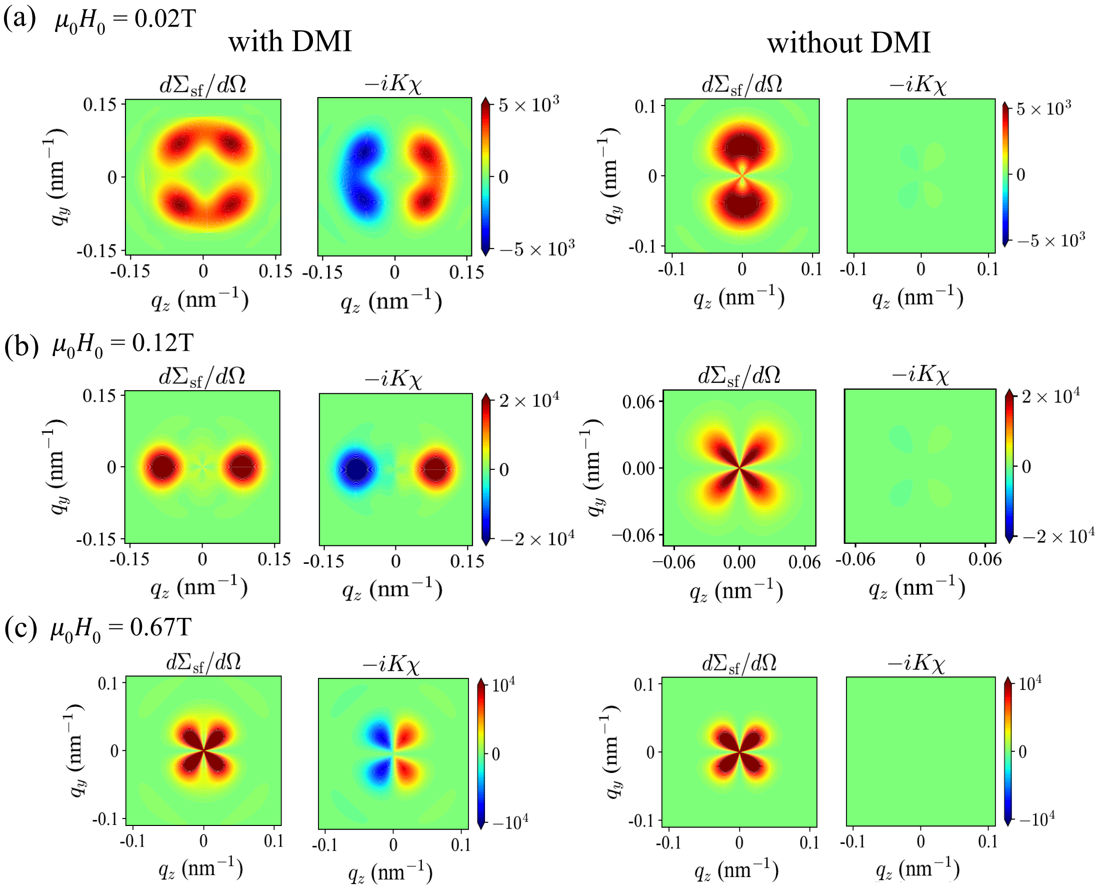

Figure A.2: Similar to figure A.1, but for $D = 120\,\text{nm}$. Image taken from [2].

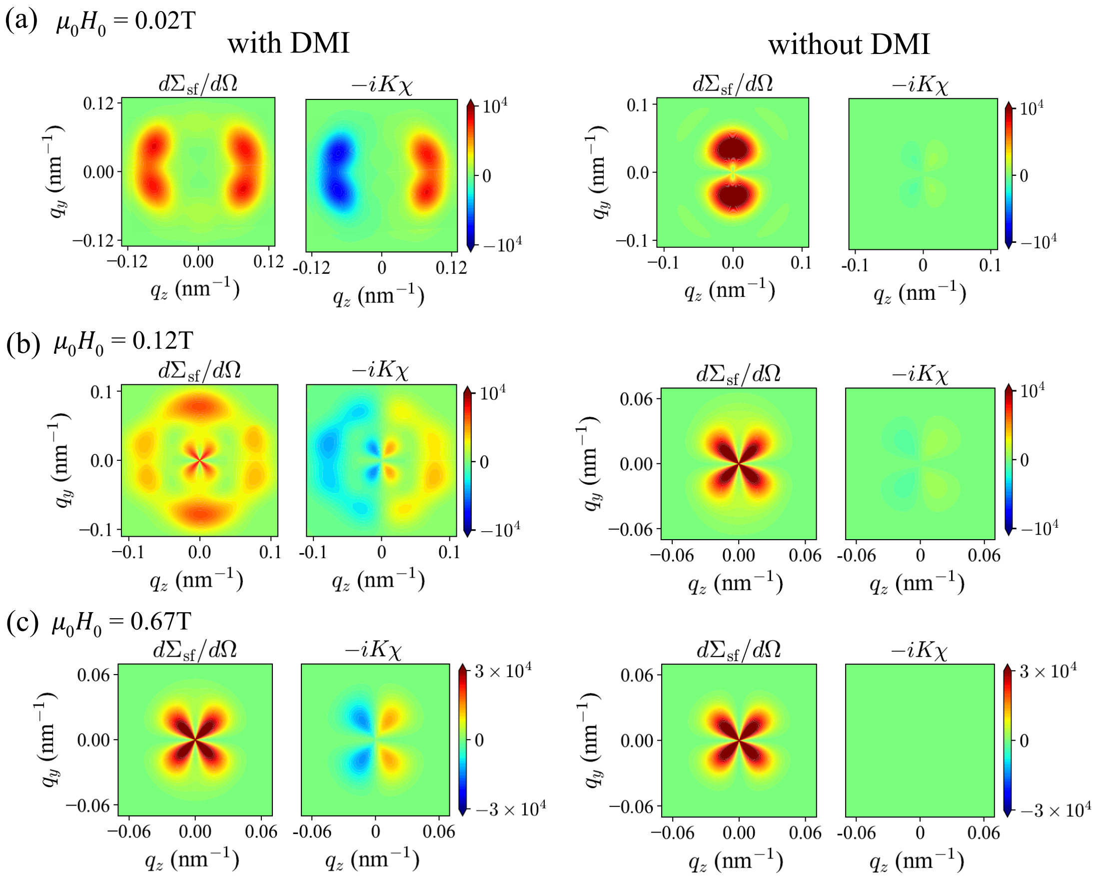

Figure A.3: Similar to figure A.1, but for $D = 150$ nm. Image taken from [2].

Appendix B

Single Skyrmion in a Cylindrical FeGe Disk

In this Appendix, we present the results for the magnetization distribution in a single cylindrical FeGe disk. This research was undertaken in order to replicate the numerical results for the micromagnetic standard problem of materials with DMI proposed in Ref. [124]. They serve as a benchmark for the SANS simulations on the FeGe spheres in Chapter 5.

The simulations were performed on a circular FeGe platelet with a constant height of 20 nm and a diameter ranging between 60 nm and 200 nm [124]. The volume of the nanodot was discretized into $1 \times 1 \times 1\,\mathrm{nm}$ cells; for a nanodot with a height of 20 nm and a diameter of 100 nm, this leads to approximately 157000 cells. We have taken into account the following contributions to the total magnetic Gibbs free energy: Zeeman energy E_{z} in the external magnetic field $\mathbf{H}_0$, isotropic and symmetric exchange energy E_{ex}, as well as the antisymmetric DMI energy E_{dmi}. For simplicity, we have ignored the magnetic anisotropy energy and the magnetodipolar interaction, which can also be taken into account. Periodic boundary conditions in the x and y directions were employed and the following materials parameters for FeGe were used [93]: $M_{\mathrm{s}} = 384\,\mathrm{kA/m}$, $A = 8.78 \times 10^{-12}\,\mathrm{J/m}$, and $\mathcal{D} = 1.58 \times 10^{-3}\,\mathrm{J/m^2}$.

Figure B.1 displays the computed spin structures of FeGe nanodisks with diameters of 60 nm and 200 nm at an applied magnetic field of 40 mT. It becomes visible that, while m_z is an even function of the position (along the x direction), both transversal magnetization components m_x and m_y are uneven functions of the position within the considered middle layer extending from 9–11 nm. This is a consequence of the DMI, which breaks structural inversion symmetry, and is

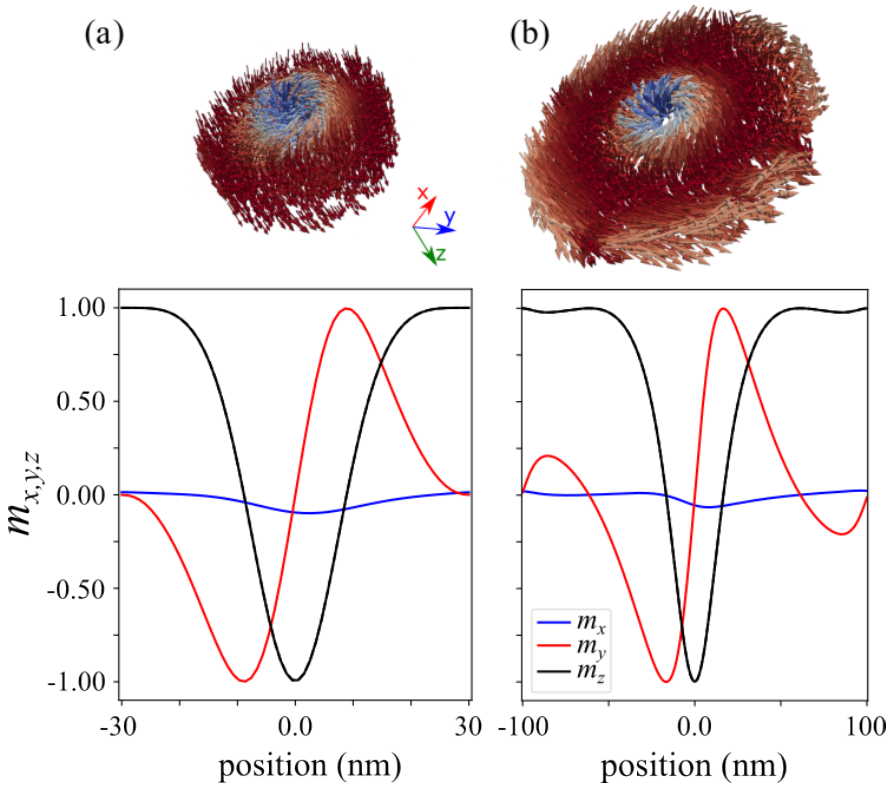

Figure B.1: Skyrmion spin structures in circular FeGe nanodots with diameters of (a) 60 nm and (b) 200 nm (respective height is 20 nm). $\mathbf{H}_0 \parallel \mathbf{e}_z$ with $\mu_0 H_0 = 40\,\mathrm{mT}$. Below the 3D spin structures we display, for the respective middle layer (extending from 9–11 nm), the spatial profile of the Cartesian components of $\mathbf{m}$ along the x direction (see inset). The winding number of these spin structures (middle layer), computed as $Q = (4\pi)^{-1} \int d^2\mathbf{r}\, \mathbf{m} \cdot (\partial\mathbf{m}/\partial x \times \partial\mathbf{m}/\partial y)$, evaluates to $Q \cong -1$.

expected to result in a nonzero chiral function contained in the spin-flip channels. All in all we can say that the results agree very well with the ones reported in Ref. [124].

Appendix C

Numerical Fourier Transformation

The magnetic small angle neutron scattering cross section depends on the Fourier components $\widetilde{M}_{x,y,x}(\mathbf{q})$ of the magnetization $\mathbf{M}(\mathbf{r})$. The continuous magnetization vector field is introduced as the local thermodynamical average over N discrete atomic magnetic moments $\boldsymbol{\mu}_a$ within a small mesoscopic volume V.

$$\mathbf{M} = \mathbf{M}(\mathbf{r}) = \left\{ \begin{matrix} M_x(x,y,z) \\ M_y(x,y,z) \\ M_z(x,y,z) \end{matrix} \right\} \hat{=} V^{-1} \sum_{i=1}^{N} \boldsymbol{\mu}_{a,i} \tag{C.1}$$

The magnitude of $\mathbf{M}$ is denoted as the saturation magnetization M_s, which is only a function of temperature. The three-dimensional Fourier-transform pair of the magnetization can then be defined as:

$$\mathbf{M}(\mathbf{r}) = \frac{1}{(2\pi)^{3/2}} \int \widetilde{\mathbf{M}}(\mathbf{q}) \exp\left(i\mathbf{q}\cdot\mathbf{r}\right)\, d^3q, \tag{C.2}$$

$$\widetilde{\mathbf{M}}(\mathbf{q}) = \frac{1}{(2\pi)^{3/2}} \int_V \mathbf{M}(\mathbf{r}) \exp\left(-i\mathbf{q}\cdot\mathbf{r}\right)\, d^3r. \tag{C.3}$$

where $i^2 = -1$, $\mathbf{q} = \{q_x, q_y, q_z\}$ is the wave vector, and $\mathbf{r} = \{x, y, z\}$ is the position vector. Note that the Fourier components $\widetilde{M}_{x,y,x}$ are in units of Am^2, while the real-space magnetization components $M_{x,y,x}$ come in units of A/m.

When dealing with numerical micromagnetic spin structure data, it is necessary to compute the discrete Fourier transform of all the unit magnetization vectors $\mathbf{m}_i = \mathbf{m}_i(\mathbf{r}) = \mathbf{M}_i/M_\mathrm{s}$ belonging to the spherical nanomagnet. In fact, one needs to consider the following discrete version of the above continuous Fourier integral:

$$\widetilde{\mathbf{M}}(\mathbf{q}) \cong \frac{1}{(2\pi)^{3/2}} \sum_{i=1}^{\mathcal{K}} \boldsymbol{\mu}_i \exp\left(-i\mathbf{q}\cdot\mathbf{r}_i\right), \tag{C.4}$$

where $\boldsymbol{\mu}_i$ is the magnetic moment (in Am^2) of the discretization cell "i" (with a typical size of $a = 2\,\mathrm{nm}$), $\mathbf{r}_i = \{x_i, y_i, z_i\}$ is the location point of the cell, $\mathbf{q}$ represents the wave vector (scattering vector), and $\mathcal{K}$ represents the number of cells; see Fig. 4.3 for a sketch that illustrates the discretization of a spherical nanoparticle into cubical cells.

In the micromagnetic simulations we have set $q_x = 0$, which corresponds to the perpendicular scattering geometry where the applied magnetic field $\mathbf{H}_0$ is perpendicular to the incident neutron beam (compare Fig. 2.2). In this case $[\mathbf{q} \cong \{0, q_y, q_z\}]$, we have typically used $10^3 \times 10^3$ points for the computation of a two-dimensional (q_y-q_z) detector image. Moreover, using $\boldsymbol{\mu}_i = \boldsymbol{\mu}_i(\mathbf{r}) = M_\mathrm{s} V_i \mathbf{m}_i(\mathbf{r})$, the discrete-space Fourier transform [Eq. (C.4)] is computed as ($V_i = a^3$)

$$\widetilde{\mathbf{M}}(\mathbf{q}) \cong \frac{M_\mathrm{s} a^3 h(\mathbf{q})}{(2\pi)^{3/2}} \sum_{i=1}^{\mathcal{K}} \mathbf{m}_i \exp\left(-i\mathbf{q}\cdot\mathbf{r}_i\right). \tag{C.5}$$

We use the CUDA C++ environment, which does not support complex numbers. Therefore, we split the above sum into the real (Re) and imaginary (Im) parts as follows:

$$\mathrm{Re}\{\widetilde{\mathbf{M}}(\mathbf{q})\} = \frac{M_\mathrm{s} a^3 h(\mathbf{q})}{(2\pi)^{3/2}} \sum_{i=1}^{\mathcal{K}} \mathbf{m}_i \cos\left(\mathbf{q}\cdot\mathbf{r}_i\right) \tag{C.6}$$

$$\mathrm{Im}\{\widetilde{\mathbf{M}}(\mathbf{q})\} = \frac{M_\mathrm{s} a^3 h(\mathbf{q})}{(2\pi)^{3/2}} \sum_{i=1}^{\mathcal{K}} \mathbf{m}_i \sin\left(\mathbf{q}\cdot\mathbf{r}_i\right) \tag{C.7}$$

Using Eqs. (C.6) and (C.7), we can evaluate $\widetilde{\mathbf{M}}(\mathbf{q})$ for arbitrary resolution of $\mathbf{q}$. The function

$$h(\mathbf{q}) = h(q_y, q_z) = \frac{\sin(q_y a/2)}{q_y a/2} \frac{\sin(q_z a/2)}{q_z a/2} \tag{C.8}$$

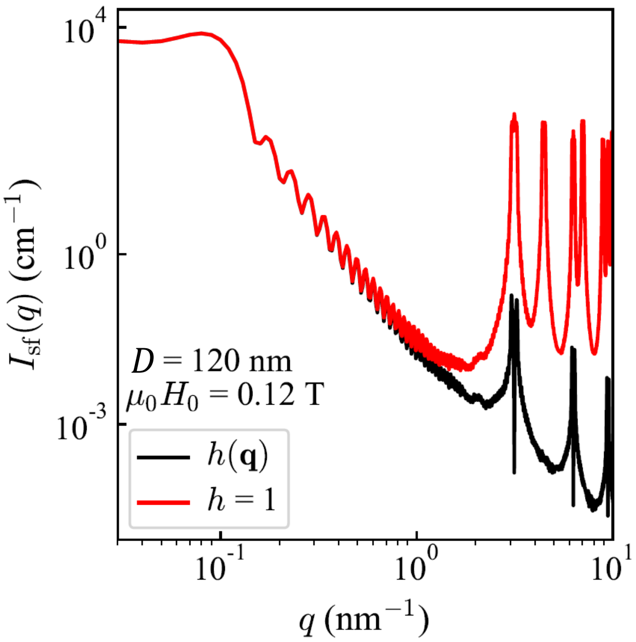

Figure C.1: Effect of the form factor of the cubic discretization cell, $h(\mathbf{q})$, on the randomly-averaged spin-flip SANS cross section $I_{\mathrm{sf}}(q)$ [compare Eq. (C.4)]. Shown is $I_{\mathrm{sf}}(q)$ for $D = 120\,\mathrm{nm}$ and at $\mu_0 H_0 = 0.12\,\mathrm{T}$ with the function $h(q_x = 0, q_y, q_z) = \frac{\sin(q_y a/2)}{q_y a/2} \frac{\sin(q_z a/2)}{q_z a/2}$ included using a cell size of $a = 2\,\mathrm{nm}$ (black line) and for $h = 1$ (red line) (log-log scale). As is seen, the q dependent cell form factor suppresses the scattering curve. Here, significant deviations become noticeable for $q \gtrsim 0.3\,\mathrm{nm}^{-1}$. Figure taken from [2].

denotes the form factor of the cubic discretization cell with $a = 2\,\mathrm{nm}$ being the cell size; for $q_{y,z}a/2 \ll 1$, $h \rightarrow 1$. For atomistic calculations [122, 123], this correction is irrelevant in the small-angle regime, but for the here-used cell size becomes already noticeable for $q \gtrsim 0.3\,\mathrm{nm}^{-1}$ illustrated in Fig. C.1. Equation (C.5) establishes the relation between the outcome of the simulations, $\mathbf{m}_i$, and the SANS observables computed in this PhD thesis.

Appendix D

Magnetic SANS Cross Section in the Presence of a Lognormal Distribution Function

In this Appendix, we provide additional details on the incorporation of a lognormal particle-size distribution function into the micromagnetic simulations of Section 4.4. For the purpose of comparison to analytical expressions, we restrict ourselves to the saturated case, but the general principle is applicable to any azimuthally-averaged SANS cross section.

The unpolarized magnetic SANS cross section for the perpendicular scattering geometry can be expressed as ($\mathbf{k}_0 \perp \mathbf{H}_0$):

$$\begin{aligned} \frac{d\Sigma_{\mathrm{M}}}{d\Omega} &= \frac{8\pi^3}{V} b_{\mathrm{H}}^2 \Big(|\widetilde{M}_x|^2 + |\widetilde{M}_y|^2 \cos^2\theta \\ &+ |\widetilde{M}_z|^2 \sin^2\theta - (\widetilde{M}_y \widetilde{M}_z^* + \widetilde{M}_y^* \widetilde{M}_z) \sin\theta\cos\theta \Big) . \end{aligned} \tag{D.1}$$

In the case of magnetic saturation ($M_x = M_y = 0$) and for a single spherical particle with diameter $D = 2R$, this expression simplifies to:

$$\frac{d\Sigma_{\mathrm{M}}}{d\Omega} = 9 V_{\mathrm{p}} (\Delta\rho)_{\mathrm{mag}}^2 \left(\frac{j_1(qD/2)}{qD/2} \right)^2 \sin^2\theta, \tag{D.2}$$

where $V_{\mathrm{p}} = 4/3\pi(D/2)^3$ is the sphere volume, $(\Delta\rho)_{\mathrm{mag}}^2 = b_{\mathrm{H}}^2 M_{\mathrm{s}}^2$ is the magnetic scattering length density contrast, and $j_i(z)$ denotes the spherical Bessel function of the first order. Azimuthally-averaging Eq. (D.2) produces a factor of 1/2 (due to the $\sin^2\theta$ factor). The lognormal distribution function can be defined as follows [96]:

$$f(D) = \frac{1}{\sqrt{2\pi} D \log\sigma} e^{-\frac{1}{2}\left(\frac{\log D - \log D_0}{\log\sigma}\right)^2}, \tag{D.3}$$

where D_0 is the median of the distribution and the parameter σ describes its width ($\int_0^\infty f(D) dD = 1$). The magnetic SANS cross section averaged over the distribution, $\langle d\Sigma_{\mathrm{M}}/d\Omega \rangle_f$, is then computed as follows:

$$\left\langle \frac{d\Sigma_{\mathrm{M}}}{d\Omega}(q) \right\rangle_f = \int_0^\infty \frac{d\Sigma_{\mathrm{M}}}{d\Omega}(q, D) f(D) dD. \tag{D.4}$$

Note that in the actual micromagnetic simulations we have typically chosen $D_{\mathrm{min}} = 10\,\mathrm{nm}$ and $D_{\mathrm{max}} = 100\,\mathrm{nm}$ as the limits of the above integral (see Section 4.4). The corresponding pair distance distribution function averaged over the distribution, $\langle p(r) \rangle_f$, can then be computed from the azimuthally-averaged magnetic SANS cross section according to:

$$\langle p(r) \rangle_f = r^2 \int_0^\infty \left\langle \frac{d\Sigma_{\mathrm{M}}}{d\Omega}(q) \right\rangle_f j_0(qr) q^2 dq, \tag{D.5}$$

where $j_0(x) = \sin x/x$. For comparison, the $p(r)$ [$c(r)$] of a single spherical particle with radius R reads (for $r \leq 2R$) [Eq. (2.33)] [66]:

$$\begin{aligned} p(r) &= r^2 c(r), \qquad \text{(D.6)} \\ p(r) &= r^2 \left(1 - \frac{3r}{4R} + \frac{r^3}{16R^3}\right), \end{aligned}$$

while $p(r) = 0$ for $r > 2R$. Figure D.1 displays the effect of a particle-size distribution on the single-particle magnetic SANS cross section at saturation and on the corresponding pair distance distribution. One can see that with increasing width σ of $f(D)$ the features in $\left\langle \frac{d\Sigma_{\mathrm{M}}}{d\Omega}(q) \right\rangle_f$ and $\langle p(r) \rangle_f$ are progressively washed out; the zero in the single-particle $p(r)$ at $r = 2R = 40\,\mathrm{nm}$ shifts to larger distances with increasing σ. The case of a saturated spherical particle has merely been chosen for illustration purposes and because we can compare the results for the averaged quantities $\langle d\Sigma_{\mathrm{M}}/d\Omega\rangle_f$ and $\langle p\rangle_f$ with the analytically-known single particle results [Eqs. (D.2) and (D.6)].

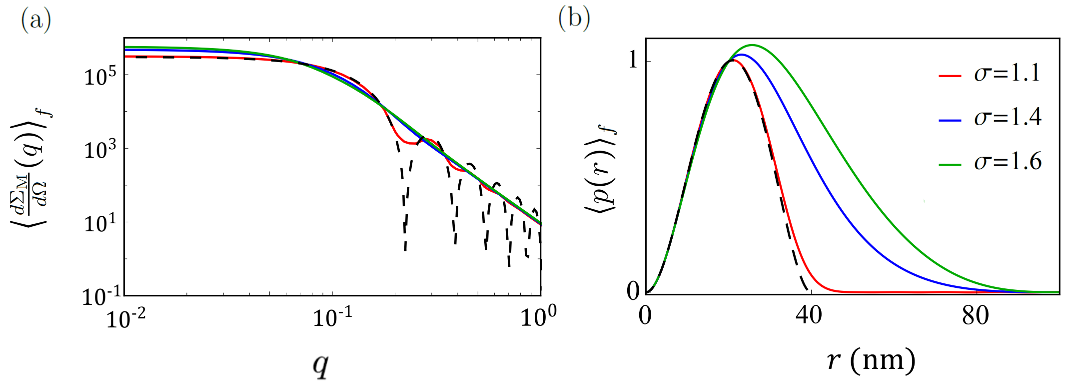

Figure D.1: Effect of a lognormal particle-size distribution function on the single-particle magnetic SANS cross section at saturation and the corresponding pair distance distribution. Shown are (a) $\left\langle \frac{d\Sigma_{\mathrm{M}}}{d\Omega}(q) \right\rangle_f$ (log-log scale) and (b) $\langle p(r) \rangle_f$ for different values of the width σ of the distribution. The black dashed lines in (a) and (b) correspond, respectively, to a single sphere with a diameter of $D = 2R = 40$ nm.

Appendix E

MuMax3 Codes

In this Appendix, we provide the main parts of the MuMax3 codes used for the miromagnetic SANS simulations.

E.1 Effect of Defects in Fe Nanospheres [1]

```
ngrid := 64
xcell := 2e−9
defects := 0.15
d := 40e−9
r := d/2

SetGridsize(ngrid, ngrid, ngrid)
SetCellsize(xcell, xcell, xcell)
a := ellipsoid(d, d, d)
rgrid := r/xcell
vgrid := 4.0/3.0∗Pi∗(rgrid∗rgrid∗rgrid)
vdef := vgrid ∗ defects
print(”vdef =”,vdef)
maxregion := 200
kali := pow(vdef/maxregion,1/3)
print (vgrid, vdef,kali,r,xcell)
SetGeom(a)
DefRegion(1,a)

Msat.SetRegion(1, 1.7e6 )
Aex.SetRegion(1, 1e−11)
Kc1.SetRegion(1, 4.7e4)
```

```
Kc2.SetRegion(1, -0.01e6)
radiusR := 40e-9
setgeom(ellipsoid(radiusR, radiusR, radiusR))
alpha = 1
randomSeed := CAMBIO
randSeed(randomSeed)

Bmax  := 1.0
Bstep :=  0.5e-2
TableAdd(B_ext)

for j:=0; j<maxParticleNumber; j++{
// random cubic anisotropy direction
    theta := 2.0*pi*rand()
    phi := acos(1.0-2.0*rand())
    axis1  := vector(sin(phi)*cos(theta),sin(phi)*sin(theta), cos(phi))
    theta2 := 2.0*pi*rand()
    phi2 := acos(1.0-2.0*rand())
    helper  := vector(sin(phi2)*cos(theta2),sin(phi2)*sin(theta2), cos(phi2))
    axis2 := axis1.cross(helper)
    AnisC1 = axis1     // axes need not be normalized
    AnisC2 = axis2
// Save the direction of the easy axes
 fprintln("Parti-Eaxes.txt", j, AnisC1, AnisC2)

// set random parameters per region
for i:=2; i<maxRegion; i++{
    x1:=(r * rand())*Sin(Pi*rand())*Cos(2*Pi*rand())
    y1:=(r * rand())*Sin(Pi*rand())*Sin(2*Pi*rand())
    z1:=(r * rand())*Cos(Pi*rand())
    //print(x1,y1,z1)
    DefRegion(i,cuboid (xcell*kali, xcell*kali, xcell*kali). transl (x1,y1,z1))
    Msat.SetRegion(i, 0.0) \\defects properties
    Aex.SetRegion(i, 0.0)
    Ku1.SetRegion(i, 0.0)
```

```
    Ku2.SetRegion(i, 0.0)
    alpha.SetRegion(i, 0.0)}

// Initial magnetization
   m=uniform(1.0,0.0,0.0)


i:=0
iB:= 0
// hysteresis loops:
    for B:=Bmax; B>=-Bmax; B-=Bstep{
            i = i+1
            iB = floor(B*100)
            B_ext = vector(B, 0.0, 0.0)
                relax()
            tablesave()
           // FilenameFormat=sprintf(”%%s%%03d%%03d”,iB)
           // save (mfft_squared)
          // save (mfft_imaginary)
          // save (mfft_real)
           FilenameFormat=sprintf(”%%s%%06d”)
           save (m)}

for B:=-Bmax; B<=Bmax; B+=Bstep{
             i = i+1
             iB = floor(B*100)
                B_ext = vector(B, 0.0, 0.0)
                    relax()
           tablesave()}
```

E.2 Effect of DMI in FeGe Nanospheres [2]

```
nx:=90
cells:=2e-09
dia:=170e-09
SetGridsize(nx,nx,nx)
```

```
SetCellsize(cells, cells, cells)
SetGeom(Ellipsoid(dia, dia, dia))
a:= (dia/2/cells)-10
reg1:=Cylinder(dia,cells)
reg2:=Cylinder(dia,cells).transl(0,0,1*cells)
reg3:=Cylinder(dia,cells).transl(0,0,15*cells)
reg4:=Cylinder(dia,cells).transl(0,0,-10*cells)
reg5:=Cylinder(dia,cells).transl(0,0,-20*cells)
reg6:=Cylinder(dia,cells).transl(0,0,5*cells)
DefRegion(1,reg1)
DefRegion(2,reg2)
DefRegion(3,reg3)
DefRegion(4,reg4)
DefRegion(5,reg5)
DefRegion(6,reg6)

defMsat  := 384e3
Msat = defMsat
defAex := 8.8e-12
Aex = defAex
Kc1   = 10e3
defDbulk := 1.6e-3
Dbulk = defDbulk
Edgesmooth = 8
alpha = 0.5
openBC = true
maxParticleNumber := 1
randomSeed := CAMBIO
randSeed(randomSeed)

// random cubic anisotropy direction
        theta := 2.0*pi*rand()
        phi := acos(1.0-2.0*rand())
        //axis1 := vector (0,0,1)
        axis1  := vector(sin(phi)*cos(theta),sin(phi)*sin(theta), cos(phi))
```

```
        theta2 := 2.0*pi*rand()
        phi2 := acos(1.0-2.0*rand())
        helper  := vector(sin(phi2)*cos(theta2),sin(phi2)*sin(theta2), cos(phi2))
        axis2 := axis1.cross(helper)
        AnisC1 = axis1 // axes need not be normalized
        AnisC2 = axis2
// Save the direction of the easy axes
fprintln("Parti-Eaxes.txt", j, AnisC1, AnisC2)

lex := sqrt((2.0*defAex)/(pow(defMsat,2)*mu0))
ld := (4*3.14*defAex)/defDbulk
print("lex (nm)",lex*1e09)
print("ld (nm)",ld*1e09)
//print("pi", pi)
print("Msat =",Msat)
m = BlochSkyrmion(1,-1)

qtop1:=0.0
qtop2:=0.0
qtop3:=0.0
qtop4:=0.0
qtop5:=0.0
qtop6:=0.0

Bmax := 1.0
Bstep := 0.5e-2
TableAdd(B_ext)
tableaddvar(qtop1,"q1","")
tableaddvar(qtop2,"q2","")
tableaddvar(qtop3,"q3","")
tableaddvar(qtop4,"q4","")
tableaddvar(qtop5,"q5","")
tableaddvar(qtop6,"q6","")
tableadd(AnisU)
tableadd(ext_topologicalcharge)
```

```
tableadd(ext_topologicalchargelattice)
tableadd(E_total)
tableadd(E_zeeman)
tableadd(E_exch)
tableadd(E_demag)
tableadd(E_anis)

//hysteresis loops:
for B:=−3.0; B<=−1.0; B+=0.25{
qtop1=0.0
qtop2=0.0
qtop3=0.0
qtop4=0.0
qtop5=0.0
qtop6=0.0
fprintln(”filename.txt”, i, B)

        B_ext = vector(0.0,0.0,B)
        print(B,”B”)
        relax()
        FilenameFormat=sprintf(”%%s%%06d”)
        save(m)

        count1:=0
        count2:=0
        count3:=0
        count4:=0
        count5:=0
        count6:=0

        for i:=0; i<nx; i++{
            for j:=0; j<nx; j++{
                for k:=0; k<nx; k++{

                   if regions.GetCell(i,j,k)==1 {
```

```
            count1++
            }
            if regions.GetCell(i,j,k)==2 {
            count2++
            }
            if regions.GetCell(i,j,k)==3 {
            count3++
            }
            if regions.GetCell(i,j,k)==4 {
            count4++
            }
            if regions.GetCell(i,j,k)==5 {
            count5++
            }
            if regions.Getcell(i,j,k)==6 {
            count6++
            }

            }
        }
    }

s1:=ext_topologicalchargedensity.region(1).average()
s2:=ext_topologicalchargedensity.region(2).average()
s3:=ext_topologicalchargedensity.region(3).average()
s4:=ext_topologicalchargedensity.region(4).average()
s5:=ext_topologicalchargedensity.region(5).average()
s6:=ext_topologicalchargedensity.region(6).average()
qtop1= 0.25*cells*cells/pi*s1*count1
qtop2= 0.25*cells*cells/pi*s2*count2
qtop3= 0.25*cells*cells/pi*s3*count3
qtop4= 0.25*cells*cells/pi*s4*count4
}
```

E.3 Single Skyrmion in a Cylindrical FeGe Disk

This code was used to replicate the numerical results for the micromagnetic standard problem of materials with DMI proposed in Ref. [124].

```
lx := 200e-9
ly := 200e-9
lz := 20e-9

dx := 1e-09
dy := 1e-09
dz := 1e-09

SetGridSize(200,200,20)
SetcellSize(dx,dy,dz)

//Define the cylinder
SetGeom(Circle(lx))

defMsat  := 0.384e6
Msat = defMsat
defAex := 8.78e-12
Aex = defAex
defDbulk := 1.58e-3
Dbulk = defDbulk
SetPBC(2,2,0)
//Demag
NoDemagSpins = 1 \\ without dipolar interaction

lex := sqrt((2.0*defAex)/(pow(defMsat,2)*mu0))
ld := (4*3.14*defAex)/defDbulk
print("lex (nm)",lex*1e09)
print("ld (nm)",ld*1e09)
//print("pi", pi)
print("Msat =",Msat)
```

```
//Initial magnetization
m=BlochSkyrmion(1,−1)

B_ext = vector (0.0, 0.0, 0.4)


minimize()
save(m)
tableAdd(B_ext)
tableAdd(ext_topologicalcharge)
tableAdd(ext_topologicalchargelattice)
tableAdd(E_total)
tableAdd(E_zeeman)
tableAdd(E_exch)
tableAdd(E_demag)
tableAdd(E_anis)
tablesave()
SaveAs(m,"isolated_FeGe_cylinder")
```